Modeling and Calculation of Heat Transfer Relationships for Concentrated Solar Power Receivers

by

Soenke Holger Teichel

A thesis in partial fulfillment of

the requirements for the degree of

Master of Science

(Mechanical Engineering)

At the

UNIVERSITY OF WISCONSIN – MADISON

2011

NATIONAL RENEWABLE ENERGY LABORATORY

UNIVERSITY OF WISCONSIN–MADISON

Approved by

Professor Sanford A. Klein

Professor Douglas T. Reindl

12/16/2011

Date:

Abstract

The objective of this research project is to develop an improved heat transfer model for receivers of concentrated solar power, focusing on the application in solar tower power plants. Specifically, this project aims to improve an existing heat loss model for a cavity receiver by implementing semi-gray radiation heat transfer and improving the correlations for natural and forced convection from the cavity to the surroundings.

The basis of this work is the existing model of a Cavity-Type Solar Central Receiver System, developed by (Feierabend, 2009). This model was developed for National Renewable Energy Laboratory's (NREL's) "Solar Advisor Model" (SAM); a software tool that allows users to examine and to compare solar technologies on economic, technological and operational bases. The solar technologies modeled in SAM include concentrated solar power (CSP), photovoltaic systems and solar heating systems. Funding for this project was provided by NREL, subcontract No. AGG-0-40293-01 under Prime Contract No. DE-AC36-08G028308.

As part of the work presented in this manuscript, a radiation model was developed on the basis of Gebhart's Absorption Factor Model (Gebhart, 1957) to model semi-gray radiation heat transfer inside the cavity receiver. The model theoretically supports an unlimited number of emissivity bands to approximate the emissivity distribution of the interacting surfaces; this study however focuses on the two band model. Compared to other radiation analysis methods, the approach developed offers simplicity due to its similarity to the functional form of the black surface enclosure model. In comparison to the radiosity method, the described method not only provides the net radiation heat transfer rate from a given surface but also the heat transfer between any two surfaces in the enclosure. Due to the simpler equation system, the method is expected to offer the benefit of reduced computational time in comparison to the radiosity method.

A literature survey showed that that none of the established free correlations are applicable over the full range of operational conditions of the cavity receiver, due to size of the apparatus and the high surfaces temperatures. Following findings of (Siebers, D.

and Kraabel, J., 1984) and(Leibfried, U. and Orthjohan, J., 1995) a model that provides an upper bound of natural convection losses was developed, by representing the cavity as a combination of independent flat plates. Forced convection was approximated using the approach presented in (Siebers, D. and Kraabel, J., 1984). This approach was modified to account for the dependence of the forced convection losses of the cavity on wind direction. All findings concerning the convection model are not backed by any reliable physical studies and have to be regarded as rough approximations.

The improved heat transfer model was implemented in the cavity receiver model in SAM (NREL, 2011). The improved semi-gray radiation model was also implemented in the external receiver model developed by (Wagner, 2008).

The influence of semi-gray radiation on the system performance was studied in annual simulation using TMY2 (typical meteorological year) to find an optimal emissivity distribution inside the cavity receiver to maximize annual thermal efficiency.

The performance of cavity and external receiver was compared for different surface emissivity configurations.

Acknowledgements

The time I spend at the University of Wisconsin-Madison during my Master's study will stay in my memory as one of the most fascinating and instructive sixteen months I ever got to experience.

I am very grateful that this opportunity was given to me by my advisors at the Solar Energy Laboratory of the University of Wisconsin, our contact persons at the National Renewable Energy Laboratory, who provided invaluable advice and the funding for this project. I would also like to thank Professor Seume from the Leibniz University Hannover, Germany who first told me about the possibility to study in Madison and helped to make my stay possible.

During my studies in Madison, I was truly lucky to have two advisors at the Solar Energy Laboratory with the dedication, competence and patience I experienced with Professor Klein and Professor Reindl.

Professor Klein's tremendous knowledge in the area of thermodynamics, solar energy technology and programming was a great help to guide me through the project. I'm thankful for his patience to help me solve problems with the project on my own, through his advice. Professor Reindl's practical knowledge and outside view assured to always keep the overall objective of the project in mind. At the same time he was always able to concentrate on important details of the model and showed ways to improve these.

The work with my advisors at the Solar Energy Laboratory not only helped me to improve my knowledge in the specific field of this project but shaped my approach to engineering problems as a whole.

I am also very grateful for the friendliness and support I experienced with my office mates, Rodrigo, Dan, Bryant, Diego and Amir who were always willing to share thoughts and offer help concerning study related or not. The friendship and support we shared as group of students at the Solar Energy Lab helped me a lot to accomplish both research and classwork during my studies at the University of Wisconsin-Madison.

Table of Contents

1 Introduction 1

1.1 Concentrated Solar Power – Power Tower Technology 1

1.2 System Advisor Model – Objective of this work 5

2 Cavity Receiver Model 6

3 Radiation Transfer 8

3.1 Radiation Heat transfer of a Cavity – Black Surfaces 9

3.2 Radiation Heat transfer of a Cavity – Diffuse Non-Gray Surfaces 11

3.2.1 Radiosity Method 13

3.2.2 The F-hat- Method 15

3.2.3 Extension to Two Band Semi - Gray Surface Model 19

3.2.4 Multi Band Semi - Gray Surface Model 24

4 Convective Heat Loss 26

4.1 Convective Heat Loss Regime of the Cavity Receiver 27

4.2 Natural Convection Correlations 32

4.2.1 Clausing (1983) 33

4.2.2 Clausing (1987) 35

4.2.3 Siebers and Kraabel (1984) 37

4.2.4 Paitoonsurikarn & Lovegrove (2006) 39

4.2.5 Leibfried and Ortjohan (1995) 42

4.2.6 Natural Convection at Independent Flat Plates 45

4.2.7 Forced Convection at Independent Flat Plates 47

4.3 Modeling of Forced Convection 48

4.4 Validity of the Correlations 53

4.5 Measurement of convection loss 55

4.5.1 Review of Existing Small-Scale Experimental Set Ups 55

4.5.2 Small-Scale Analysis 59
4.5.3 Large-Scale Analysis 62
4.5.4 Measurement of Useful Energy Gain of the HTF 64
4.5.5 Measurement of the Incoming Solar Flux 65
4.5.6 Measurement of Radiation Heat Loss 66
4.5.7 Flux-On Testing 67
4.5.8 Barron Method and Baker Modification 69
4.5.9 Flux Off Testing 71
4.5.10 Daytime Flux Off Transient Testing 72
5 Cavity Receiver Model in TRNSYS/SAM 77
5.1 Cavity Heat Transfer Model 77
5.1.1 Heat transfer to the HTF 78
5.1.2 Radiation Heat Transfer Model 80
5.1.3 Convective Heat Loss Model 81
5.2 Model of the Solar Tower Power Plant in TRNSYS 82
5.3 Implementation of the Cavity Receiver Model in FORTRAN 83
5.3.1 Uncoupled Convection Implementation 87
5.3.2 Coupled Convection Implementation 88
5.3.3 Iterative scheme to solve the energy balances 92
6 Results 100
6.1 Performance of the Cavity Receiver 100
6.2 Sensitivity of the Model to the Number of Bands 113
6.3 Comparison of the Convection Correlations 121
6.3.1 Behavior and Characteristics of the Correlations 123
6.3.2 Influence of the Correlations on the Receiver Model 125
6.3.3 Influence of the Forced Convection 128

6.4 Comparison Cavity vs. External Receiver 130

6.4.1 External Receiver Model – Implementation of Semi-Gray Surfaces 130

6.4.2 Comparison Cavity vs. External Receiver 132

7 Conclusion 142

8 Future Work 144

9 Bibliography 146

10 Appendices 151

List of figures

Figure 1.1 – Photo of Gemasolar Power Tower in Fuentes de Andalucía, Spain (Torresol Energy) 2
Figure 1.2 – Heliostat Field of Gemasolar Power Tower in Fuentes de Andalucía, Spain (Teichel, 2011)..... 2
Figure 1.3 – Schematical illustration of the Solar Tower Power Plant from (Ho, C.K. et al., 2010) 4
Figure 2.1 – 3D view, front of the cavity receiver 6
Figure 2.2 – Bottom view of the cavity receiver 7
Figure 3.1 - Selected radiation pathways between surface i and j inside a general enclosure with reflective surfaces. 12
Figure 3.2 - Definition of radiosity for surface i - (Nellis, G. and Klein, S.A., 2009) 13
Figure 3.3 - Emissivity step in semi-gray heat transfer model. 20
Figure 4.1 – Richardson number of the cavity receiver vs. wind velocity 29
Figure 4.2 – Wind velocity at the tower from TMY-data – Blythe, CA 30
Figure 4.3 - Network representation of the convection loss mechanism – from (Clausing, 1983) 33
Figure 4.4 - Cavity orientation, from (Siebers, D. and Kraabel, J., 1984) 38
Figure 4.5 - Comparison of cavity- and vertical plate correlations (Siebers, D. and Kraabel, J., 1984)..... 39
Figure 4.6 - Receiver configurations used by (Paitoonsurikarn, S. and Lovegrove K., 2006)..... 40
Figure 4.7 – Denotation of geometrical parameters used in the definition of the ensemble cavity length scale L_s, (Paitoonsurikarn, S. and Lovegrove K., 2006)..... 41
Figure 4.8 - Examined cavity geometries - out of (Leibfried, U. and Orthjohan, J., 1995) 42
Figure 4.9 - Streamlines in a spherical receiver out of (Leibfried, U. and Orthjohan, J., 1995) ... 43
Figure 4.10 - Flow configuration in a hemispherical cavity out of (Leibfried, U. and Orthjohan, J., 1995) 43
Figure 4.11 - Estimated cavity convective losses for flux-off tests, (Smith, D.C. and Chavez, J.M. , 1987), p.304ff 49
Figure 4.12 - Wind direction from TMY-data Blythe, CA 50
Figure 4.13 - Wind rose from TMY-data Blythe, CA with cavity orientation 50
Figure 4.14 – Exemplary scaling factor to account for wind direction dependence of forced convection 51

Figure 4.15 – Cavity receiver sketch and wind direction used in numerical study by (Fang, J.B. et al., 2011) 52
Figure 4.16 – Heat loss of the receiver normalized by incident solar radiation. (Fang, J.B. et al., 2011) 52
Figure 4.17 - Experimental set up, (Prakash, M. et al., 2008) 55
Figure 4.18 – Front view cavity receiver (Prakash, M. et al., 2008) 56
Figure 4.19 - Side view cavity receiver (Prakash, M. et al., 2008) 56
Figure 4.20 - Experimental set up (Leibfried, U. and Orthjohan, J., 1995) 57
Figure 4.21 – Outline of experimental set up (Taumoefolau, T. et al., 2004) 58
Figure 4.22 – Non-dimensional convective loss measurement uncertainty- flux on test – measurement error as parameter (Falcone, P., K. et al., 1981) 63
Figure 4.23 – Non-dimensional convective loss measurement uncertainty- flux off test – measurement error as parameter (Falcone, P., K. et al., 1981) 63
Figure 4.24 - Daytime flux-off testing scheme 73
Figure 5.1 – Computation surface segments of the cavity receiver geometry 78
Figure 5.2 - Scheme of the heat transfer model of the HTF pipe 79
Figure 5.3 – General structure of TYPE 232 84
Figure 5.4 – Parameters in the model to choose the convection implementation method 91
Figure 5.5 – Simplified Schematic Iteration Method 92
Figure 5.6 – Code Structure Cavity Receiver Model 99
Figure 6.1 - Annual average incident solar radiation on the receiver 102
Figure 6.2 - Thermal radiation loss distribution –gray surfaces, ε_{solar}=0.95; $\varepsilon_{thermal}$=0.95; $\varepsilon_{solar-passive}$=0.95; $\varepsilon_{thermal-passive}$=0.95 102
Figure 6.3 - Solar radiation loss distribution gray surfaces, ε_{solar}=0.95; $\varepsilon_{thermal}$=0.95; $\varepsilon_{solar-passive}$=0.95; $\varepsilon_{thermal-passive}$=0.95 102
Figure 6.4 - Thermal radiation loss distribution – semi-gray surfaces, ε_{solar}=0.95; $\varepsilon_{thermal}$=0.1; $\varepsilon_{solar-passive}$=0.95; $\varepsilon_{thermal-passive}$=0.1 103
Figure 6.5 - Solar radiation loss distribution gray surfaces, ε_{solar}=0.95; $\varepsilon_{thermal}$=0.1; $\varepsilon_{solar-passive}$=0.95; $\varepsilon_{thermal-passive}$=0.1 103
Figure 6.6 - Thermal radiation loss from the passive surfaces as a function of thermal emissivity for different solar emissivities; λ_{step}=5μm. 104
Figure 6.7 - Thermal radiation loss from the passive surfaces as a function of thermal emissivity for different solar emissivities; λ_{step}=2μm. 104

Figure 6.8 - two dimensional vertical sectional view of the cavity receiver, illustrating radiation loss paths from the passive surfaces 105
Figure 6.9 – Temperatures of the passive surfaces as a function of thermal emissivity for different solar emissivities; λ_{step}=5μm. 106
Figure 6.10 - Temperatures of the passive surfaces as a function of thermal emissivity for different solar emissivities; λ_{step}=2μm. 107
Figure 6.11-Thermal radiation loss distribution gray surfaces ε_{solar}=0.95; $\varepsilon_{thermal}$=0.1; $\varepsilon_{solar-passive}$=0.1; $\varepsilon_{thermal-passive}$=0.1 109
Figure 6.12 - Solar radiation loss distribution gray surfaces, ε_{solar}=0.95; $\varepsilon_{thermal}$=0.1; $\varepsilon_{solar-passive}$=0.1; $\varepsilon_{thermal-passive}$=0.1 109
Figure 6.13 – Temperatures of the passive surfaces as a function of thermal emissivity and emissivity of the passive surfaces for different solar emissivities; λ_{step}=5μm. 109
Figure 6.14 - Cavity receiver efficiency as a function of emissivity for different emissivity step wavelengths. 110
Figure 6.15 - Radiation loss of the cavity as a function of emissivity for different emissivity step wavelengths. 111
Figure 6.16 - Convection loss of the cavity as a function of emissivity for different emissivity step wavelengths. 112
Figure 6.17 – Emissivity distribution of a hypothetical absorber surface 113
Figure 6.18 - One band approximation, hypothetical surface 114
Figure 6.19 - Two band approximation, hypothetical surface 114
Figure 6.20 - Three band approximation, hypothetical surface 114
Figure 6.21 - Four band approximation, hypothetical surface 114
Figure 6.22 - Five band approximation, hypothetical surface 114
Figure 6.23 - Six band approximation, hypothetical surface 114
Figure 6.24 - Seven band approximation, hypothetical surface 115
Figure 6.25 - Emissivity distribution of a hypothetical absorber surface and spectral emissive powers for the full integration range. 116
Figure 6.26 - Influence of the number of bands on receiver performance – run #1 117
Figure 6.27 - Influence of the number of bands on receiver performance – run #2 117
Figure 6.28 - Influence of the number of bands on receiver performance – run #3 117
Figure 6.29 - Influence of the number of bands on receiver performance – run #4 117

Figure 6.30 - Emissivity of Pyromark 2500 surface coating as a function of wavelength, (Tempil, 2012)..... 118
Figure 6.31 – One band approximation..... 119
Figure 6.32 - Two band approximation..... 119
Figure 6.33 – Five band approximation 119
Figure 6.34 - Ten band approximation..... 119
Figure 6.35 - Influence of the number of bands on receiver performance; Pyromark 2500 120
Figure 6.36 - Overall convection loss coefficient in respect of emissivity. Solar emissivity of the active surfaces is 0.95, all other emissivity vary with $\varepsilon_{thermal}$; λ_{step}=5μm. 122
Figure 6.37 - Cavity efficiency for different convection correlations with $\varepsilon_{solar,active}$ = 0.95 and $\varepsilon_{solar,passive}$.= $\varepsilon_{thermal}$=0.1 126
Figure 6.38 – Heat losses normalized by incident solar radiation for different convection correlations 127
Figure 6.39 – Convective heat transfer coefficients of the natural convection correlation, including the implementation methods of forced convection..... 128
Figure 6.40– Receiver efficiency for the different natural convection correlation, including the implementation methods of forced convection 129
Figure 6.41 – Dimensions of External and Cavity Receiver in Comparison..... 133
Figure 6.42 - Thermal efficiencies of cavity and external receiver for different emissivities; Emissivity step wavelength is at 5μm 134
Figure 6.43 – Normalized radiation- and convection loss of cavity and external receiver for different emissivities – $\varepsilon_{solar\text{-}active}$=0.95..... 135
Figure 6.44 - Normalized radiation- and convection loss of cavity and external receiver for different emissivities – $\varepsilon_{solar\text{-}active}$=0.85..... 136
Figure 6.45 - Normalized reflective- and thermal radiation loss of cavity and external receiver for different emissivities – $\varepsilon_{solar\text{-}active}$=0.95..... 137
Figure 6.46 - Thermal efficiencies of cavity and external receiver for different emissivities; Emissivity step wavelength is at 2μm 139
Figure 6.47 - Normalized radiation- and convection loss of cavity and external receiver for different emissivities – $\varepsilon_{solar\text{-}active}$=0.95..... 139
Figure 6.48 - Normalized radiation- and convection loss of cavity and external receiver for different emissivities – $\varepsilon_{solar\text{-}active}$=0.85..... 140

Figure 6.49 - Normalized reflective- and thermal radiation loss of cavity and external receiver for different emissivities – $\varepsilon_{solar\text{-}active}$=0.95..... 141

Table of Tables

Table 2.a – Dimensions of the receiver used in this study (100MWe)..... 8
Table 3.a - Fraction of solar and thermal radiation within specific wavelengths bands..... 20
Table 4.a - Characteristic receiver parameters 31
Table 4.b – Heat transfer correlations for different flow regimes, (Clausing, 1987) 36
Table 4.c – Coefficients for (Paitoonsurikarn S. and Lovegroove K., 2003) – natural convection correlations 41
Table 4.d - Rayleigh number range of the cavity receiver surfaces over a range of operating conditions 46
Table 4.e - Validity Range of Convection Correlations 53
Table 4.f - Conditions required to achieve similarity for a small-scale experimental set up 61
Table 4.g - Assumed uncertainties of the measured inputs to evaluate the heat loss components 68
Table 4.h - Flux on - Uncertainty of heat loss component determination 69
Table 4.i - Flux off uncertainty of heat loss component determination..... 71
Table 5.a - TRNSYS Types that comprise the Solar Tower Model 82
Table 6.a - Results table – variation of emissivity distribution – λ_{step}=5μm..... 100
Table 6.b - Selected dimension of External and Cavity Receiver in Comparison..... 133

Nomenclature

A	m^2	Surface area
β	$\frac{1}{K}$	Expansion factor
Bi	–	Biot number
c	$\frac{J}{kg-K}$	Specific heat
C_1	$W-\mu m^4$	Constant in Planck's spectral energy distribution
C_2	$\mu m-K$	Constant in Planck's spectral energy distribution
D	m	Diameter
E_b	$\frac{W}{m^2}$	Blackbody emissive power
F	–	View Factor
f	–	Fraction function
$\hat{F}$	–	F-hat factor
$Flux$	$\frac{W}{m^2}$	Heat flux
G	$\frac{W}{m^2}$	Irradiation
g	$\frac{m}{s^2}$	Gravitational constant
Gr	–	Grashof number
H	m	Height
h	$\frac{W}{m^2-K}$	Heat transfer coefficient
J	$\frac{W}{m^2}$	Radiosity
k	$\frac{W}{m^2}$	Conductivity
L	m	Length
M	kg	Mass
N	–	Number of Surfaces; Number of surfaces per receiver panel
Nu	–	Nusselt number
$\Pr$	–	Prandtl number

$\dot{Q}$	W	Heat transfer rate
R	$\frac{W}{K}$	Heat transfer resistance
Ra	–	Rayleigh number
Re	–	Reynolds number
Ri	–	Richardson number
T	K	Temperature
U	J	Internal energy
u	$\frac{m}{s}$	Wind velocity
UA	$\frac{W}{K}$	Conductance

Greek Letters

β	$\frac{1}{K}$	Volumetric expansion factor
ν	$\frac{m^2}{s}$	Kinematic viscosity
σ	$\frac{W}{m^2K^4}$	Kinematic viscosity
α	–	Diffuse surface absorptivity
ε	–	Diffuse surface emissivity
ρ	–	Diffuse surface reflectivity / Fluid density
τ	–	Diffuse surface transmissivity / Time constant
λ	μm	Radiation wavelength
θ	deg	Receiver tilt angle
ν	$\frac{m^2}{s}$	Kinematic viscosity

Subscripts

$aperture$	Receiver Aperture
i, j, k	Indicate receiver surfaces
lip	Receiver Lip
$panel$	Receiver Panel
s	Surface
$solar$	Solar radiation
$thermal$	Thermal radiation
$wall$	Wall

Acronyms

CFD	Computational Fluid Dynamics
CSP	Concentrated
HTF	Heat Transfer Fluid
NREL	National Renewable Energy Laboratory
SEL	Solar Energy Laboratory
SAM	Solar Advisor Model
TRNSYS	Transient System Simulation Tool

1 Introduction

The production of energy in an ecologically justifiable, cost-effective way is one of the key challenges facing our society. Meeting the energy demand of a growing population in a way that minimizes negative impact on the environment is a premise for the development and preservation of prosperity and wellbeing not only of developing- but also for industrialized countries. Only if energy is widely accessible and affordable to everyone, our society as a whole can benefit.

Renewable energies will play an increasingly important role in achieving this goal. In particular the use of solar energy has promising potentials to help meet our energy demand for the future. A very simplified example illustrates the great energy solar resources available: The average annual electricity consumption of the USA (Division, United Nations Statistics, 2008) for example corresponds to the average solar energy that could be received by a heliostat field in an average year in Long Beach, California with an area of 601 square miles (ca. 1558 km^2) – that is approximately 50% of the area of Dane County, WI (calculation in Appendix A).

The Solar Power Tower Technology, studied in this work, represents a highly efficient way to convert solar energy into electricity and process heat. This technology is very likely to play a significant role in the way solar energy will help to meet our future energy demand.

1.1 Concentrated Solar Power – Power Tower Technology

The concept of a Solar Tower Power Plant is shown in Figure 1.3. A field of mirrors, called Heliostats, tracks the movement of the sun and reflects the incident solar radiation onto a receiver located at the top of a tower. The multiplicity of heliostats results in a concentration of solar energy on the tower's receiver. In the receiver, a part of the incident solar energy is transferred to a heat transfer fluid (HTF). The heat carried in this fluid can be utilized in various ways, such as process heat or energy production.

Figure 1.1 – Photo of Gemasolar Power Tower in Fuentes de Andalucía, Spain (Torresol Energy)

Figure 1.2 – Heliostat Field of Gemasolar Power Tower in Fuentes de Andalucía, Spain (Teichel, 2011)

Compared to other concentrated solar power plant technologies, the Solar Tower design offers higher possible concentration ratio due to the surrounding solar field and therefore higher theoretical receiver temperatures. The receiver temperatures are limited due to material constraints and not by the available solar radiation. Because of the central position of the power

block near the receiver, this design reduces the infrastructure of the plant and avoids pumping losses due to long plumbing.

Different types of receivers are used. From simple absorber surfaces that absorb part of the incoming energy and transfer it to a heat transfer fluid (HTF) (tube receiver) to various types of volumetric receivers, where the HTF itself is the absorbing material. In these so called volumetric receivers gas is the most common heat transfer medium. New designs are in development to use reacting gas flows or solid particles as a HTF to enhance the absorptive properties, (Hunt, A., 1979), (Z'Graggen,A. and Steinfeld,A., 2009). Depending on the type of heat transfer fluid, different uses of the absorbed heat can be considered. High temperature gases can be used to power a Brayton cycle for electricity production. Other fluids are more favored to generate steam to power Rankine cycle type power block. For the absorber surface type receivers two principle receiver designs are distinguished. The external receiver type, in general, has a cylindrical shape with the absorber surface outward facing and fully exposed to the surroundings. With this design a surrounding heliostat field with a comparably small diameter can be employed. In this way, atmospheric radiation losses from the heliostats to the receiver are minimized; also the focus point of the field is lower which results in reduced tower height, an important cost factor. A different receiver type is the so called cavity receiver. This type of receiver shades the absorber surfaces from the surroundings and supposedly leads to lower radiation and convection losses from the absorber surfaces. Because cavity receivers are usually only open to one side the solar tower can no longer be located in the center of the heliostat field but instead at the south edge. This geometry leads to an increased distance between the heliostats and the receiver, increasing atmospheric losses and requiring a higher tower. The optimal tower design depends on the required thermal power of the tower. The power of the solar tower is proportional to the area of the heliostat field. With increasing heliostat field size the efficiency advantage of the cavity receiver design will be overpowered by the decreasing field efficiency in comparison to central external receivers. This work focuses on an analysis of the cavity receiver design with absorber surfaces that convey a liquid HTF.

To provide better grid integration of solar power towers and under the competitive pressure the concentrated solar power technology experiences from the side of the photovoltaic technologies, dispatchability of the energy production is important to solar power tower development. Some types of heat transfer fluids, such as molten salts, offer high specific heat capacity and great potential for thermal storage. There are also studies that discuss the use of sand as a heat transfer

and storage medium(Al-Ansary,H. et al., 2011). Thermal storage offers the ability to uncoupled energy production of the solar plant from the incident solar energy. This capability can be used to avoid the highly variable energy production that is characteristic for other renewable energy technologies such as wind turbines and photovoltaics. With storage new modes of energy production with a solar power plant are imaginable. From offsetting the peak energy production a few hours, providing peak load when it is needed to base load energy production. Because the value of energy production is not only the ability to provide energy but to provide energy according to the demand, storage can be an attractive way to make thermal solar power plants more competitive with convectional power plants. Figure 1.3 shows, apart from the external receiver, the schematic configuration of the power plant that is described in the model.

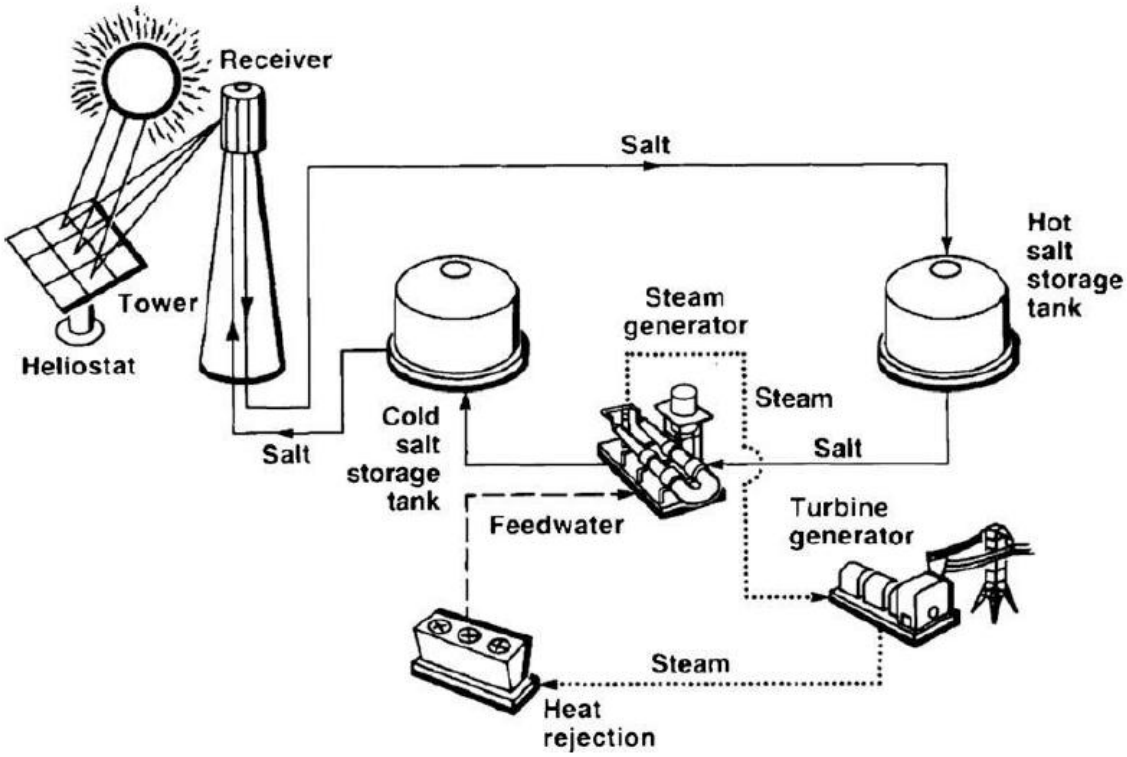

Figure 1.3 – Schematical illustration of the Solar Tower Power Plant from (Ho, C.K. et al., 2010)

In our model a heliostat field concentrates solar energy on a cavity receiver. The receiver transfers the absorbed heat to a molten salt which is supplied by a cold salt storage tank and once heated, stored in a separate hot storage tank. At times when energy is needed, hot molten salt from the tank is used to generate steam to power a steam turbine which is coupled with a generator to produce electricity.

1.2 System Advisor Model – Objective of this work

The main objective of this work is to improve the heat transfer model of an existing cavity receiver model implemented in the System Advisor Model (SAM). This software tool was developed by the National Renewable Energy Laboratory (NREL) and is available for free download at (NREL, 2011). SAM allows users to examine and to compare solar and other renewable technologies on economic, technological and operational bases. SAM is based on the Transient Systems Simulation (TRNSYS) program, maintained and distributed by (Klein, S.A. et al., 2007). TRNSYS provides a software platform to model thermodynamic systems on a modular basis in dependence on hourly weather data. It is widely used to simulate buildings and renewable energy systems. Any process in a thermodynamic system simulated in TRNSYS can be represented as a separate module that interacts with other modules in the system. TRNSYS offers an extensive library of existing modules for various applications; modules can also be developed by the user, coded according to a TRNSYS template in FORTRAN and complied in the TRNSYS .DLL (Dynamic Link Library). SAM provides a graphical interface to specify and run a predefined TRNSYS simulation and to analyze the outputs. SAM provides detailed modules in TRNSYS to simulate complex energy systems such as concentrated solar power (CSP), photo-voltaic systems and solar heating systems.

The previous solar tower models include external receiver (Wagner, 2008) and a cavity receiver (Feierabend, 2009). The cavity model by (Feierabend, 2009) considered a receiver with black surfaces, and natural convection. The convection loss was uncoupled from the energy balances which leads the effect that the convection losses are considered in the overall receiver efficiency and performance, the cavity surface temperature however are independent on the convection loss. Improvements in this work were done by implementing a radiation model that considers semi-gray surfaces and includes convective losses in the energy balances. A natural convection model was developed that provides an upper bound of free convection loss from the cavity. An important objective was to include forced convection in the model. A very simple model described in Section 4.3 approximates forced convection loss. The model was extended to consider the effect of wind direction on the overall convection loss. The author sees the need for further research in this field to develop a reliable, verified model that describes wind effects on the convective heat loss of a cavity receiver.

2 Cavity Receiver Model

The receiver was chosen in the initial modeling work done by (Feierabend, 2009). Detailed information about the geometric relationship and design of the receiver model are given in his thesis. A brief description of the receiver geometry and dimensions used in this study is given in this section.

The active (absorbing) portion of the receiver consists of four vertical rectangular heat exchanger panels (Panels 1-4) arranged in a half-octagon. Each individual panel is comprised of a set of tubes through which the heat transfer fluid (HTF) flows. In the radiation model, these surfaces are simplified to be planes. The tube character is however taken into account for the calculation the heat transfer resistance from the absorbing surfaces to the HTF.

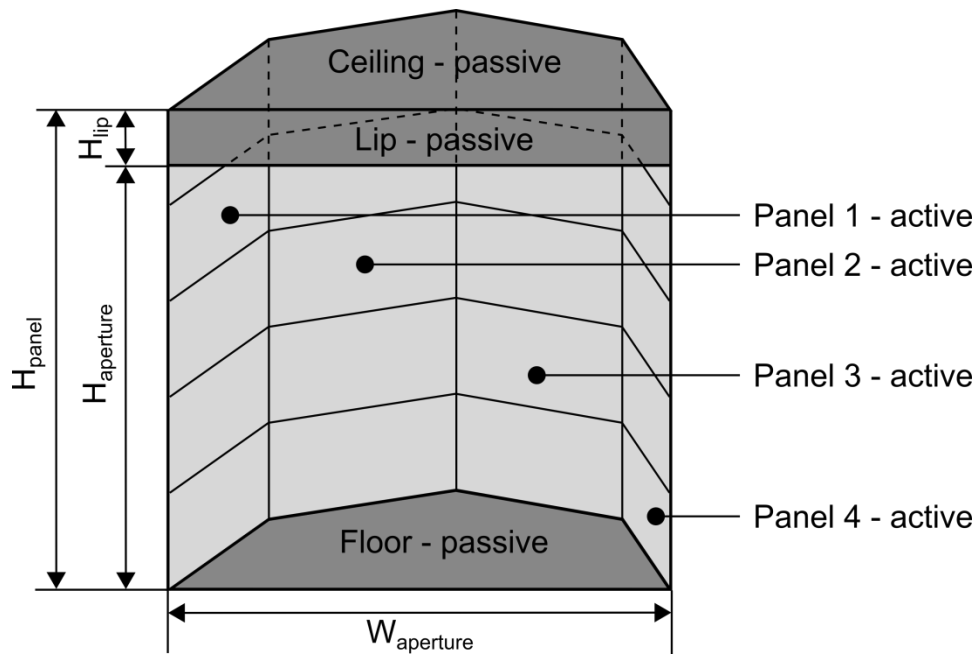

Figure 2.1 – 3D view, front of the cavity receiver

The active panels of the cavity receiver approximate a semi-cylindrical shape. Three additional passive surfaces are required to enclose active panels and form a cavity: top, bottom and a "lip" that partially covers the cavity opening. Although these passive surfaces do not directly heat the molten salt, they are important to consider from a heat transfer standpoint since they experience both, radiation and convection losses, each loss mechanism will influence the surface temperatures of the active panels within the cavity. Each of the passive surfaces is assumed to be adiabatic and their operating temperature depends on the balance of absorbed radiation and

convection from the other surfaces in the cavity. The top and bottom are needed to create a cavity enclosure. The lip is purposefully attached at the top of the opening of the cavity to create a stagnant zone in order to decrease convection losses.

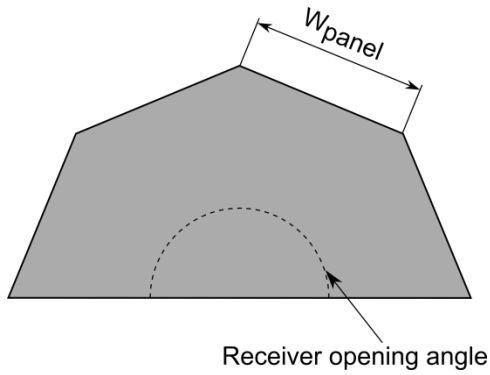

Figure 2.2 – Bottom view of the cavity receiver

The temperature of the absorber panels varies with vertical position in a manner dependent on the incident solar flux and the plumbing arrangement for the HTF. In this case, the HTF is assumed to enter at the bottom of each receiver panel (at its lowest temperature) and proceed vertically through tubing to an outlet header located at the top of the panel. In order to resolve this temperature distribution, the absorber panels are divided vertically into *N* sections (nodes). The model is designed to allow *N* to range from 1 to 10. Each node represents a surface segment of the receiver that is assumed to be at a uniform temperature for any time step. All properties of a particular node or surface segment are assumed constant at a value corresponding to the average surface temperature. It was found previously by (Feierabend, 2009) that five nodes per panel provide a reasonable compromise between accuracy and computational speed. All results presented in this paper are based on a model with five nodes per panel. Considering the receiver aperture as a single node virtual surface, there are a total of 24 surfaces that participate in radiation heat exchange. The dimensions of the cavity receiver in this work are chosen through optimization functions in SAM to provide a name plate electric power of 100MWe. The resulting dimensions are given in Table 2.a below.

H_{panel}	23.95 m
H_{lip}	2.75 m
$H_{aperture}$	21.2 m
$W_{aperture}$	25.78 m
W_{panel}	9.87 m
Receiver opening angle	180°
Active surface area	945 m^2
Passive surface area	540.85 m^2

Table 2.a – Dimensions of the receiver used in this study (100MWe)

3 Radiation Transfer

The radiation is the major heat loss mechanism of a solar central receiver. The radiation loss can be separated in two different modes. One mode of radiation loss is due to the high temperature difference of the receiver surface and the surroundings here called "thermal radiation loss". Another type of radiation loss is caused by the imperfect absorptive capabilities of the surfaces. Because this loss mechanism has its most significant effect by reducing the amount of absorbed solar radiation by reflecting solar radiation from the absorber surfaces, it is called "solar radiation loss". These types of radiation can be approximately distinguished by their wavelength, the maximum of thermal radiation occurs at larger wavelength, the maximum of solar radiation at smaller wavelength.

To evaluate the different modes of radiation loss a radiation heat transfer model for the interacting surfaces inside the cavity has to be developed. In the coming sections this process is described for different assumptions concerning the surface properties of the receiver. All radiation heat transfer models described in this work assume diffuse surfaces. The radiative surfaces properties are assumed to be independent of the direction of incoming radiation. This assumption is appropriate in that detailed information and control of the specular properties of solar surface coatings is generally not available.

3.1 Radiation Heat transfer of a Cavity – Black Surfaces

The simplest approach to model radiation heat transfer is the theory of black surfaces. All incident radiation is absorbed by the surfaces in the enclosure. The net rate of radiation heat transfer to a surface is the difference between the rate of radiation that is absorbed by the surface and the rate of radiation that is emitted by the surface.

The ratio of radiation leaving an arbitrary surface *i* falling directly on another surface *j*, to the total radiation leaving surface *i* is called view factor.

$$F_{i,j} = \frac{\text{radiation leaving surface } i \text{ that falls directly on surface } j}{\text{total radiation leaving surface } i} \tag{3.1}$$

The view factor depends solely on the geometric configuration of the surfaces with respect to each other; therefore, it is only a function of spatial surface orientation and not dependent on surface properties or radiation heat transfer mechanisms. View factors for a number of common geometries are available in the open literature (Howell, 2010). For complex geometries where view factors cannot be analytically determined, the Monte-Carlo method can be used to determine the view factors. In the Monte-Carlo method as applied in this work for diffuse surfaces, a large number of rays with a random direction are generated from a uniform diffuse distribution over the origin surface. The path of each ray is traced to determine if it intercepts the interacting (receiving) surface. The view factor between the two surfaces is calculated as the ratio of the number of rays that originated from surface *i* and hit surface *j* to the total number of rays that originated from surface *i*. This method has been used to determine the view factors for the participating cavity surfaces that do not have an analytic solution (Feierabend, 2009). A general description of the application of the Monte-Carlo method for the determination of view factors is given in (Nellis, G. and Klein, S.A., 2009). Apart from determining view factors between two surfaces that can see one another, there are two rules that help in determining the required view factors for surfaces comprising the cavity, as documented in Nellis & Klein (2009).

The Enclosure Rule states that all of the radiation emitted by a surface within an enclosure must strike another surface in the enclosure. For an enclosure consisting of *N* surfaces, this rule can be formulated as:

Enclosure rule: $$1 = \sum_{j=1}^{N} F_{i,j} \quad \text{for } i = 1..N \tag{3.2}$$

The second rule, *reciprocity*, states that for two interacting surfaces, the product of the view factor and the area of the emitting surface is the same. This relation can be deduced from Eqn. (3.6) later in this section.

Reciprocity rule: $$A_i \cdot F_{i,j} = A_j \cdot F_{j,i} \tag{3.3}$$

The total rate of emitted radiation by a black surface *i*, that impinges directly on surface *j* is the product of the area and the blackbody emissive power of the surface and the view factor for the interacting surfaces.

$$\dot{Q}_{i,emitted,j} = A_i \cdot F_{i,j} \cdot E_{b,i} = A_i \cdot F_{i,j} \cdot \sigma \cdot T_i^4 \tag{3.4}$$

With E_b representing the black body emissive power and σ the Stefan-Boltzmann constant. Similarly to Eqn. (3.4) the radiation emitted by surface *j* that strikes surface *i* is:

$$\dot{Q}_{j,emitted,i} = A_j \cdot F_{j,i} \cdot \sigma \cdot T_j^4 \tag{3.5}$$

The net rate of radiation heat transfer between two surfaces *i* and *j* is the difference between the emitted radiation of the particular surface that strikes the other surface.

$$\dot{Q}_{i,j} = A_i \cdot F_{i,j} \cdot \sigma \cdot T_i^4 - A_j \cdot F_{j,i} \cdot \sigma \cdot T_j^4 \tag{3.6}$$

At this point, Eqn. (3.3) can be deduced. Assuming the surface *i* and *j* are at the same temperature
($T_i = T_j$), the radiation heat transfer between the two surfaces has to equal zero, $\dot{Q}_{i,j} = 0$. In this case, Eqn. (3.6) can be rearranged to:

$$A_i \cdot F_{i,j} \cdot \sigma \cdot T_i^4 = A_j \cdot F_{j,i} \cdot \sigma \cdot T_j^4 \tag{3.7}$$

With $T_i = T_j$, Eqn. (3.7) can be simplified to:

$$A_i \cdot F_{i,j} = A_j \cdot F_{j,i} \tag{3.8}$$

Although Eqn. (3.8) was found with the assumption of equal surface temperatures and $\dot{q}_{i,j} = 0$, it is independent of temperatures; therefore, valid for any heat transfer process.

Using the reciprocity rue, Eqn. (3.6) can be simplified to:

$$\dot{Q}_{i,j} = A_i \cdot F_{i,j} \cdot \sigma \cdot (T_i^4 - T_j^4) = A_i \cdot F_{i,j} \cdot (E_{b,i} - E_{b,j}) \tag{3.9}$$

This approach was used by (Feierabend, 2009) to simulate the initial cavity receiver model with black surfaces.

3.2 Radiation Heat transfer of a Cavity – Diffuse Non-Gray Surfaces

The radiation characteristics of non-black (reflective) surfaces can be described in terms of the surface emissivity (ε_i), defined as a fraction of the radiation that is emitted by the non-black surface compared to the radiation that a black surface would emit, at a particular wavelength. The emissivity ranges between zero (perfect reflector) and unity (perfect emitter). Analogous to Eqn. (3.4), Eqn. (3.10) provides the thermal radiation that is emitted by a non-black surface *i* and directly intercepts surface *j*.

$$\dot{Q}_{i,\text{emitted},j} = \varepsilon_i \cdot \sigma \cdot A_i \cdot F_{i,j} \cdot T_i^4 \tag{3.10}$$

For a given wavelength, Kirchhoff's Law requires the emissivity of a diffuse surface to equal its absorptivity:

$$\underset{\text{emissivity}}{\varepsilon_{i,\lambda}} = \underset{\text{absorptivity}}{\alpha_{i,\lambda}} \tag{3.11}$$

Also, the absorptivity, reflectivity and transmissivity must sum to 1.

$$1 = \underset{\text{emissivity}}{\varepsilon_{i,\lambda}} + \underset{\text{reflectivity}}{\rho_{i,\lambda}} + \underset{\text{transmissivity}}{\tau_{i,\lambda}} \tag{3.12}$$

In comparison to black surfaces where all radiation is absorbed, part of the radiation incident on non-black surfaces will also be reflected or transmitted. Because all surfaces in the cavity are opaque, the transmissivity is zero and not considered in this work

In a cavity consisting of non-black (reflective) opaque surfaces, radiation can not only be transferred directly between surface *i* and *j* but also indirectly by reflection from any other surfaces of the enclosure. Selected radiation pathways inside an enclosure with reflective surfaces are shown in Figure 3.1. Reflections complicate the radiation heat transfer model because it is necessary to consider all possible radiation pathways between the interacting surfaces, including multiple reflections at intermediate surfaces. Eqn. (3.10) only considers the direct path of emitted radiation from surface *i* to *j*.

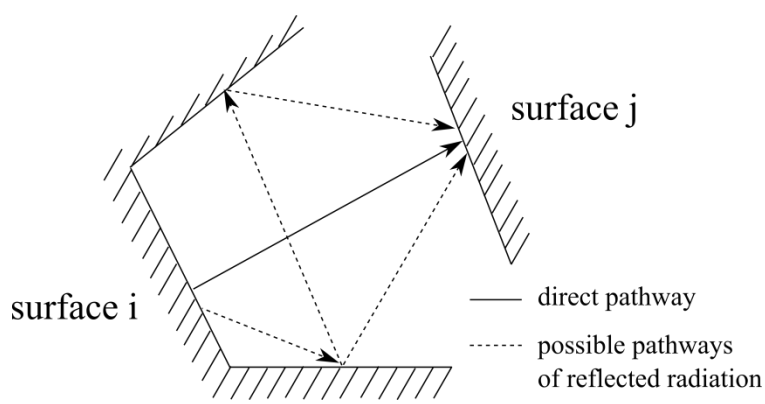

Figure 3.1 - Selected radiation pathways between surface i and j inside a general enclosure with reflective surfaces.

We will introduce two analytical methods to model the radiation heat transfer inside an enclosure with reflective surfaces. The first widely known technique is the Radiosity Method. An alternative way which is less popular but better suited for our purposes is a method which makes use of an extended view factor to account for reflection inside the enclosure.

3.2.1 Radiosity Method

For this method two new terms to describe the radiation heat transfer in an enclosure are introduced. The irradiation G_i is the radiative heat flux incident on a surface *i* , the radiosity J_i is the total radiative heat flux leaving surface *i*.

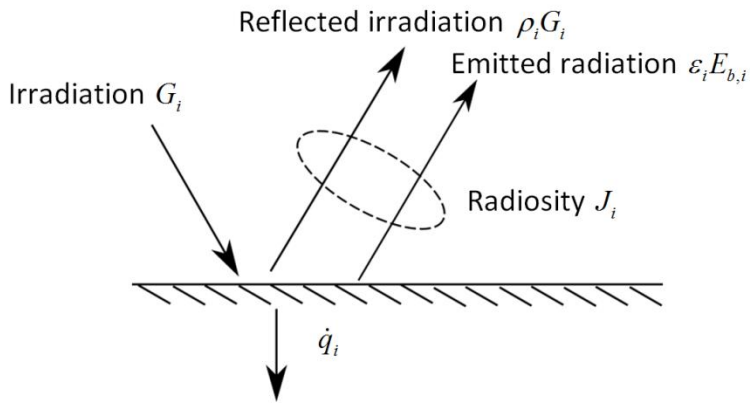

Figure 3.2 - Definition of radiosity for surface i - (Nellis, G. and Klein, S.A., 2009)

Radiosity is defined as the sum of reflected irradiation and emitted radiation leaving the surface.

$$J_i = \rho_i \cdot G_i + \varepsilon_i \cdot E_{b,i} \tag{3.13}$$

In Eqn. (3.13) ρ_i describes the reflectivity of surface *i*. For opaque surfaces, the reflectivity, absorptivity and emissivity are related by:

$$\rho_i = 1 - \alpha_i = 1 - \varepsilon_i \tag{3.14}$$

The radiation heat transfer to the gray surface *i* can be expressed as the difference between the total incoming radiation and the total radiation leaving surface *i*:

$$\dot{Q}_i = A_i \cdot J_i - A_i \cdot G_i \tag{3.15}$$

With Eqn.(3.13) and Eqn.(3.14) the new rate of radiation heat transfer to surface *i* (Eqn.(3.15)) can expressed as:

$$\dot{Q}_i = \left(\frac{\varepsilon_i \cdot A_i}{1-\varepsilon_i} \right) \cdot (E_{b,i} - J_i) \tag{3.16}$$

When modeling gray surfaces, the radiosity is the counterpart of the blackbody emissive power in blackbody radiation problems. The radiosity is the total amount of radiation leaving each surface that can interact with the surrounding surfaces. Therefore the heat transfer between two gray surfaces can be expressed as:

$$\dot{Q}_{i,j} = A_i \cdot F_{i,j} \cdot \left(J_i - J_j \right) \tag{3.17}$$

The view factors are the same as for the blackbody radiation. The reflected radiation on each surface is taken into account by using the radiosity, which includes both emissive and reflected radiation, instead of the emissive power. A general way to set up a system of equations to solve diffuse-gray surface radiation problems with *N* surfaces using the radiosity method is provided by Eqn. (3.18) and Eqn. (3.19).

$$\dot{Q}_i = \frac{\varepsilon_i \cdot A_i \cdot \left(E_{b,i} - J_i \right)}{\left(1-\varepsilon_i \right)} \text{ for } i = 1 \ldots N \tag{3.18}$$

$$\dot{Q}_i = A_i \cdot \sum_{j=1}^{N} F_{i,j} \cdot \left(J_i - J_j \right) \text{ for } i = 1 \ldots N \tag{3.19}$$

The radiosity method provides the only net heat transfer rate from a surface. The heat transfer rate from surface *i* to surface *j* cannot be determined using this method. Eqn. (3.18) and Eqn. (3.19) need to be solved simultaneously leading to an equation system with 2*N* equations that have to be solved in each iteration step.

3.2.2 The F-hat- Method

An alternative method to determine the net heat transfer between diffuse-gray surfaces in a cavity was developed by (Gebhart, 1957) and (Beckman, 1968), described in (Siegel R.and Howell J.R., 2002) and (Nellis, G. and Klein, S.A., 2009). The basic idea of this method is the extension of the concept of view factors to not only consider the direct radiation interaction between surfaces but also all radiation that is diffusely reflected by other surfaces inside the cavity along the radiation path between the two interacting surfaces. This extension of the view factor is here called the $\hat{F}$ - method following the description by (Nellis, G. and Klein, S.A., 2009).

$\hat{F}$ is defined as:

$$\hat{F}_{i,j} = \frac{\text{radiation leaving surface } i \text{ that falls directly or indirectly on surface } j}{\text{total radiation leaving surface } i} \tag{3.20}$$

$\hat{F}_{k,j}$ is calculated according to Eqn. (3.20). The first term on the right hand side is the view factor, which represents the fraction of radiation that leaves surface *i* and hits surface *j* directly. The product $\rho_k \cdot F_{i,k}$ represents the fraction of radiation that leaves surface *i* and is reflected from an intermediate surface *k*. Multiplied with $\hat{F}_{k,j}$ this product represents the radiation that originates from surface *i* and finally impinges on surface *j* as a result of reflection from intermediate surface *k*. All possible pathways from *k* to *j* are considered in the definition of $\hat{F}_{k,j}$.

$$\hat{F}_{i,j,\lambda} = F_{i,j} + \sum_{k=1}^{n} \rho_{k,\lambda} \cdot F_{i,k} \cdot \hat{F}_{k,j,\lambda} \quad \text{for } i = 1..N \text{ and } j = 1..N \tag{3.21}$$

The $\hat{F}$ parameter depends on the reflectivity of the surfaces and the view factors between all surfaces and therefore, on the geometric configuration of the enclosure. For black surfaces (emissivities = 1, no reflection) $\hat{F}_{i,j,\lambda}$ simplifies to the view factor, $F_{i,j}$.

Additional rules to find all required $\hat{F}_{i,j}$ can be stated, similar to Eqn. (3.2) and Eqn. (3.3). The *Enclosure Rule* states that all of the radiation emitted by a surface within an enclosure must strike another surface in the enclosure. For an enclosure consisting of *N* surfaces this rule can be written as (Nellis, G. and Klein, S.A., 2009):

$$\alpha_1 \cdot \hat{F}_{i,1} + \alpha_2 \cdot \hat{F}_{i,2} + ... + \alpha_N \cdot \hat{F}_{i,N} = 1 \tag{3.22}$$

For diffuse-gray surfaces: $\alpha_i = \varepsilon_i$ at all wavelengths (Kirchhoff's law) and therefore Eqn. (3.22) can be stated as:

$$\sum_{j=1}^{N} \varepsilon_j \cdot \hat{F}_{i,j} = 1 \tag{3.23}$$

Reciprocity also must be true for diffuse-gray surfaces as indicated in Eqn. (3.24). The derivation of this rule for the $\hat{F}$ - parameter is equivalent to the derivation done using the view factor in Section 3.1 (Nellis, G. and Klein, S.A., 2009).

$$\hat{F}_{i,j} \cdot A_i = \hat{F}_{j,i} \cdot A_j \tag{3.24}$$

With all $\hat{F}$ parameters determined the diffuse-gray radiation heat transfer problem can be solved. The net heat transfer rate between surface *i* and surface *j* is the difference between the heat transfer rate between the surfaces in both directions. Corresponding to Eqn. (3.4) the radiation heat transfer rate from surface *i* to surface *j* formulated with the $\hat{F}$ parameter method can be stated as:

$$\dot{Q}_{i,j} = \alpha_j \cdot \left(\varepsilon_i \cdot A_i \cdot \sigma \cdot T_i^4 \cdot \hat{F}_{i,j}\right) - \alpha_i \cdot \left(\varepsilon_j \cdot A_j \cdot \sigma \cdot T_j^4 \cdot \hat{F}_{j,i}\right) \tag{3.25}$$

The term $\left(\varepsilon_i \cdot A_i \cdot \sigma \cdot T_i^4\right)$ represents the radiation emitted by surface *i*. The term consists of the black body emissive power multiplied by the emissivity of the surface (ε_i). For a black surface the emissivity limits to 1, however for a gray surface only a part of the possible black body emitted radiation is emitted. The fraction of emitted radiation for a gray surface is represented by the emissivity of the surface. The emissivity is a property of the particular gray surface.

$\hat{F}_{i,j}$ represents the fraction of radiation incident on surface *j* coming from surface *i* by every possible radiation path, including interaction with other surfaces due to reflection. It incorporates emitted radiation and reflected radiation leaving surface *i* striking surface *j*. In comparison to the radiosity in Eqn. (3.19) , $\hat{F}_{i,j}$ combines the view factor and the radiosity. The absorptivity α_j is the fraction of incident radiation on surface *j* that is absorbed. Applying Kirchhoff's law (absorptivity equals emissivity), Eqn. (3.25) can be rearranged to:

$$\dot{Q}_{i,j} = \varepsilon_j \cdot \varepsilon_i \cdot \sigma \cdot \left(A_i \cdot T_i^4 \cdot \hat{F}_{i,j} - A_j \cdot T_j^4 \cdot \hat{F}_{j,i} \right) \tag{3.26}$$

Applying reciprocity in Eqn.(3.24) , Eqn.(3.26) can be stated as:

$$\dot{Q}_{i,j} = \varepsilon_j \cdot \varepsilon_i \cdot \sigma \cdot A_i \cdot \hat{F}_{i,j} \cdot \left(T_i^4 - T_j^4 \right) = \varepsilon_i \cdot \varepsilon_j \cdot \sigma \cdot A_j \cdot \hat{F}_{j,i} \cdot \left(T_i^4 - T_j^4 \right) \tag{3.27}$$

The overall radiation heat transfer to surface *i* can be stated as follows:

$$\dot{Q}_i = \varepsilon_i \cdot A_i \cdot \sigma \cdot \sum_{j=1}^{N} \varepsilon_j \cdot \hat{F}_{i,j} \cdot \left(T_i^4 - T_j^4 \right) \quad \text{for} \quad i = 1 \ldots N \tag{3.28}$$

Eqn. (3.28) provides N equations and $2 \cdot N$ unknowns (heat transfer rates $\dot{q}_i$ and temperatures T_i). The problem can be solved if the boundary conditions for each surface are known. The advantage of the $\hat{F}$ -Method is its structural similarity to the equations of the black surface radiation heat transfer (Eqn. (3.9)). The fact that the solving methods for both equations are equivalent simplifies the incorporation of the $\hat{F}$ -Method in the existing model. Similar to the blackbody model in Eqn. (3.9), Eqn. (3.28) calculates the heat transfer in one equation. The only variables that change in the iteration process are the surface temperatures. In contrast to the radiosity method, the $\hat{F}_{i,j}$ -Parameter itself is constant during the iteration process. The $\hat{F}$ -Method is expected to be more computationally effective than the radiosity method.

The $\hat{F}$ -Method as it was presented so far following the available literature ((Nellis, G. and Klein, S.A., 2009), (Siegel R.and Howell J.R., 2002)) only considers heat transfer rates from interacting surfaces that are part of the enclosure. In the existing cavity receiver model, there is an incoming solar flux that is distributed in a predefined manner on the cavity wall surfaces. Existing software described in Section 5.3 provides the solar flux distribution on the active surface heat exchanger walls. The passive surfaces include the top, bottom and lip; these surfaces do not receive direct solar flux. What follows is a modification of Eqn. (3.28)[1] to include the contribution of the solar flux. To incorporate solar flux in the $\hat{F}_{i,j}$ method, the term representing the radiation leaving surface *i* in Eqn. (3.25) has to be modified. $\hat{F}_{i,j}$, the corresponding enclosure rule and reciprocity remains unchanged as these quantities only depend on the geometric quantities and surface properties.

[1] Developed by Prof. Nellis (2010) at the Solar Energy Laboratory - University of Wisconsin

When there is a solar flux incident on a diffuse-gray surface, the radiation leaving surface *i* is:

$$\dot{Q}_{leaving\ i} = \underbrace{\varepsilon_i \cdot A_i \cdot \sigma \cdot T_i^4}_{\substack{\text{radiation emitted} \\ \text{by surface i}}} + \underbrace{Flux_{solar,i} \cdot A_i \cdot (1-\varepsilon_i)}_{\substack{\text{solar radiation reflected} \\ \text{by surface i}}} \tag{3.29}$$

The first term of Eqn. (3.29) represents the emitted radiation leaving surface *i* due to the temperature of the surface. The second term represents the reflected portion of the incident solar radiation striking surface *i* directly.

The radiation that leaves surface *i* and is absorbed by surface *j* by all possible radiation paths is:

$$\dot{Q}_{leaving\ i,\ absorbed\ by\ j} = \left[\varepsilon_i \cdot A_i \cdot \sigma \cdot T_i^4 + Flux_{solar,i} \cdot A_i \cdot (1-\varepsilon_i)\right] \cdot \hat{F}_{i,j} \cdot \alpha_j \tag{3.30}$$

Accordingly the radiation that leaves surface *j* and is absorbed by surface *i* can be stated. The net heat transfer rate between surface *i* and surface *j* is the difference between the absorbed radiation of each surface that was radiated by the other surface.

$$\begin{aligned} Q_{i,j} = &\left[\varepsilon_i \cdot A_i \cdot \sigma \cdot T_i^4 + Flux_{solar,i} \cdot A_i \cdot (1-\varepsilon_i)\right] \cdot \hat{F}_{i,j} \cdot \alpha_j \\ &- \left[\varepsilon_j \cdot A_j \cdot \sigma \cdot T_j^4 + Flux_{solar,j} \cdot A_j \cdot (1-\varepsilon_j)\right] \cdot \hat{F}_{j,i} \cdot \alpha_i \end{aligned} \tag{3.31}$$

With $\alpha_i = \varepsilon_i$ and $A_i \cdot \hat{F}_{i,j} = A_j \cdot \hat{F}_{j,i}$, Eqn. (3.31) can be rearranged to:

$$\dot{Q}_{i,j} = \varepsilon_i \cdot A_i \cdot \hat{F}_{i,j} \cdot \sigma \cdot \varepsilon_j \cdot \left(T_i^4 - T_j^4\right) + A_i \cdot \hat{F}_{i,j}\left[Flux_{solar,i} \cdot (1-\varepsilon_i) \cdot \varepsilon_j - Flux_{solar,j} \cdot (1-\varepsilon_j) \cdot \varepsilon_i\right] \tag{3.32}$$

The net radiation heat transfer to surface *i* can be obtained by summing Eqn. (3.32) for every surface j in the cavity:

$$\dot{Q}_i = \varepsilon_i \cdot A_i \cdot \sum_{j=1}^{N} \hat{F}_{i,j} \cdot \sigma \cdot \varepsilon_j \cdot \left(T_i^4 - T_j^4\right) + A_i \cdot \sum_{j=1}^{N} \hat{F}_{i,j}\left[Flux_{solar,i} \cdot (1-\varepsilon_i) \cdot \varepsilon_j - Flux_{solar,j} \cdot (1-\varepsilon_j) \cdot \varepsilon_i\right] \tag{3.33}$$

$$\text{for } i = 1 \ldots N$$

The modification of the $\hat{F}_{i,j}$ method results in an additional term in the radiation heat transfer equation. The first term, representing the emitted radiation and reflected radiation from surface *i* due to thermal radiation of the surfaces in the cavity, corresponds to Eqn. (3.28), it remains unchanged. The second term represents the influence of the solar flux on the heat exchanger

surfaces. Reflection and absorption effects due to the solar flux are taken into account with this second term.

3.2.3 Extension to Two Band Semi - Gray Surface Model

The thermal performance of solar receivers can be enhanced by applying surface coatings to the receiver that have high absorptivity for short wavelength (solar) radiation and low emissivity for radiation with long wavelength (thermal) radiation, as shown by (Pitz-Paal, R. et al., 1991) for a volumetric receiver. With selective coatings, thermal radiation loss can be reduced without significantly diminishing the absorbed solar input to the receiver. One approach to model these surface coatings is the implementation of a semi-gray surface approximation, for which emissivities are assumed to be constant within specific wavelength bands. . The model described in this paper uses a two-band approximation in which the emissivity for short wavelength solar radiation is assumed to have one value whereas the emissivity for long wavelength thermal radiation may have a different value. It is appropriate to represent the radiation properties in this manner for solar-thermal applications because solar and thermal radiation have characteristic maxima in separate wavelengths bands. The occurring overlap of the two radiation bands will be accounted for. This argument can be supported by calculating the reduced blackbody emissive power, E_b, according to Planck's spectral distribution of emissive power (Siegel R.and Howell J.R., 2002).

$$E_{b,reduced} = \frac{E_{b,\lambda}}{E_b} = \frac{C_1 \cdot \left[\lambda^5 \cdot \left(e^{\left(\frac{C_2}{\lambda \cdot T}\right)} - 1 \right) \right]^{-1}}{\sigma \cdot T^4} \tag{3.34}$$

To represent thermal radiation, the temperature T in Eqn. (3.34) is varied in the range of receiver surface temperature from 600-1300 K. Solar radiation is represented as radiation from a black surface at the average surface temperature of the sun, $T_{sun} \approx 5800$ K. C_1 and C_2 are constants that are equal to 3.742e8 W-µm^4/m^2 and 14388 µm-K, respectively. Varying the wavelength in Eqn. (3.34) returns the blackbody emissive power as a function of wavelength. These values are reduced by the total blackbody emissive power for all wavelengths at the particular surface temperature.

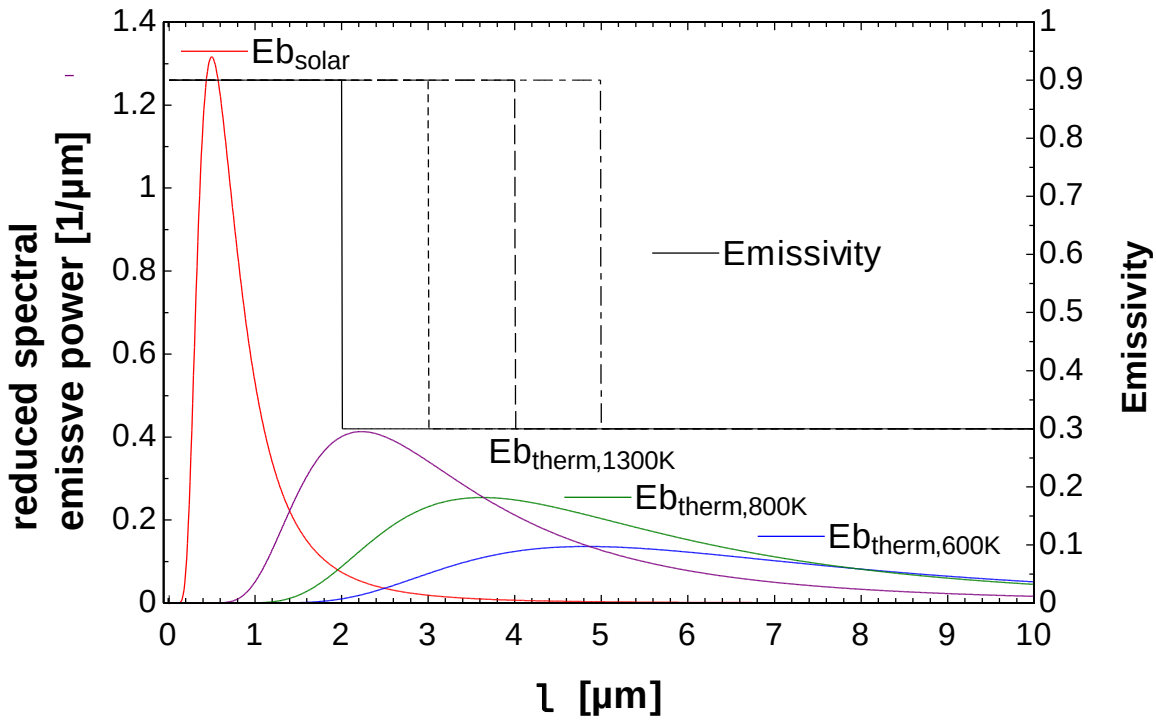

Figure 3.3 - Emissivity step in semi-gray heat transfer model.

The fractional function, given in Eqn. (3.35), provides the fraction of solar and thermal radiation within a specific wavelength band. Results are summarized for selected wavelengths bands in Table 3.a. This equation will later be used to consider the overlap of thermal and solar radiation in the heat transfer equations.

$$f_{0-\lambda_{step},T_s} = \frac{E_{b,0-\lambda_{step}}}{E_b} = \int_0^{\lambda_{step}} \frac{C_1}{\sigma T_s^4 \lambda \cdot \left(\exp\left(\frac{C_2}{\lambda T_s} \right) - 1 \right)} d\lambda \tag{3.35}$$

Emissivity step wavelength λ_{step}	$0-2\mu m$	$0-3\mu m$	$0-4\mu m$	$0-5\mu m$
Fraction of Solar Radiation; $f_{0-\lambda_{step},T_{sun}}$	94.03%	97.91%	99.04%	99.49%
Fraction of Thermal Radiation; $f_{0-\lambda_{step},800K}$	1.98%	14.02%	31.82%	48.07%
Fraction of Thermal Radiation; $f_{0-\lambda_{step},1200K}$	14.02%	40.35%	60.75%	73.78%
Fraction of Thermal Radiation; $f_{0-\lambda_{step},1500K}$	27.32%	56.43%	73.78%	83.44%

Table 3.a - Fraction of solar and thermal radiation within specific wavelengths bands

With: $$f_{\lambda_{step}-\infty,T_s} = 1 - f_{0-\lambda_{step},T_s} \tag{3.36}$$

The semi-gray surface approximation used in the cavity receiver models employs this two-band assumption. However, the method described in this section could be implemented with any number of bands, by considering more fraction band. The surface emissivities are varied for solar and thermal radiation separately, as indicated by subscripts solar and therm.

For the further development of the radiation model it is helpful to look at temperature driven radiation and reflected solar radiation in Eqn. (3.31) separately.

$$\begin{aligned}\dot{Q}_{i,j} = &\left[\varepsilon_i \cdot A_i \cdot \sigma \cdot T_{s,i}^4 + Flux_{solar,i} \cdot A_i \cdot \left(1-\varepsilon_i\right)\right] \cdot \hat{F}_{i,j} \cdot \alpha_j \\ &-\left[\varepsilon_j \cdot A_j \cdot \sigma \cdot T_{s,j}^4 + Flux_{solar,j} \cdot A_j \cdot \left(1-\varepsilon_j\right)\right] \cdot \hat{F}_{j,i} \cdot \alpha_i\end{aligned} \tag{3.31}$$

$$\begin{aligned}\dot{Q}_{thermal,i,j} = &\left[\varepsilon_i \cdot A_i \cdot \sigma \cdot T_{s,i}^4\right] \cdot \hat{F}_{i,j} \cdot \alpha_j \\ &-\left[\varepsilon_j \cdot A_j \cdot \sigma \cdot T_{s,j}^4\right] \cdot \hat{F}_{j,i} \cdot \alpha_i\end{aligned} \tag{3.37}$$

$$\begin{aligned}\dot{Q}_{solar,i,j} = &\left[Flux_{solar,i} \cdot A_i \cdot \left(1-\varepsilon_i\right)\right] \cdot \hat{F}_{i,j} \cdot \alpha_j \\ &-\left[Flux_{solar,j} \cdot A_j \cdot \left(1-\varepsilon_j\right)\right] \cdot \hat{F}_{j,i} \cdot \alpha_i\end{aligned} \tag{3.38}$$

The two band semi-gray model assumes constant emissivity within either wavelength band. Emissivity for wavelength from 0 to λ_{step} is considered the solar emissivity band denoted with the subscript 'solar'. The band for wavelength from λ_{step} to infinity is considered the thermal emissivity band, denoted with the subscript 'thermal'. These emissivity bands can be applied to Eqn. (3.37) and Eqn. (3.38). Because we deal with two emissivity bands we also need to use two sets of $\hat{F}$ - parameters, one for each emissivity band. Applying the two band model to Eqn. (3.37) , the temperature driven radiation that occurs in the thermal emissivity band can be stated as:

$$\begin{aligned}\dot{Q}_{thermal\ \text{in thermal emissivity band},i,j} = &\left(1 - f_{0-\lambda_{step},T_{s,i}}\right)\left[\varepsilon_{therm,i} \cdot A_i \cdot \sigma \cdot T_{s,i}^4\right] \cdot \hat{F}_{therm,i,j} \cdot \alpha_{therm,j} \\ &-\left(1 - f_{0-\lambda_{step},T_{s,j}}\right)\left[\varepsilon_{therm,j} \cdot A_j \cdot \sigma \cdot T_{s,j}^4\right] \cdot \hat{F}_{therm,j,i} \cdot \alpha_{therm.i}\end{aligned} \tag{3.39}$$

with $\left(1-f_{0-\lambda_{step},T_i}\right)$ indicating the fraction of temperature - driven radiation leaving surface *i* that occurs in the thermal emissivity band from λ_{step} to infinity. Accordingly the temperature driven radiation that occurs in the solar emissivity band can be stated as:

$$\begin{aligned}\dot{Q}_{thermal\ \text{in solar emissivity band},i,j} &= f_{0-\lambda_{step},T_{s,i}}\left[\varepsilon_{solar,i}\cdot A_i\cdot\sigma\cdot T_{s,i}^4\right]\cdot\hat{F}_{solar,i,j}\cdot\alpha_{solar,j}\\ &\quad - f_{0-\lambda_{step},T_{s,j}}\left[\varepsilon_{solar,j}\cdot A_j\cdot\sigma\cdot T_{s,j}^4\right]\cdot\hat{F}_{solar,j,i}\cdot\alpha_{solar.i}\end{aligned} \tag{3.40}$$

Note that for the different fractions of the total radiation, the according emissivity and $\hat{F}$ - parameter is used. Summing Eqn. (3.39) and Eqn. (3.40) leads to Eqn. the total temperature driven radiation heat transfer in both the thermal- and solar emissivity band.

$$\begin{aligned}\dot{Q}_{therm,i,j} &= \begin{bmatrix}\left(1-f_{0-\lambda_{step},T_{s,i}}\right)\left[\varepsilon_{therm,i}\cdot A_i\cdot\sigma\cdot T_{s,i}^4\right]\cdot\hat{F}_{therm,i,j}\cdot\alpha_{therm,j}\\ -\left(1-f_{0-\lambda_{step},T_{s,j}}\right)\left[\varepsilon_{therm,j}\cdot A_j\cdot\sigma\cdot T_{s,j}^4\right]\cdot\hat{F}_{therm,j,i}\cdot\alpha_{therm.i}\end{bmatrix}\\ &\quad + \begin{bmatrix} f_{0-\lambda_{step},T_{s,i}}\left[\varepsilon_{solar,i}\cdot A_i\cdot\sigma\cdot T_{s,i}^4\right]\cdot\hat{F}_{solar,i,j}\cdot\alpha_{solar,j}\\ -f_{0-\lambda_{step},T_{s,j}}\left[\varepsilon_{solar,j}\cdot A_j\cdot\sigma\cdot T_{s,j}^4\right]\cdot\hat{F}_{solar,j,i}\cdot\alpha_{solar.i}\end{bmatrix}\end{aligned} \tag{3.41}$$

Eqn. (3.41) can be simplified applying Kirchhoff's Law:

$$\begin{aligned}\dot{Q}_{therm,i,j} &= \sigma\cdot\varepsilon_{therm,i}\cdot\varepsilon_{therm,j}\cdot\left[\left(1-f_{0-\lambda_{step},T_{s,i}}\right)\cdot T_{s,i}^4\cdot A_i\cdot\hat{F}_{therm,i,j}-\left(1-f_{0-\lambda_{step},T_{s,j}}\right)\cdot T_{s,j}^4\cdot A_j\cdot\hat{F}_{therm,j,i}\right]\\ &\quad +\sigma\cdot\varepsilon_{solar,i}\cdot\varepsilon_{solar,j}\cdot\left[f_{0-\lambda_{step},T_{s,i}}\cdot T_{s,i}^4\cdot A_i\cdot\hat{F}_{solar,i,j}-f_{0-\lambda_{step},T_{s,j}}\cdot T_{s,j}^4\cdot A_j\cdot\hat{F}_{solar,j,i}\right]\end{aligned} \tag{3.42}$$

With the Reciprocity Rule Eqn. (3.42) can be stated as:

$$\begin{aligned}\dot{Q}_{therm,i,j} &= \sigma\cdot\varepsilon_{therm,i}\cdot\varepsilon_{therm,j}\cdot A_i\cdot\hat{F}_{therm,i,j}\cdot\left[\left(1-f_{0-\lambda_{step},T_{s,i}}\right)\cdot T_{s,i}^4-\left(1-f_{0-\lambda_{step},T_{s,j}}\right)\cdot T_{s,j}^4\right]\\ &\quad +\sigma\cdot\varepsilon_{solar,i}\cdot\varepsilon_{solar,j}\cdot A_i\cdot\hat{F}_{solar,i,j}\cdot\left[f_{0-\lambda_{step},T_{s,i}}\cdot T_{s,i}^4-f_{0-\lambda_{step},T_{s,j}}\cdot T_{s,j}^4\right]\end{aligned} \tag{3.43}$$

The steps taken to implement the semi-gray approximation for thermal radiation can be applied to the solar radiation equation(3.38):

$$\dot{Q}_{solar,i,j} = f_{0-\lambda_{step},T_{sun}} \cdot \begin{bmatrix} \left[Flux_{solar,i} \cdot A_i \cdot \left(1-\varepsilon_{solar,i}\right)\right] \cdot \hat{F}_{solar,i,j} \cdot \alpha_{solar,j} \\ -\left[Flux_{solar,j} \cdot A_j \cdot \left(1-\varepsilon_{solar,j}\right)\right] \cdot \hat{F}_{solar,j,i} \cdot \alpha_{solar,i} \end{bmatrix} + \left(1-f_{0-\lambda_{step},T_{sun}}\right) \cdot \begin{bmatrix} \left[Flux_{solar,i} \cdot A_i \cdot \left(1-\varepsilon_{therm}\right)\right] \cdot \hat{F}_{therm,i,j} \cdot \alpha_{therm,j} \\ -\left[Flux_{solar,j} \cdot A_j \cdot \left(1-\varepsilon_j\right)\right] \cdot \hat{F}_{therm,j,i} \cdot \alpha_{therm,i} \end{bmatrix} \tag{3.44}$$

In contrast to the temperature driven radiation equation the fraction of solar radiation does not depend on the surface temperatures but the temperature of the sun and therefore constant. Applying Kirchhoff's Law and Reciprocity leads to the simplification of Eqn. (3.44):

$$\dot{Q}_{solar,i,j} = f_{0-\lambda_{step},T_{sun}} \cdot \hat{F}_{solar,i,j} \cdot A_i \cdot \left[Flux_{solar,i} \cdot \left(1-\varepsilon_{solar,i}\right) \cdot \varepsilon_{solar,j} - Flux_{solar,j} \cdot \left(1-\varepsilon_{solar,j}\right) \cdot \varepsilon_{solar,i} \right] + \left(1-f_{0-\lambda_{step},T_{sun}}\right) \cdot \hat{F}_{therm,i,j} \cdot A_i \cdot \left[Flux_{solar,i} \cdot \left(1-\varepsilon_{therm,i}\right) \cdot \varepsilon_{therm,j} - Flux_{solar,j} \cdot \left(1-\varepsilon_{therm,j}\right) \cdot \varepsilon_{therm,i} \right] \tag{3.45}$$

Eqn. (3.43) and (3.45) are the governing radiation heat transfer equations in this model. Summing both equations in respect to *j* leads to the net radiation heat transfer of each type from surface *i*:

$$\dot{Q}_{therm,i} = \sigma \cdot \varepsilon_{therm,i} \cdot A_i \cdot \sum_{j=1}^{4N+4} \varepsilon_{therm,j} \cdot \hat{F}_{therm,i,j} \cdot \left[\left(1-f_{0-\lambda_{step},T_{s,i}}\right) \cdot T_{s,i}^4 - \left(1-f_{0-\lambda_{step},T_{s,j}}\right) \cdot T_{s,j}^4 \right] + \sigma \cdot \varepsilon_{solar,i} \cdot A_i \cdot \sum_{j=1}^{4N+4} \varepsilon_{solar,j} \cdot \hat{F}_{solar,i,j} \cdot \left[f_{0-\lambda_{step},T_{s,i}} \cdot T_{s,i}^4 - f_{0-\lambda_{step},T_{s,j}} \cdot T_{s,j}^4 \right] \tag{3.46}$$

$$\dot{Q}_{solar,i} = f_{0-\lambda_{step},T_{sun}} \cdot A_i \cdot \sum_{j=1}^{N} \hat{F}_{solar,i,j} \cdot \left[Flux_{solar,i} \cdot \left(1-\varepsilon_{solar,i}\right) \cdot \varepsilon_{solar,j} - Flux_{solar,j} \cdot \left(1-\varepsilon_{solar,j}\right) \cdot \varepsilon_{solar,i} \right] + \left(1-f_{0-\lambda_{step},T_{sun}}\right) \cdot A_i \cdot \sum_{j=1}^{N} \hat{F}_{therm,i,j} \cdot \left[Flux_{solar,i} \cdot \left(1-\varepsilon_{therm,i}\right) \cdot \varepsilon_{therm,j} - Flux_{solar,j} \cdot \left(1-\varepsilon_{therm,j}\right) \cdot \varepsilon_{therm,i} \right] \tag{3.47}$$

Combining thermal and solar radiation leads to the total semi-gray radiation heat transfer between to surfaces in the cavity.

$$\dot{Q}_{radiaiton,i} = \sigma \cdot \varepsilon_{therm,i} \cdot A_i \cdot \sum_{j=1}^{4N+4} \varepsilon_{therm,j} \cdot \hat{F}_{therm,i,j} \cdot \left[\left(1 - f_{0-\lambda_{step},T_{s,i}}\right) \cdot T_{s,i}^4 - \left(1 - f_{0-\lambda_{step},T_{s,j}}\right) \cdot T_{s,j}^4 \right]$$
$$+ \sigma \cdot \varepsilon_{solar,i} \cdot A_i \cdot \sum_{j=1}^{4N+4} \varepsilon_{solar,j} \cdot \hat{F}_{solar,i,j} \cdot \left[f_{0-\lambda_{step},T_{s,i}} \cdot T_{s,i}^4 - f_{0-\lambda_{step},T_{s,j}} \cdot T_{s,j}^4 \right]$$
$$+ f_{0-\lambda_{step},T_{sun}} \cdot A_i \cdot \sum_{j=1}^{N} \hat{F}_{solar,i,j} \cdot \left[Flux_{solar,i} \cdot \left(1 - \varepsilon_{solar,i}\right) \cdot \varepsilon_{solar,j} - Flux_{solar,j} \cdot \left(1 - \varepsilon_{solar,j}\right) \cdot \varepsilon_{solar,i} \right]$$
$$+ \left(1 - f_{0-\lambda_{step},T_{sun}}\right) \cdot A_i \cdot \sum_{j=1}^{N} \hat{F}_{therm,i,j} \cdot \left[Flux_{solar,i} \cdot \left(1 - \varepsilon_{therm,i}\right) \cdot \varepsilon_{therm,j} - Flux_{solar,j} \cdot \left(1 - \varepsilon_{therm,j}\right) \cdot \varepsilon_{therm,i} \right]$$
(3.48)

3.2.4 Multi Band Semi - Gray Surface Model

The radiation model in Section 3.2.3 considers two emissivity bands, one approximating solar radiation in a short wavelength band and thermal radiation in a long wavelength band. The model can however easily be extended to consider more than these two emissivity bands. Consider the thermal radiation heat transfer in Eqn. (3.43). Each of the two terms of the equation respresents one of the emissivity bands. Consequently, each emissivity band requires a set of surface emissivities, the corresponding $\hat{F}$ -parameters and fractions of temperature driven radiation and solar radiation within that band. For each emissivity band one term needs to be added to the equation. Assuming K bands, the temperature driven radiation in Eqn. (3.43) can then be stated as:

$$\dot{Q}_{therm,i,j} = \sigma \cdot \sum_{k=2}^{K-1} \left[\begin{array}{l} \varepsilon_{therm,i,k} \cdot \varepsilon_{therm,j,k} \cdot \left[f_{\lambda_{step,k}-\lambda_{step,k+1},T_{s,i}} \cdot T_{s,i}^4 \cdot A_i \cdot \hat{F}_{therm,i,j,k} - f_{\lambda_{step,k}-\lambda_{step,k+1},T_{s,j}} \cdot T_{s,j}^4 \cdot A_j \cdot \hat{F}_{therm,j,i,k} \right] \\ + \varepsilon_{solar,i,k} \cdot \varepsilon_{solar,j,k} \cdot \left[f_{\lambda_{step,k-1}-\lambda_{step,k},T_{s,i}} \cdot T_{s,i}^4 \cdot A_i \cdot \hat{F}_{solar,i,j} - f_{\lambda_{step,k-1}-\lambda_{step,k},T_{s,j}} \cdot T_{s,j}^4 \cdot A_j \cdot \hat{F}_{solar,j,i,k} \right] \end{array} \right]$$
(3.49)

The fractions are not calculated from $0 - \lambda_{step}$ and $\lambda_{step} - \infty$ as it was done for the two band model but from $\lambda_{step,k-1} - \lambda_{step,k}$ and $\lambda_{step,k} - \lambda_{step,k+1}$. The first wavelength for $k = 1$ is 0 the last wavelength step for $k = K$ is infinity. The steps taken to derive Eqn. (3.49) from Eqn. (3.43) for thermal radiation can be also applied to the solar radiation heat transfer in Eqn. (3.45).

$$\dot{Q}_{solar,i,j} = \sum_{k=2}^{K-1} \left[\begin{array}{l} f_{\lambda_{step,k-1}-\lambda_{step,k},T_{sun}} \cdot \hat{F}_{solar,i,j,k} \cdot A_i \cdot \left[Flux_{solar,i} \cdot \left(1-\varepsilon_{solar,i,k}\right) \cdot \varepsilon_{solar,j,k} - Flux_{solar,j,k} \cdot \left(1-\varepsilon_{solar,j,k}\right) \cdot \varepsilon_{solar,i,k} \right] \\ + f_{\lambda_{step,k}-\lambda_{step,k+1},T_{sun}} \cdot \hat{F}_{therm,i,j,k} \cdot A_i \cdot \left[Flux_{solar,i} \cdot \left(1-\varepsilon_{therm,i,k}\right) \cdot \varepsilon_{therm,j,k} - Flux_{solar,j,k} \cdot \left(1-\varepsilon_{therm,j,k}\right) \cdot \varepsilon_{therm,i,k} \right] \end{array} \right] \tag{3.50}$$

With Eqn. (3.49) and (3.50) multiple emissivity bands can be used to approximate the emissivity of a surface as a function of wavelength. There is no systematical limit for the number of emissivity bands that can be modeled with this method. Because every band requires a set of $\hat{F}$ -parameters with N^2 values (N being the number of interacting surfaces in the enclosure) the number of variables increases significantly with the number of emissivity bands. For many emissivity bands this might lead to problems in the computational process required to solve the equations provided by this method.

4 Convective Heat Loss

Convective heat losses of a solar central receiver cannot be assumed as negligible; therefore, convective losses need to be considered for the cavity receiver thermal model. The accurate description and modeling of convective losses in cavity receivers is a complex problem and subject of research. Because of the complexity the physics of free and forced convective flow in a cavity bring with them an analytical solution of this problem is not possible. Numerical simulation using computational fluid dynamics (CFD) is not appropriate to be applied to a cavity model like it is used in this work because of the complexity. Without experimental verification the reliability of CFD-simulation is highly questionable. We will discuss the possibility to measure convective losses of a cavity receiver and will show that it is a very complex field itself that does not promise to provide accurate results that could be used to verify complex models. What is left to approximate the convective losses are semi-empirical or empirical convection correlations.

While there are a number of natural convection correlations for small cavity receivers. There are no correlations that are reliably applicable to large cavities that are typically used in solar towers.

Because of the shading effect of the cavity one of the expected advantages of this type of receiver is the reduction of convection loss, in particular the forced convection component caused by wind effects. The effect of wind induced forced convection is strongly dependent on the wind direction and the shape of the tower itself. There are some numerical studies[2] that model wind effects on cavity receivers but the results are limited to a specific receiver geometry and not directly applicable to our receiver model. Forced convection will be considered in our model using a very simplified approach by (Siebers, D. and Kraabel, J., 1984).

[2] (Fang, J.B. et al., 2011), (Prakash, M. et al., 2008)

4.1 Convective Heat Loss Regime of the Cavity Receiver

There are two convection modes that can be of importance in a solar central cavity receiver, natural convection driven by temperature induced buoyancy gradients and forced convection due to wind. The importance of natural convection in comparison to forced convection for the cavity receiver geometry has to be evaluated in order to reliably predict the total heat loss.

An important parameter to characterize natural convection is the Grashof number. It approximates the ratio of buoyancy to viscous force acting on a flow, and is therefore an indicator if a flow is driven by buoyancy or external effects. The Grashof number is defined in Eqn. (4.1) with g the gravitation constant, β the volumetric expansion factor, ν the kinematic viscosity and *L* the characteristic length of the receiver:

$$Gr_L = \frac{g\beta\left(T_{wall} - T_\infty\right)L^3}{\nu^2} \hat{=} \frac{\text{buoyancy effects}}{\text{viscous effects}} \approx \frac{\text{natural convection}}{\text{forced convection}} \tag{4.1}$$

Another important parameter for forced convection flow is the Reynolds number which relates the inertial forces to the viscous forces of the flow. In this case, the inertial forces are driven by the local wind velocity; therefore, the Reynolds number is given by:

$$\mathrm{Re} = \frac{u_{wind} \cdot L}{\nu} \tag{4.2}$$

(Nellis, G. and Klein, S.A., 2009) show that, for natural convection, the buoyancy induced flow velocity can be approximated by:

$$u_{char,nc} = \sqrt{gL\beta\left(T_{wall} - T_\infty\right)} \tag{4.3}$$

Substituting Eqn. (4.3) in Eqn. (4.2) leads to the Reynolds number of the buoyancy driven flow when no momentum is induced:

$$\mathrm{Re}_{nc} = \frac{u_{char,nc} \cdot L}{\nu} = \frac{L \cdot \sqrt{gL\beta\left(T_{wall} - T_\infty\right)}}{\nu} \tag{4.4}$$

If only natural convection is considered, the square of the Reynolds number is equal to the Grashof number:

$$\mathrm{Re}_{nc}^2 = \left(\frac{\sqrt{L^2 \cdot gL\beta\left(T_{wall} - T_\infty\right)}}{\nu} \right)^2 = \frac{gL^3\beta\left(T_{wall} - T_\infty\right)}{\nu^2} = Gr_L \tag{4.5}$$

Consequently the ratio of the Grashof number to the square of the Reynolds number is a useful indicator of the driving forces of the flow and therefore what kind of convection mechanism has to be considered in transfer model. This ratio is also called Richardson number $Ri = \frac{Gr}{\mathrm{Re}^2}$.

$\frac{Gr}{\mathrm{Re}^2} >> 1$ <u>Natural convection</u> is dominant, forced convection can be neglected.

$\frac{Gr}{\mathrm{Re}^2} \approx 1$ Mixed convection <u>where</u> both natural and forced convection are considered.

$\frac{Gr}{\mathrm{Re}^2} << 1$ <u>Forced convection</u> is dominant, natural forced convection can be neglected

Our cavity receiver model predicts wall temperatures in the range of 800-1500 K. Figure 4.1 shows the Richardson number as a function of the wind velocity with wall temperature as a parameter. All properties are determined at film temperature, which is the mean of film- and ambient temperature. It can be seen that for wind velocities below 5 m/s, natural convection is the dominant mechanism of convective heat transfer, forced convection is an insignificant influence. With increasing velocity forced convection becomes an increasingly significant mechanism of convective heat transfer. For wind velocities between 6-20 m/s, a mixed convection heat transfer regime has to be considered because natural and forced convection are of the similar magnitude and are influencing each other. For wind velocities higher than 25 m/s, only forced convection can be considered. For wind velocities this high, natural convection is an insignificant influence.

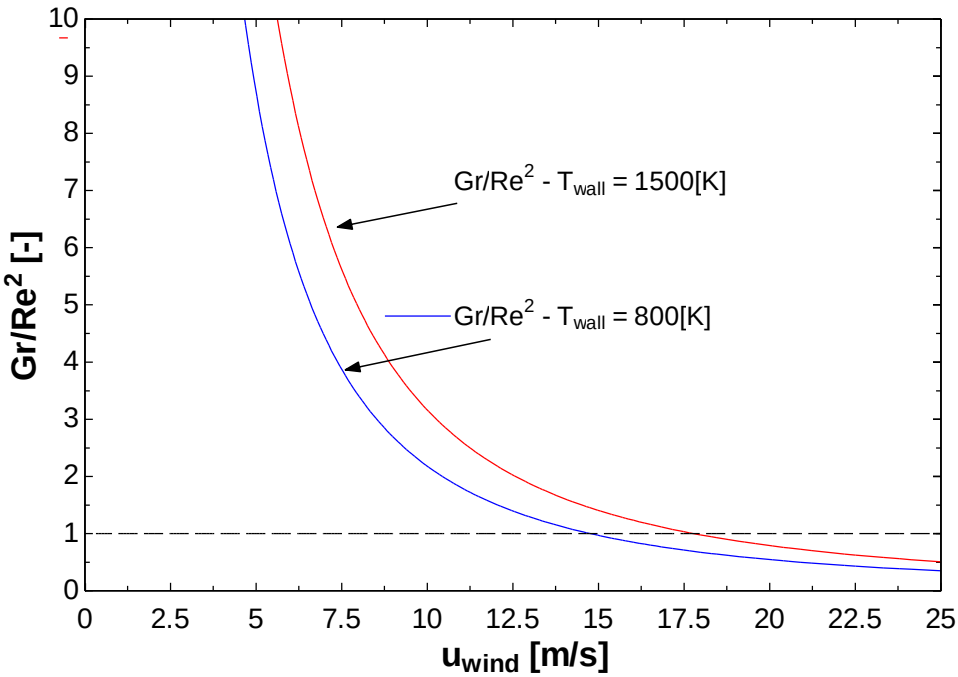

Figure 4.1 – Richardson number of the cavity receiver vs. wind velocity

Figure 4.2 shows a histogram of the wind velocity for the location, Blythe CA, which are used for the annual simulation in TRNSYS(Klein, S.A. et al., 2007). Wind data is usually measured in heights of 40m, 25m and 10m (Bailey, B.H., McDonald, S.L, 1997). The cavity receiver is mounted at the top of the solar tower with 312m height. To account for the increasing wind velocity with increased elevation the correlation in Eqn.(4.6) from (Duffie, J. A., Beckman, W.A., 2006) is used. The subscript one denotes the measuring conditions and the subscript two the elevated conditions. The data was measured at a height of 10 m.

$$\frac{u_1}{u_2} = \left(\frac{z_1}{z_2}\right)^{0.14} \tag{4.6}$$

Figure 4.2 shows that a significant time of the year the wind velocity is low enough so that forced convection is not expected to have a dominating influence on the convection heat loss mechanism inside the cavity. The majority of the year wind velocities are of a magnitude that forced convection needs to be considered in from of a mixed convection regime. The wind never exceeds wind velocities of 20 m/s, natural convection is a significant convection mechanism over the full range of observed wind speeds.

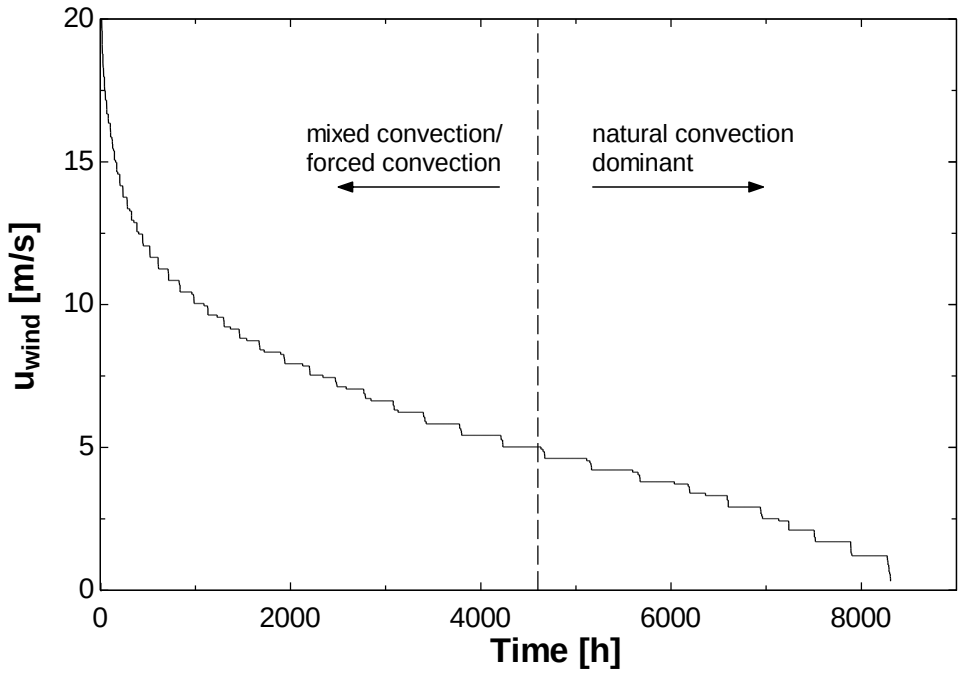

Figure 4.2 – Wind velocity at the tower from TMY-data – Blythe, CA

Consequently natural and mixed convection needs to be considered to in the thermodynamic model of the cavity receiver. For the application in this model it is the convection loss will be estimated using correlations. There are several physical conditions and properties of a solar central cavity receiver that limit the applicability of existing convection correlations.

Additionally to the Grashof number in Eqn. (4.1), other non-dimensional characteristics are used to describe natural convection loss. The Prandtl number in Eqn. (4.7) represents the ratio of viscous diffusion rate to thermal diffusion rate. This ratio represents the importance of convective to conductive heat transfer in a fluid.

$$\Pr = \frac{\nu}{\alpha} = \frac{c_p \mu}{k} \tag{4.7}$$

Many natural convection correlation use the Rayleigh number as the dominating parameter to characterize the fluid properties and heat transfer condition:

$$Ra = Gr \cdot \Pr \tag{4.8}$$

Typically correlations are developed to represent a certain a range of fluid properties and heat transfer conditions. Using a correlation outside of this range leads to unverified, in some cases

non-physical results. The range of validity is usually defined by one or more of the mentioned non-dimensional numbers and/or for a range of temperature ratios between wall temperature and ambient temperature.

Characteristics	**Range**
Characteristic length = receiver height H_{Rec}	$23.65m$
Temperature ratio: $\frac{T_{wall}}{T_{amb}}$	$\approx 1.8-3.4$
Prandtl number: $\mathrm{Pr}=\frac{\nu}{\alpha}$	$0.7<\mathrm{Pr}<0.71$
Grashof number: $Gr=\frac{g\beta\rho^2\left(T_W-T_\infty\right)H_{\mathrm{Rec}}{}^3}{\mu^2}$	$2.8\cdot 10^{13}<Gr<1.1\cdot 10^{14}$
Rayleigh number: $Ra=\mathrm{Pr}\cdot Gr$	$2.8\cdot 10^{13}<Ra<7.8\cdot 10^{13}$
Reynolds number: $\mathrm{Re}_{nc}=\frac{\rho H_{\mathrm{Rec}}}{\mu}\sqrt{gH_{\mathrm{Rec}}\beta\left(T_W-T_\infty\right)}$	$1.5\cdot 10^7 < \mathrm{Re} < 2.8\cdot 10^7$

Table 4.a - Characteristic receiver parameters

4.2 Natural Convection Correlations

Some important characteristics of the cavity receiver are given in Table 4.a. Because of the size of the cavity receiver the characteristic length used for the Grashof and Rayleigh number is large leading to comparably large numbers. The surface temperatures of the cavity receiver can go up to 1300K resulting in very high temperature ratios. Because of these conditions the fully developed natural convection flow regime is turbulent. Many cavity correlations consider laminar flow. These demanding natural convection condition in the receiver exceed the range of validation of most correlations.

Property data for most correlations is determined at the film temperature, Eqn. (4.9).

$$T_{film} = \frac{T_{wall} + T_{amb}}{2} \tag{4.9}$$

For very high wall temperatures it is questionable if the mean of ambient and wall temperature represents the fluid temperature close to the wall or if a temperature weighted closer to the wall temperature would be more appropriate. Current correlations however use the film temperature.

4.2.1 Clausing (1983)

This correlation is based on the work presented in (Clausing, 1981) and (Clausing, 1983). The underlying idea of semi-analytical approach to model convective losses from a cavity receiver is shown in Figure 4.3.

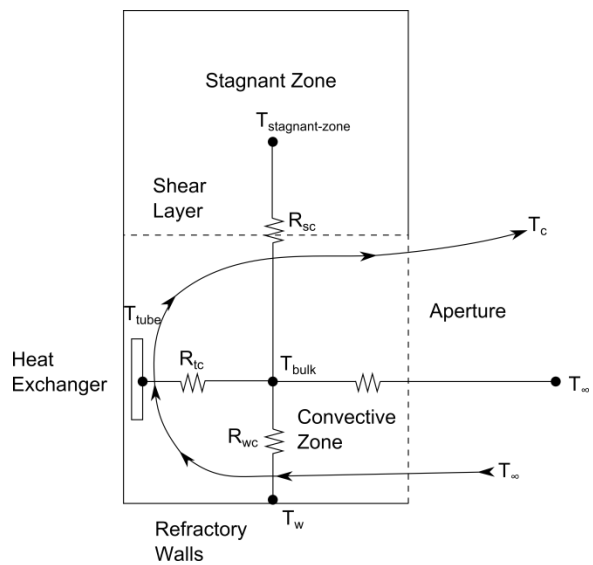

Figure 4.3 - Network representation of the convection loss mechanism – from (Clausing, 1983)

Clausing describes the convection heat loss of a cavity using a resistance network. A stagnant zone is assumed to develop at the top of the receiver due to the large density gradient of air within the cavity. The stagnant zone, confined by the cavity walls, the ceiling and lip is assumed to experience no convection losses. Instead, the heat exchange between the stagnant zone and the bulk flow inside the convective zone is assumed to be by conduction.

The resulting heat transfer equation considering heat transfer from each surface inside the cavity to the bulk flow is given in Eqn. (4.10).

$$\begin{aligned}\dot{Q}_{conv,total} &= \frac{T_{tube}-T_{bulk}}{R_{tc}} + \frac{T_{wall}-T_{bulk}}{R_{wc}} + \frac{T_{stagnantzone}-T_{bulk}}{R_{sc}} \\ &= h_t A_t \left(T_{tube}-T_{bulk}\right) + h_w A_w \left(T_{wall}-T_{bulk}\right) + h_s A_s T_{stagnantzone} - T_{bulk}\end{aligned} \tag{4.10}$$

To complete the system of equations, an energy balance of the convective air flow is used, Eqn.(4.11).

$$\dot{Q}_{aperature} = \left(\rho_\infty u_a A_a\right) c_p \left(T_c - T_\infty\right) \tag{4.11}$$

With u_a an effective flow velocity which is the quadratic mean of wind velocity (u_{wind}) and buoyancy induced velocity (u_b).

$$u_a = 0.5\left[u_b^2 + \left(\frac{u_{wind}}{2}\right)^2\right]^{0.5} \tag{4.12}$$

$$u_b = \left[g\beta\left(T_c - T_\infty\right)L_a\right]^{0.5} \tag{4.13}$$

Although this equation suggests that forced convection effects are considered in this model, Clausing emphasizes that this correlation is only valid when u_{wind} and u_b are of the same magnitude and internal resistances dominate the heat transfer situation. Eqn. (4.12) has no theoretical basis and cannot be interpreted as including wind effects in the convective loss mechanism.

The convection heat transfer coefficients needed to solve Eqn.(4.10) and (4.11) are given in (Clausing, 1983). Data from a small scale experiment (LeQuere, et al., 1981) are used to fit Nusselt number correlations to the model. The Nusselt number is determined as a function of Rayleigh number, wall- and ambient temperature and the surface orientation $\mathrm{z}\left(\mathrm{Z_w}\right)$, Eqn. (4.14).

$$Nu = 0.082 \cdot Ra^{1/3}\left[-0.9 + 2.4\left(\frac{T_w}{T_\infty}\right) - 0.5\left(\frac{T_w}{T_\infty}\right)^2\right] \cdot \mathrm{z}\left(\mathrm{Z_w}\right) \tag{4.14}$$

For vertical and horizontal upward facing surfaces, the correction factor for surface orientation $\mathrm{z}\left(\mathrm{Z_w}\right)$ is unity.

$$\begin{aligned} &\mathrm{z}\left(Z_W\right) = 1\,,\ \ 0 \le Z_w \le 135\,\mathrm{deg} \\ &Z_w \rightarrow \text{ wall zenith angle ; } \mathrm{z}\left(\mathrm{Z_w}\right) \rightarrow \text{ correction factor for surface orientation} \end{aligned} \tag{4.15}$$

For horizontal downward facing surfaces such as the cavity ceiling, the correction factor is 2/3.

$$\mathrm{z}\left(Z_W\right)=1\,,\quad 0\le Z_w\le 135\,\mathrm{deg}$$
$$\mathrm{z}\left(Z_W\right)=\tfrac{2}{3}\left[1+\frac{\sin\left(\mathrm{Z_W}\right)}{\sqrt{2}}\right],\quad Z_w>135\,\mathrm{deg} \tag{4.16}$$
$$\text{For } Z_W\left(180\,\mathrm{deg}\right)=\tfrac{2}{3}\text{ - downward facing heated surface}$$

Also, based on the experimental results (LeQuere et al 1981), the heat exchange surface between stagnant zone and convective zone is reduced to 30% of its actual geometric value:

$$A_{stagnant}=0.3\cdot A_{\text{cross-section}} \tag{4.17}$$

Clausing points out that this approach is based on one data point. Although this model best represents the geometry of our cavity receiver and also provides the most detailed information about the convection loss, in our application it is slightly out of the valid range. According to Clausing, this model is valid for $Ra>1.6\cdot 10^9$ and $1<T_W/T_\infty<2.6$.

4.2.2 Clausing (1987)

The correlations derived by (Clausing, 1987) are based on an experimental investigation of smooth, isothermal cubic small-scale cavities; with focus on influence of the shape of the side facing opening. The measurements were performed in a cryogenic wind tunnel with air temperatures ranging from 80K to 310K. In this way, the large Rayleigh numbers and the large temperature ratios between wall and ambient temperature, which are characteristic for large solar receivers, could be realized for a small 0.4 m-cubic cavity. Another advantage of the low ambient temperature is the surface temperature also can be set to comparably low values, reducing radiation loss and therefore decreasing uncertainty of the measurements. The correlation is deduced from a dimensional analysis of the governing equations of natural convection. Simplifying assumptions are laminar flow of a Newtonian fluid, ideal gas, negligible viscous dissipation and negligible work done by compression. Clausing also based this correlation on the previously introduced understanding of the cavity consisting of a stagnant and a convective zone. This leads to the following correlation:

$$Nu = \frac{hL_c}{k} = \frac{\dot{Q} \cdot L_c}{A_{convective-zone}\left(T_w - T_\infty\right)k} = g \cdot f \cdot b \tag{4.18}$$

g represents the natural convection correlation from the internal cavity surfaces to the surroundings for constant properties. f is the quantity which accounts for variable property influences because of the difference of wall- and ambient temperature. b accounts for effects that occur when the bulk temperature T_b is significantly different than T_∞.

The other two factors are depending on the flow regime. Clausing provides the following equations to determine these variables:

<u>Laminar</u> - regime I for: $Ra < 3.8 \times 10^8 \equiv Ra_{\text{laminar}}$	$g = 0.63 Ra^{1/4}$ $f_{\text{laminar}} = 1$
<u>Transitional</u> - regime II for: $\text{Ra}_{\text{laminar}} < Ra < 1.6 \times 10^9 \equiv \text{Ra}_{\text{turb}}$	$g = 0.63 Ra^{1/4}$ $f_{transistion} = \left(f_{turb} - 1\right) \cdot \left[\frac{Ra^{1/3} - \text{Ra}_{\text{lam}}^{1/3}}{Ra_{turb}^{1/3} - \text{Ra}_{\text{lam}}^{1/3}}\right] + 1$
<u>Turbulent</u> - regime III for: $Ra > 1.6 \times 10^9 \equiv \text{Ra}_{\text{turb}}$	$g = 0.108 Ra^{1/3}$ $f_{turb} = 0.2524 + 0.9163 \cdot \left(\frac{T_W}{T_\infty}\right) - 0.1663 \cdot \left(\frac{T_W}{T_\infty}\right)^2$

Table 4.b – Heat transfer correlations for different flow regimes, (Clausing, 1987)

b is given as:

$$b = 1 - 1.57\left[\frac{g \cdot f \cdot b\left(\frac{k_f}{k_\infty}\right)}{\left(Ra_\infty \cdot \text{Pr}_\infty \cdot \frac{L_a}{L_c}\right)^{1/2} \cdot \left(\frac{A_a}{A_{convective-zone}}\right)}\right]^{2/3} \tag{4.19}$$

All properties are evaluated at film temperature defined as the mean of wall and ambient temperature. In this case, the characteristic length is the aperture height plus half of the total cavity height.

$$L_c = L_{ap} + \frac{L}{2} \tag{4.20}$$

The area $A_{convective-zone}$ includes all surfaces that are not in the stagnant zone and the aperture area. The correlations are valid for $1 < T_W / T_\infty < 3$; $L^2/18 \leq A_a \leq L^2$ and $3\times10^7 < Ra < 3\times10^{10}$.

4.2.3 Siebers and Kraabel (1984)

(Siebers, D. and Kraabel, J., 1984) developed convection loss correlations for both cylindrical, external- and cavity receivers. The correlations are based on experimental data from large and small scale experiments and information, available in literature at that time.

The cavity receiver correlation, in particular, is based on a larger-scale cavity experiment (2.2 m high) and two small scale experiments with a height of 0.2m and 0.6m. The correlation in Eqn. (4.21) gives the total natural convection loss of a simple cavity for $10^5 < Gr < 10^{12}$.

$$Nu_l = 0.088 \cdot Gr_l^{1/3} \left(\frac{T_w}{T_\infty} \right)^{0.18} \tag{4.21}$$

Due to the $1/3$ exponent of the Grashof number, the authors claim that correlation is independent of the length scale. Comparing the results of the three experiments to results in (Siebers, D. and Kraabel, J., 1984), the authors claim that the heat transfer coefficient is independent of cavity size. The correlation is therefore also significant for larger cavities, although it is based on comparably small cavities.

The properties in Eqn. (4.21) are determined at <u>ambient temperature</u>. For air at normal ambient temperatures, an equivalent formulation of Eqn. (4.21) is given by the authors as:

$$h_{nc,0} = 0.81 \cdot \left(T_w - T_\infty \right)^{0.426} \tag{4.22}$$

T_w is the area-averaged wall temperature of the cavity. To account for partial covering of the cavity opening such as a lower and upper lip the following correction is used:

$$h_{nc} = h_{nc,0} \cdot \underbrace{\left(\frac{A_1}{A_2}\right)}_{\text{accounts for lower lip}} \underbrace{\left(\frac{A_3}{A_1}\right)^{0.63}}_{\text{accounts for upper lip}} \tag{4.23}$$

with A_1 being the total cavity surface, A_2 being the cavity surface area excluding the area of the lower lip and A_3 being the cavity surface area excluding the area of the upper lip.

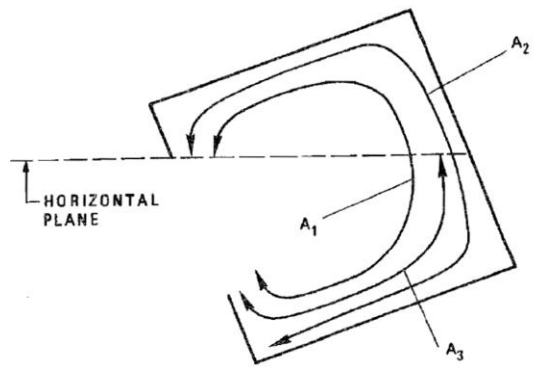

Figure 4.4 - Cavity orientation, from (Siebers, D. and Kraabel, J., 1984)

As shown in Figure 4.4, Eqn. (4.23) can be used to account for inclination of the cavity as well.

Another important finding by (Siebers, D. and Kraabel, J., 1984) is that for natural convection, the heat transfer coefficients of large cavity experiments are similar to those of large vertical flat plates. This is shown in Figure 4.5, the measured natural convection heat transfer for a vertical flat plate agrees well with the measured and calculated heat transfer coefficients of large cavities.

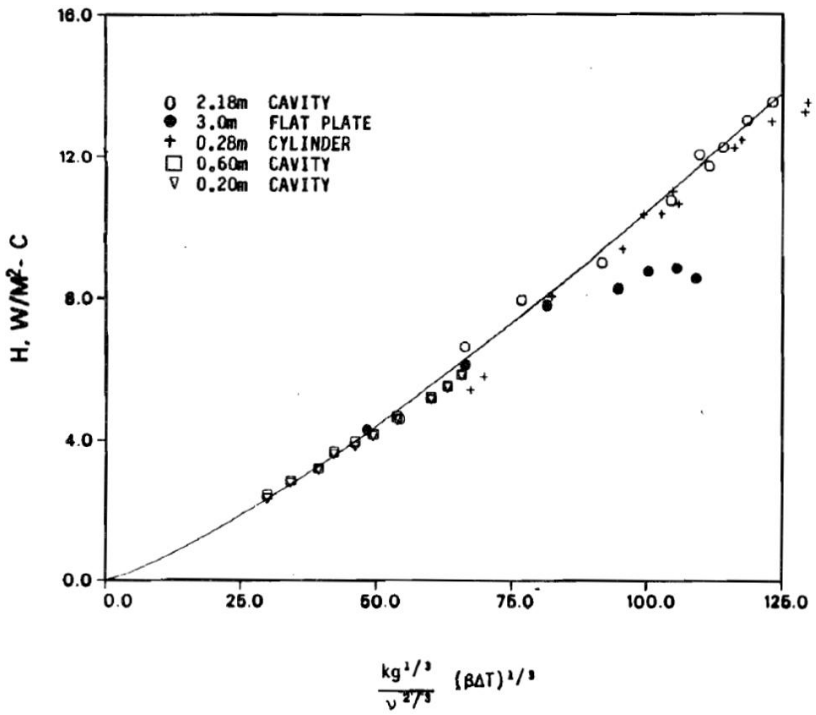

Figure 4.5 - Comparison of cavity- and vertical plate correlations (Siebers, D. and Kraabel, J., 1984)

4.2.4 Paitoonsurikarn & Lovegrove (2006)

The natural convection correlation by (Paitoonsurikarn, S. and Lovegrove K., 2006) is developed for an open-cavity receiver in solar dish application. These receivers are generally much smaller (L_{char}<1m) and have a different shape than central receiver in solar tower applications. Another difference is that inclination is an important influence on the convection losses for these receivers. Central receivers in solar tower have a constant inclination and are generally horizontal or nearly horizontal. Apart from these differences, these cavities are similar in many thermodynamic characteristics such as the high ratio between surface temperature and ambient temperature. The authors based this convection correlation on experiments on three different cavity geometries on being a small scale experiment and the others full scale experiments. A numerical simulation was done and verified with the experimental data. The authors claim that the correlation predicts 50% of the data within 20% and 90% of the data within 50% deviation, for all tested geometries. For the cavity geometries shown in the figure below experimental data were used to test, deduce and verify the correlation.

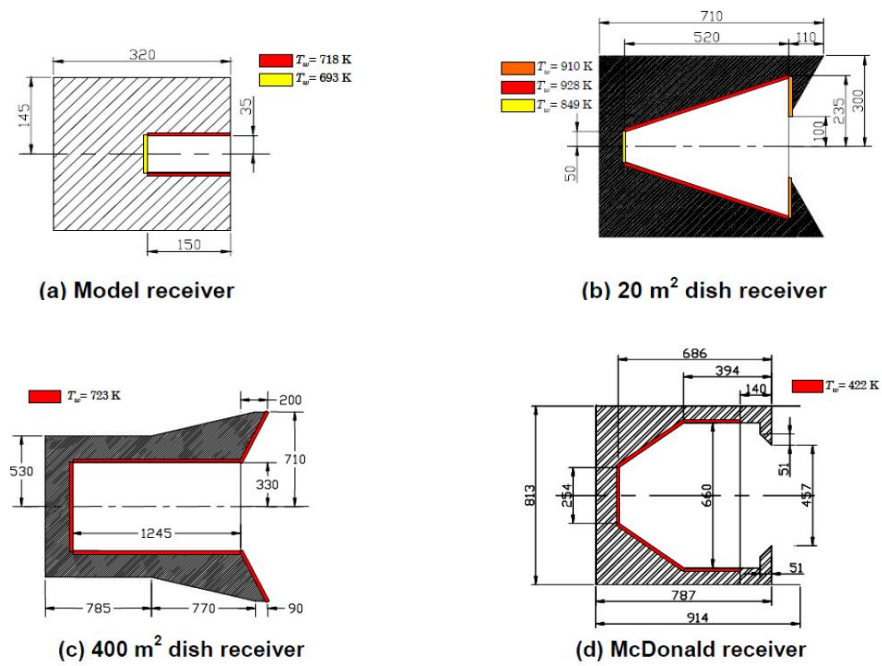

Figure 4.6 - Receiver configurations used by (Paitoonsurikarn, S. and Lovegrove K., 2006)

The authors modify a previous correlation (Paitoonsurikarn S. and Lovegroove K., 2003) by adjusting the characteristic length, according to the original dimensions of the receiver, the aperture and the angle to fit the experimental data.

$$L_s = \left| \sum_{i=1}^{3} a_i \cdot \cos\left(\phi + \psi_i\right)^{b_i} L_i \right| \tag{4.24}$$

The characteristic length is then used to calculate the characteristic parameters of the cavity. Properties are evaluated at film temperature

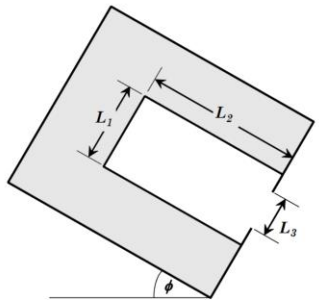

Figure 4.7 – Denotation of geometrical parameters used in the definition of the ensemble cavity length scale L_s, (Paitoonsurikarn, S. and Lovegrove K., 2006)

i	$a_i(-)$	$b_i(-)$	$\psi_i(rad)$
1	4.08	5.41	-0.11
2	-1.17	7.17	-0.30
3	0.07	1.99	-0.08

Table 4.c – Coefficients for (Paitoonsurikarn S. and Lovegroove K., 2003) – natural convection correlations

$$Nu_L = 0.0196 \cdot Ra_L^{0.41} \cdot \Pr^{0.13}$$
$$Nu_L = \frac{hL_s}{k} \;\; ; \;\; Ra_L = \frac{g\beta(T_w - T_\infty)L_s^3}{\nu\alpha} \tag{4.25}$$

Although the correlation is designed for much smaller solar cavity receivers and for a different application, it provides results that are in the range of the (Clausing, 1983), (Clausing, 1987) and (Siebers, D. and Kraabel, J., 1984) model for our cavity receiver. It is one of the most recent correlations for convective loss of cavity receivers and, as there are no limitations provided in the paper that would prohibit a use for larger receivers, this model can be considered to give useful approximation for the convection loss in a cavity receiver of a solar tower.

4.2.5 Leibfried and Ortjohan (1995)

The work of (Leibfried, U. and Orthjohan, J., 1995) aims to develop a correlation for upward and downward facing cavity receivers, for varying tilt angles. Experimental studies were done for the small-scale receiver types shown in the figure below. The temperatures were varied between 573K and 873K

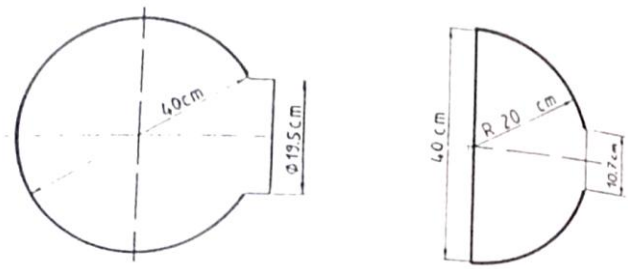

Figure 4.8 - Examined cavity geometries - out of (Leibfried, U. and Orthjohan, J., 1995)

Smoke is introduced in the cavity to visualize the flow pattern. The radiative and conductive losses are measured in a downward facing position. At that position, convective losses are assumed to be negligibly small. The radiative losses are calculated taking into account that the surfaces are not black. Details on how the calculations were performed are not given. The conductive losses are then calculated by subtraction of the calculated radiation losses from the measured heat loss in downward facing position. The total expected error using this method is approximated to be 11% for a heat loss of 900 W.

From these experiments, the authors theorize that the flow inside the cavity can be divided into 5 major regimes, illustrated in the figures below.

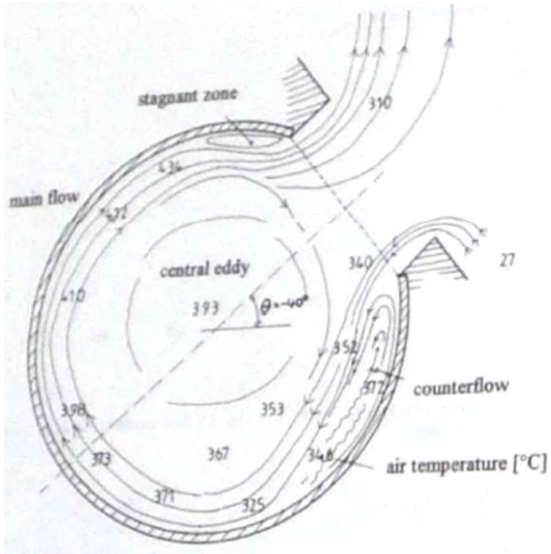

Figure 4.9 - Streamlines in a spherical receiver out of (Leibfried, U. and Orthjohan, J., 1995)

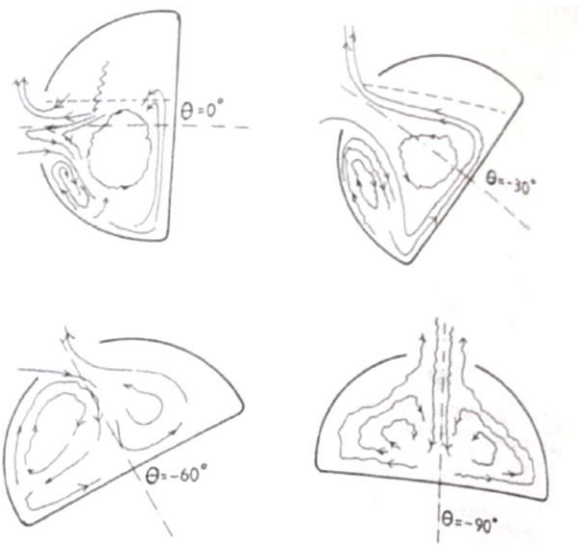

Figure 4.10 - Flow configuration in a hemispherical cavity out of (Leibfried, U. and Orthjohan, J., 1995)

- Cold and hot air, entering and leaving the cavity, respectively
- Rising main air-flow, heating up along the hot wall
- A counter flow retarding entering cold air
- A quasi-isotherm bulk air/ central eddy
- A stagnant zone at the top of the cavity, with stable stratification of hot air

The authors recognize that heat transfer mainly occurs in the boundary layer. Although only buoyancy driven flow is considered, in some regions of the cavity a forced convection like heat transfer is observed. The central eddy, that is caused by buoyancy driven flow, impels an air stream along the inside walls.

In the figure on the right hand side, the observation is illustrated that, for a cavity with a small aperture, the maximum convective heat loss does not occur when it is facing directly upwards. Counter-rotating eddies inside the cavity reduce the exiting steam of hot air. Instead maximum convection loss is observed for tilt angles in the neighborhood of a tilt angle of 45deg upward facing.

The correlation that was deduced from these studies is based on Siebers& Kraabel correlation from 1984 with some modifications to include tilt angles and the understanding of the flow inside the cavity. The characteristic length is the average internal diameter of the cavity; properties are evaluated at ambient temperature.

$$Nu = 0.106 \cdot Gr^{1/3} \left(\frac{T_w}{T_\infty} \right)^{0.18} \cdot \left(4.256 \frac{A_{aperture}}{A_{cavity}} \right)^{s} \cdot h\left(\theta, \theta_{\max}, \theta_{stag} \right) \tag{4.26}$$

The exponent s is given as: $$s = 0.56 - 1.01 \left(\frac{A_{aperture}}{A_{cavity}} \right)^{1/2} \tag{4.27}$$

The function $h\left(\theta, \theta_{\max}, \theta_{stag} \right)$ accounts for the angular dependence of the natural convection losses. The angle at which the heat loss maximum occurs is given with:

$$\theta_{\max} = -23\,\text{deg} - 260\,\text{deg} \cdot \frac{A_{aperture}}{A_{cavity}} \quad \text{for} \quad \frac{A_{aperture}}{A_{cavity}} \leq 0.2 \tag{4.28}$$

For geometries with $\frac{A_{aperture}}{A_{cavity}} > 0.25$ the underlying theory of flow inside the cavity is not valid any more. The aperture is too large in respect to the cavity, the angle of maximum heat loss is then $-90\,\text{deg}$, straight upward facing. The given correlations are not valid for this case.

θ_{stag} is the angle up to which the heated part of the cavity is situated in the stagnant zone. In general it is set to $\theta_{stag} = 90\,\text{deg}$. The effective $\theta_{stag,eff}$ is defined by the authors to include the effect the not heated surfaces inside the cavity have on the heat loss mechanism:

$$\theta_{stag,eff} = \theta_{stag} + \left(90\,\text{deg} - \theta_{stag}\right)\frac{\theta_{stag} - \theta}{\theta_{stag}} \tag{4.29}$$

The reference angle is then defined as: $\bar{\theta} = \dfrac{\theta - \theta_{stag,eff}}{\theta_{\max} - \theta_{stag,eff}}$ (4.30)

With this definition of function h, the following statement is true: $h\left(\theta, \theta_{\max}, \theta_{stag}\right) = h\left(\bar{\theta}\right)$

This function is then given as:

$$h\left(\bar{\theta}\right) = \frac{1}{h_0}\left[1 - \cos\left(\bar{\theta}^{0.85} \cdot \pi\right)\right]$$

$$\text{with: } \mathrm{h}_0 = 1 - \cos\left[\bar{\theta}\left(\theta = 0\right)^{0.85} \cdot \pi\right] \tag{4.31}$$

In case $\theta < \theta_{\max}$ the following equations are give to determine the function h.

$$\bar{\theta} = \frac{\theta + 90\,\text{deg}}{\theta_{\max} + 90\,\text{deg}} \tag{4.32}$$

$$h\left(\bar{\theta}\right) = \frac{1}{h_0}\left(2 - 0.01\left(\theta_{\max} + 90\,\text{deg}\right)\left[1 + \cos\left(\bar{\theta}^{0.9} \cdot \pi\right)\right]\right) \tag{4.33}$$

4.2.6 Natural Convection at Independent Flat Plates

The correlations for natural convection at flat plates are taken out of (Hewitt, 2008). Three different correlations were considered to account for the different orientations of the cavity surfaces. The active panels were approximated as one vertical wall at the average cavity surface temperature. The same correlation for vertical flat plates was used for the panels and the lip of the cavity. Property data for the correlations is determined at film temperature. Because of the size and high temperature of the surfaces, high Rayleigh numbers and turbulent flow is expected. Most of the available natural convection correlations are not valid in the observed range of Rayleigh numbers. Correlations were chosen with validity ranges close to the actual conditions.

Surface Segment	Rayleigh Number for a Range of Operating Conditions
Floor & Ceiling	$5 \cdot 10^{10}$ - $2 \cdot 10^{11}$
Panels	10^{13}
Lip	10^{9}

Table 4.d - Rayleigh number range of the cavity receiver surfaces over a range of operating conditions

<u>Vertical plate – Panels, Lip - valid Ra>10^{12}</u>

$$Nu_{vertical} = 0.15 \cdot \left[Ra \cdot \psi(\mathrm{Pr}) \right]^{\frac{1}{3}} \tag{4.34}$$

<u>Horizontal plates:</u>

Downward-facing plate – Ceiling:

$$Nu_{downward-facing} = 0.6 \cdot \left[Ra \cdot \psi(\mathrm{Pr}) \right]^{\frac{1}{5}} \tag{4.35}$$

With:

$$\psi(\mathrm{Pr}) = \left[1 + \left(\frac{0.492}{\mathrm{Pr}} \right)^{\frac{9}{15}} \right]^{\frac{-16}{9}} \tag{4.36}$$

Upward-facing plate - Floor:

$$Nu_{upward-facing} = \frac{0.766 \cdot Ra^{1/5}}{\left[1 + \left(\frac{0.322}{\mathrm{Pr}} \right)^{11/20} \right]^{4/11}} \tag{4.37}$$

With these correlations the total convective heat loss of the cavity is calculated as the sum of the convective losses from each surface to the air inside the cavity. The overall convection heat transfer coefficient of the cavity is then determined according to:

$$h_{cavity} = \frac{\dot{Q}_{convection}}{\left(T_{wall} - T_{bulk}\right) \cdot A_{cavity}} \tag{4.38}$$

Properties are evaluated at film temperature.

4.2.7 Forced Convection at Independent Flat Plates

For the approach to determine an upper bound of the natural convection losses of the cavity receiver using a forced convection correlation for flat plates the correlation presented by (Hewitt, 2008) is used. The correlations is given in Heat Exchanger Design Handbook - Part 2 – Section 2.5.2-2. It is based on a correlation by (Petukhov, B. S. and Popov, V. N., 1963)

$$Nu_{turb} = \frac{\left(\xi/8\right) \cdot \mathrm{Re} \cdot \mathrm{Pr}}{1 + 12.7\left(\sqrt{\xi/8}\right)\left(\mathrm{Pr}^{2/3} - 1\right)} \tag{4.39}$$

Using the boundary layer theory presented by (Schlichting, 1958), the friction factor ξ is given as:

$$\frac{\xi}{8} = 0.0376 \cdot \mathrm{Re}_l^{-0.2} \tag{4.40}$$

With Eqn. (4.40); Eqn. (4.39) can be simplified to:

$$\boxed{Nu_{l,turb} = \frac{0.0376 \cdot \mathrm{Re}_l^{0.8} \cdot \mathrm{Pr}}{1 + 2.443 \cdot \mathrm{Re}_l^{-0.1}\left(\mathrm{Pr}^{2/3} - 1\right)}} \tag{4.41}$$

The correlation is valid for $5 \cdot 10^5 < \mathrm{Re}_l < 10^7$ and $0.5 < \mathrm{Pr} < 2000$. The Reynolds number is determined according to:

$$\mathrm{Re}_l = \frac{u_{conv} \cdot L_{char}}{\nu_{bulk}} \quad \text{with} \quad u_{conv} = \sqrt{g \cdot \beta_{bulk} \cdot \left(T_{wall} - T_{amb}\right) \cdot L_{cavity}} \tag{4.42}$$

The correlation is used the determine the total heat transfer coefficient using the same method used for the natural convection flay plate correlations described in the previous section. The average wall temperature is an area averaged temperature of the cavity surfaces, with $(4N+4)$ being the total number of surface segments of the cavity:

$$T_{wall} = \frac{\sum_{i=1}^{4N+4} T_{s,i} \cdot A_i}{\sum_{i=1}^{4N+4} A_i} \tag{4.43}$$

4.3 Modeling of Forced Convection

As stated before in Section 4.1, forced convection has a significant influence on the convective heat transfer regime of the receiver. Numerical simulations to assess the forced convection heat losses of the cavity receiver are not practicable for the use in our analytical receiver model. There are also no reliable correlations available in the open literature describing forced convection for cavity receivers, comparable to the type modeled in this work. The only correlation that is applicable and also used for other cavity receiver models[3] is the very simplified model by (Siebers, D. and Kraabel, J., 1984).

To approximate the influence of wind on the convective losses they use a forced convection correlation for a vertical flat plate (Kays, W.M. and Crawford, M.E., 1980). The assumption is supported by the experimental data shown in Figure 4.5.

The used correlation is given in Eqn. (4.44).

$$Nu_{forced} = 0.287 \cdot \mathrm{Re}_w^{0.8} \cdot \mathrm{Pr}^{1/3} \tag{4.44}$$

Properties are evaluated at the film temperature defined as the average surface temperature of the cavity and the ambient temperature. The characteristic length is the width of the aperture.

[3] (Smith, D.C. and Chavez, J.M. , 1987), (Loosen, A. et al., 2011)

The resulting heat transfer coefficient for mixed convection is then:

$$h_{conv,mix} = h_{nc} + h_{forced} \tag{4.45}$$

According to the authors, this correlation under predicts the limited data available from the cavity receiver of the International Energy Agency Small Solar power Systems Project (Almeria, Spain). The authors see the need to develop more advanced, accurate forced convection models for cavities due to the fact that wind effects are suspected to be the largest uncertainties in the correlation.

The correlation is also used to predict the convective heat loss of 4.5 MW test receiver at SANDIA National Laboratory Central Receiver Test Facility in Albuquerque, New Mexico, in (Smith, D.C. and Chavez, J.M. , 1987).

For "flux-off" tests and wind from the front of the receiver, the predicted values are 25-30% higher than measured values. For cases when wind is coming from behind the predicted values are about 60% higher than measured convection losses. In most cases the correlation tends to over-predict the convection loss, for higher wind velocities, the prediction is in the range of the measured value scatter. These results have to be considered with the knowledge that the measurement of the convection losses itself is expected to have an uncertainty of around 50%.

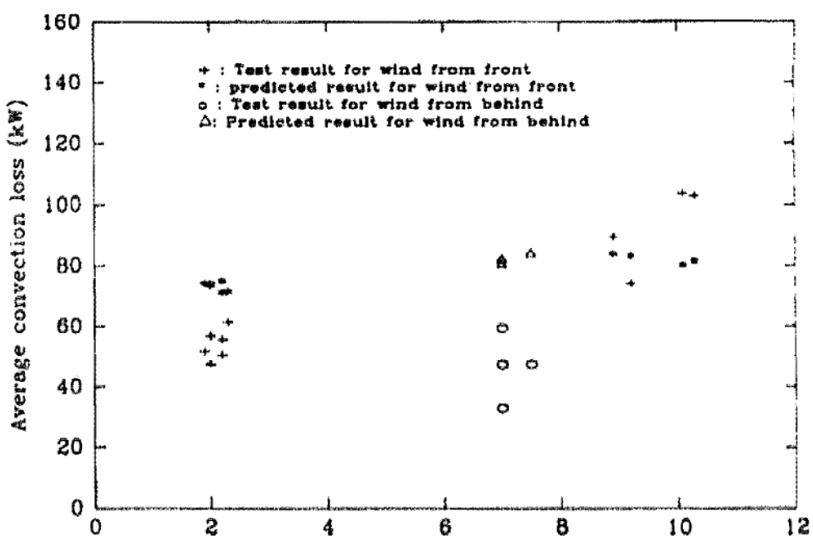

Figure 4.11 - Estimated cavity convective losses for flux-off tests, (Smith, D.C. and Chavez, J.M. , 1987), p.304ff

This correlation provides an approach to approximate wind effects on the overall convection loss of the cavity receiver. One major benefit of the cavity geometry, the shading of the hot internal absorber surface from wind however is not considered by this correlation because it is not taking wind direction into account.. Onside wind on the cavity aperture will have a bigger influence on the convective heat loss than wind that come from the backside of the cavity. Figure 4.12 and Figure 4.13 show the time- wind direction distribution for the TMY- data of Blythe California

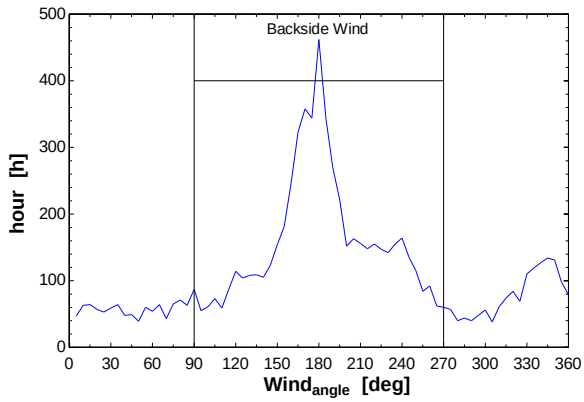

Figure 4.12 - Wind direction from TMY-data Blythe, CA

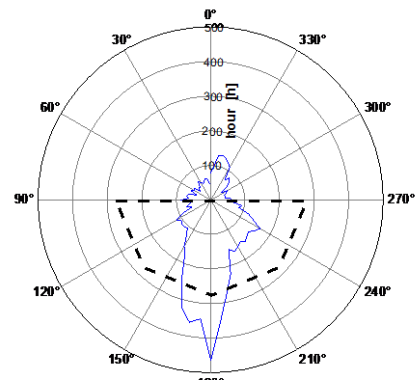

Figure 4.13 - Wind rose from TMY-data Blythe, CA with cavity orientation

To maximize the incident solar radiation on the heliostat field of the solar tower, the cavity is usually facing north. The TMY-data of Blythe shows that most of the time, the wind come from the backside of the cavity, where the shielding effect reduces the influence of wind on the convective heat losses. It can be seen that the wind direction varies significantly over the period of one year influencing forced convection effects in the cavity receiver.

As mentioned before there are no studies available to reliably predict the influence of wind direction in forced convection of a cavity receiver on a solar tower. From a basic understanding one would expect that the forced convection losses will have a maximum if the wind blows straight into the opening at angle 0°. It can be assumed that it will have a minimum when it comes from the backside (180°) and will gradually increase the more wind is directly entering the cavity. These effects could be included in the (Siebers, D. and Kraabel, J., 1984) model using scaling factor $f_{wind-direction,\alpha}$ dependent a wind direction α. A possible distribution could be given by:

$$f_{wind-direction,\alpha} = \frac{2+\cos(\alpha)}{3} \tag{4.46}$$

The resulting scaling factor is given in a polar plot in Figure 4.14.

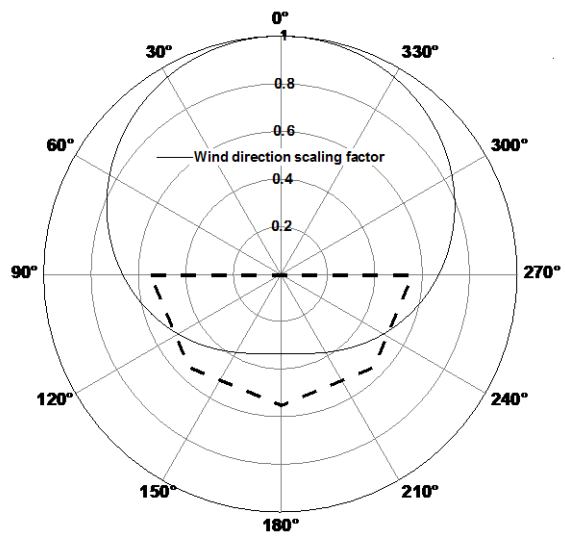

Figure 4.14 – Exemplary scaling factor to account for wind direction dependence of forced convection

The cavity receiver model is implemented in a way that simulation can be run with or without forced convection and the forced convection scaling factor. The code could be easily modified to enable the user to provide a scaling factor distribution. The assumptions made to approximate the influence of forced convection loss on the cavity performance are vague and without any physical validation.

A numerical study done by (Fang, J.B. et al., 2011) illustrates that the actual forced convection processes in the cavity receiver are far more complex and might lead to unexpected directional dependence of forced convection losses.

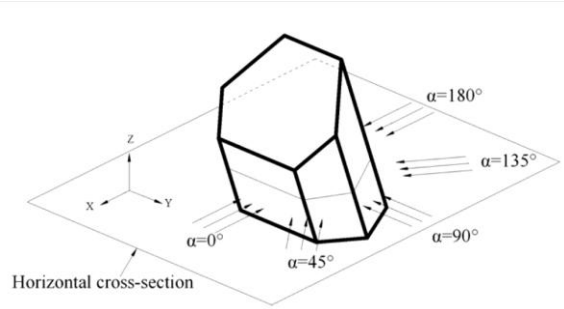

Figure 4.15 – Cavity receiver sketch and wind direction used in numerical study by (Fang, J.B. et al., 2011)

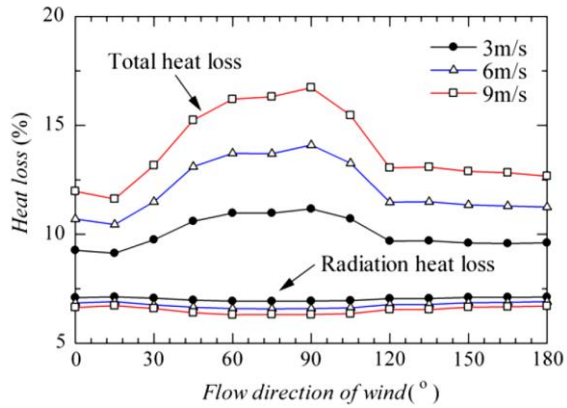

Figure 4.16 – Heat loss of the receiver normalized by incident solar radiation. (Fang, J.B. et al., 2011)

Of particular interest is Figure 4.16 because it suggests that the heat loss is greatest not for onside wind of 0° but rather for side wind from $30^o - 120^o$. Obviously forced convection model implemented in our cavity receiver model can only be a first approximation; further research is necessary to provide a more reliable model.

4.4 Validity of the Correlations

Each of the presented correlations was developed for a certain application and a range of conditions. Table 4.e summarizes the validity range for each correlation presented in Section 0 and set this range in comparison to the operational conditions of the receiver.

Convection model	Limiting Validity Range	Receiver Condition	Correlation validity	Model type
Clausing (1983)	$1 < T_W / T_\infty < 2.6$	$1.8 < T_W / T_\infty < 3.4$	**Out of range for some operational conditions**	Natural convection - cavity model
Clausing (1987)	$Ra < 3 \cdot 10^{10}$	$Ra > 2.8 \cdot 10^{13}$	**Out of range**	Natural convection - cavity model
Siebers and Kraabel (1984) – natural convection	$10^5 < Ra < 10^{12}$	$Ra > 2.8 \cdot 10^{13}$	**Out of range**	Natural convection - cavity model
Siebers and Kraabel (1984) – forced convection	No limits given	-	**Unclear**	Forced convection – vertical plate
Paitoonsurikarn & Lovegrove (2006)	No limits given	-	**Unclear**	Natural convection – dish receiver
Leibfried and Ortjohan	No limits given	-	**Unclear**	Natural convection – dish receiver
Natural Convection at Independent Flat Plates	$Ra > 10^{12}$	$2.8 \cdot 10^{13} < Ra < 7.8 \cdot 10^{13}$	**Within range**	Natural convection - Flat Plate
Forced Convection at Independent Flat Plates	$5 \cdot 10^5 < \mathrm{Re}_l < 10^7$	$1.5 \cdot 10^7 < \mathrm{Re} < 2.8 \cdot 10^7$	**Out of range for some operational conditions**	Forced convection - Flat Plate

Table 4.e - Validity Range of Convection Correlations

The table shows, that none of the cavity correlations are valid within the full range of the receiver conditions. Temperature ratio between wall and ambient, Grashof and Rayleigh number exceed the range of validity of the correlations for a significant portion of operational conditions of the

receiver. The applicability of these correlations for this receiver is questionable. The fact that some of the correlations do not provide a range of validity does not mean these correlations are applicable to the receiver geometry. Part of the motivation to approximate the cavity as a composition of flat plates for the convection models described in Section 4.2.6 and 4.2.7 was the intention to use correlations that cover the range of operational conditions of the receiver. This was accomplished for the natural convection correlations in Section 4.2.6, there was no correlation for forced convection along a flat plate for Reynolds numbers larger than 10^7.

4.5 Measurement of convection loss

The fact that none of the available natural convection correlations are valid for our cavity receiver creates the need to verify the convection loss that is predicted by these correlations for our application. Because there are no experimental data available that could be applied to our model the general question arises on how convective losses of a solar central cavity receiver could be measured.

There are basically two ways to approach the experimental study of convection losses of solar central cavity receivers: **Large-scale analysis**, performed on a near full scale cavity receivers and **Small-scale analysis** performed on laboratory sized experiments. Both methods will be discussed in the following sections.

4.5.1 Review of Existing Small-Scale Experimental Set Ups

It is perhaps useful to review the existing small-scale convective loss measurement methods that have appeared in recent literature. (Prakash, M. et al., 2008) describes the following experimental set up:

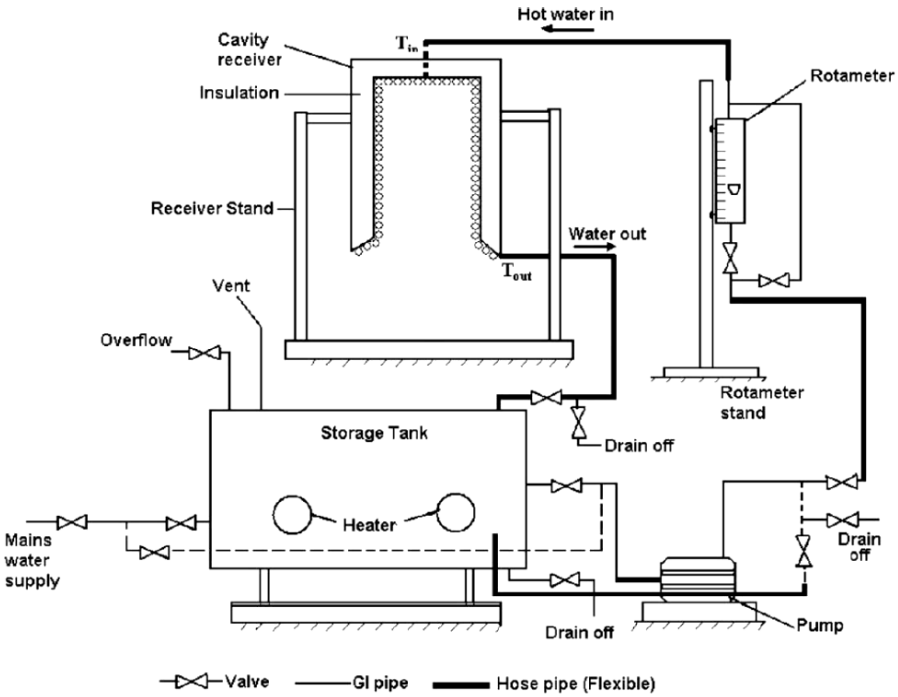

Figure 4.17 - Experimental set up, (Prakash, M. et al., 2008)

The cavity receiver is built using coiled helical copper tubing with a diameter of 0.009 m, coated with polyurethane to withstand temperatures of about 520 K. A layer of mineral wool (thickness 0.075 m) and aluminum foil on the outside insulates the receiver thermally.

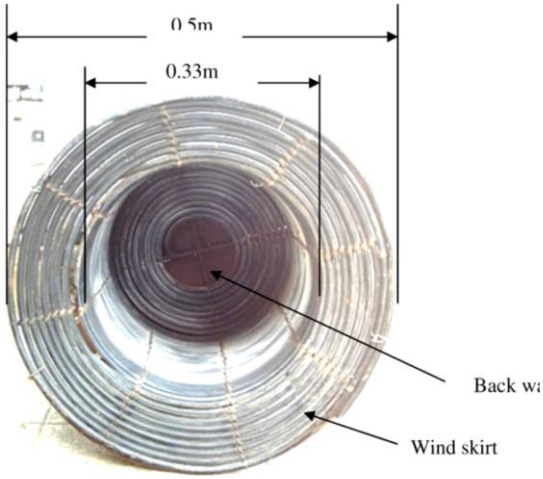

Figure 4.18 – Front view cavity receiver (Prakash, M. et al., 2008)

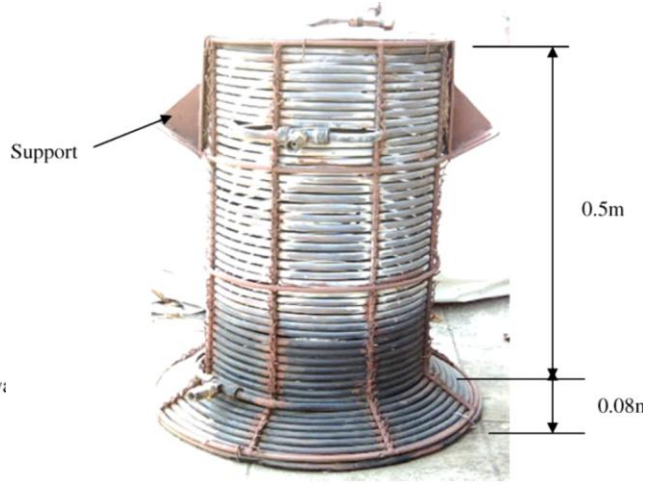

Figure 4.19 - Side view cavity receiver (Prakash, M. et al., 2008)

The receiver is mounted on a stand in a way that it can be inclined to various angles in steps of 15°. The receiver surfaces are heated with a steady waterflow of 0.02 kg/s, inlet temperatures can be varied between 320 K-350 K. The heating water is supplied by a 125 liter storage tank with water being heated by a 3 kW resistance element. The fluid temperature flowing through the cavity is measured at four evenly distributed locations in the receiver.

One possible approach to determine the different heat loss mechanisms is to measure the heat loss of the cavity receiver at a downward facing position where no forced or natural convection losses are expected ((Leibfried, U. and Orthjohan, J., 1995), (Stine, W.B. and McDonald, C.G., 1989)). In this way, heat losses only occur via radiation and conduction. Blocking the aperture for radiation should approximate the conductive losses as radiation losses are significantly diminished. In many studies the radiation losses are calculated instead of a direct measurement.

Forced convection around the cavity reciever was analyzed using a blower with flow straighteners (honeycomb mesh). The blower was located 0.2 m from the receiver stand in order to study convective losses attributable to both head-on and side-on wind. Maximum wind speeds that could be achieved with this method are 3 m/s.

This study is an example for a comparably simple small-scale experiment set up. The disadvantage of this simplicity is the lack of similarity to large-scale solar cavity receiver. This study was done to analyze receivers typical in solar dish applications, which are typically much smaller than the cavity receiver of interest to this research. To obtain similarity with a cavity receiver of a solar tower, the entire apparatus would need to be in a vessel where ambient pressure and temperature are controllable. Also the surface temperatures obtainable in this experiment are too low to represent a solar tower receiver. Another small-scale experimental study is presented by (Leibfried, U. and Orthjohan, J., 1995). Here a spherical- and hemispherical cavity with an inner diameter of 0.4 m is studied.

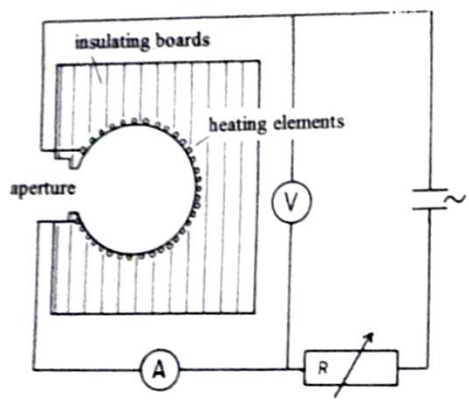

Figure 4.20 - Experimental set up (Leibfried, U. and Orthjohan, J., 1995)

The cavity is heated by six tubular heating elements, each of 2.5 m length, which are wrapped around the cavity outside. The wall temperature can be varied between 573 K-873 K, by varying the power input to the heating elements. The cavity is placed in micro porous insulating boards and can be turned to upwards and downward-facing positions. Nine thermocouples are used to measure the mean wall temperature. To visualize the flow, smoke can be introduced in the cavity though a thin tube. To approximate flow- and eddy velocities thin sheets of papers are introduced in the cavity. After burning the paper, the very light ash flows with the streaming, permitting the approximation of velocities.

To determine the loss components, the same method as mentioned before is used. In a downward facing position the convection loss is neglected, at steady state the electrical power is equal to the radiation and conduction loss. To determine the conduction loss, a plug on the opening is used which prevents radiation loss. Alternatively the authors note that radiation loss can be calculated

and subtracted from the electrical power for downward facing position. (Leibfried, U. and Orthjohan, J., 1995) estimate the error of this measuring method to be about 11 percent for a heat loss of 900 W. This uncertainty includes errors in the measurement and errors due to the calculation.

A similar experiment is introduced by (Taumoefolau, T. et al., 2004). An electrically heated cylindrical cavity receiver is used to examine convective heat transfer losses and flow regime of the cavity. The experiment is done at laboratory (ambient conditions); the Rayleigh numbers were between 10^7-10^9, which is much lower than the range of 10^{11}-10^{14} needed for large cavity receivers.

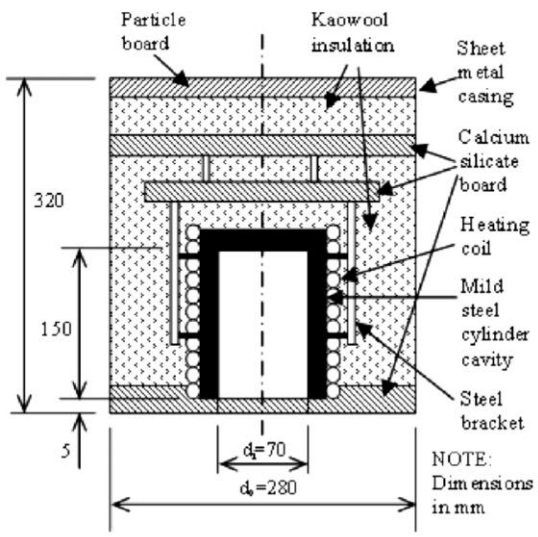

Figure 4.21 – Outline of experimental set up (Taumoefolau, T. et al., 2004)

Conductive heat losses are determined using an insulated plug in the aperture. Internal and external temperatures of the plug were measured to determine the plug conduction loss. Conduction loss through the insulation were also calculated using a thermal resistance network assuming that convection from outside of the insulation is independent of inclination. Also a finite element analysis of the conduction losses yielded agreement within 10% of the analytical method. Differences are explained by the uncertainty in the actual effective conductivity of the insulation material. Radiation losses were calculated using the radiosity method. A synthetic Schlieren method was used to visualize the flow at the exit of the cavity.

Numerical analysis in FLUENT was developed and verified using the experimental results. Comparing the results to the existing natural convection correlations it was found that for a

horizontal orientation, the (Clausing, 1981) model under predicts the losses by about 20% and the (Clausing, 1987) model over predicts the losses by about 20%.

4.5.2 Small-Scale Analysis

The underlying idea of small-scale analysis is to design a reduced-scale experiment that will be representative of the full size cavity receiver with the goal of establishing physical and thermal similarity to the actual cavity receiver. Dimensionless numbers are used to characterize the cavity receiver. As shown in the previous section, significant properties of the solar cavity receiver are its characteristic length (about 25 m), the large temperature ratio between wall- and ambient temperature (ratios as high as 3 are possible), and the turbulent flow regime indicated by high Reynolds-, Grashof- and Rayleigh numbers. The most important conditions of similarity needed to represent a large-scale cavity receiver with a small-scale experiment are still subject of research and not well understood (Falcone, P., K. et al., 1981). It is therefore not clear which dimensionless characteristics a small-scale experiment must meet to guarantee physical and thermal similarity to full- scale cavity receiver. It is not possible to design a small-scale experiment that has all dimensionless characteristics identical to the actual system.

To design small-scale experiments efficiently, the analysis is often restricted to only one aspect of the system. It is usually easier to design an experiment that only represents natural convection than to couple it with incident radiation to consider radiation losses.

To obtain Prandtl-, Grashof-, and Rayleigh number in the range shown in Table 4.a with a small-scale experiment, it was found that ambient temperatures in the range of 100-250 K, cavity-wall temperatures of 230-550K and ambient pressures of 4-20 bar are necessary. Because of the comparably large volume that would be required to minimize “end-effects” associated with the experimental apparatus, it is advisable to choose a fluid that is safe and easy to handle. Of the fluids that were considered, air, nitrogen, argon, R124 and R134a meet the requirements within the given temperature and pressure ranges. Low cavity surface temperatures are desirable to minimize thermal radiation losses.

To analyze natural convection, it is expected that a comparably large control volume around the cavity geometry has to be established to assure unrestricted buoyancy induced flow. To keep the design and operation of a small-scale experiment simple and cost efficient, the total volume of the

enclosure should not exceed 1 m^3. In this respect, fluids that are cheap and easy to handle, with pressures and temperatures in the magnitude of ambient conditions are desirable.

As shown in Table 4.f, these requirements cannot all be met in the same design. Restricting the total size of the apparatus requires a characteristic length of the cavity receiver of about 0.3 m. Using air as the working fluid would require pressures of about 17-28 atm and cryogenic fluid temperatures. Using R124 instead of air makes it possible to work at pressures of around 5 atm and temperatures close to ambient conditions. The apparatus would then have to meet more strict requirements to be able to contain R124, which would increase the cost and complexity of the system, in addition to the fluid costs. Conditions of similarity for a characteristic length of 1 m were also investigated to determine if a much larger experiment would have less demanding requirements. As shown in Table 4.f, the requirements are a little less strict, requiring lower ambient pressures and wall temperatures. The ambient temperatures can only be slightly higher than using a characteristic length of 0.3 m. It seems like the advantage in less extreme physical conditions to achieve similarity are not worth the additional effort a larger experiment brings with it. It is noteable that a larger experiment and the use of R124 would allow experiments near ambient conditions, which might offer a possibility for very simplified experimental apparatus.

The use of other common gases was investigated as well. Besides for various refrigerants, similarity was tried to achieve using ammonia, helium, argon, carbon dioxide, nitrogen as the working fluid. With some of these fluids similarity cannot be achieved under any ambient condition. For ammonia, and carbon dioxide the Prandtl number is generally too high, for helium too low. Similarity was achieved only with two refrigerants, R134a and R124. Table 4.f shows conditions required to achieve similarity with the full-scale receiver in a laboratory-scale receiver using nitrogen and argon.

Fluid	Characteristic length	Ambient temperature	Wall temperature	Pressure	Grashof & Rayleigh	Prandtl
Air	0.3 m	100-186 K	490-660 K	17-28 atm	10^{11}-10^{12}	0.71-0.73
Nitrogen	0.3 m	125-190 K	486-630 K	22-37 atm	10^{11}-10^{12}	0.71-0.73
Argon	0.3 m	115-230 K	310-430 K	17-38 atm	10^{11}-10^{12}	0.69-072
R134a	0.3 m	-	-	-	-	-
R124	0.3 m	270-285 K	440-475 K	4.8-5.2 atm	10^{11}	0.71-0.72
Air	1 m	100-230 K	230-540 K	4-19 atm	10^{11}-10^{13}	0.70-0.73
Nitrogen	1 m	160-220 K	310-545 K	4-11 atm	10^{11}-10^{12}	0.71-0.72
Argon	1 m	100-200 K	200-300 K	10-20 atm	10^{12}-10^{13}	0.69-0.72
R134a	1 m	200-250 K	350-430 K	0.9-1.9 atm	10^{11}	0.72
R124	1 m	210-290 K	350-550K	0.7-1.6 atm	10^{11}-10^{12}	0.69-72

Table 4.f - Conditions required to achieve similarity for a small-scale experimental set up

Clearly, conducting small-scale experiments requires considerable effort and design/operation complexities while producing results of unknown validity. A pressure vessel with a volume of at least 3 m^3 controllable for fluid pressures of up to 38 atm and fluid temperatures as low as 100 K are necessary if air should be used as a fluid. The pressure can be reduced to about 5 atm using R124. With a much larger experiments and R124 a fluid similarity can be achieved near ambient conditions.

Even though these conditions can be achieved for a small-scale analysis of natural convection, the level of experimental complexity increases significantly if the effects of forced convection are also to be investigated. First, a means of generating external flow would be required suggesting the need for a wind tunnel. A significantly larger control volume would be necessary to ensure an undisturbed flow regime around the cavity model and to maintain a controlled temperature of the convective “ambient” fluid flowing past the cavity. These experimental challenges coupled with the uncertainty about the physical and thermal similarity to the actual cavity receiver indicate that using a small-scale experimental method is probably not worthy of pursuit to characterize convective losses of cavity receivers.

4.5.3 Large-Scale Analysis

Large-scale analysis implies that measurements are performed on a full-scale (or near full-scale) cavity receiver. In this way, realistic convective flow/heat loss and energy transfer (short-wave radiation, long-wave radiation, and convection) conditions are assured. Disadvantages of large-scale experiments are the high costs, the complexity of the experimental set up, and the inherent difficulty controlling the environmental conditions. In addition, the direct measurement of convection losses is very difficult. Because of the spatial variations in flux, temperature and flow conditions, a large quantity of measurements is necessary to fully characterize the convection processes occurring inside the cavity. The size of the experiment also complicates any approach to visualize the flow phenomena that drive the convection heat transfer inside the cavity.

One way to determine the convection losses is to use the following energy balance of the receiver:

$$\dot{Q}_{convection-loss} = \dot{Q}_{solar,in} - \dot{Q}_{HTF} - \dot{Q}_{radiation-loss} \tag{4.47}$$

While the energy absorbed by the HTF can be measured quite easily, the determination of incident solar radiation and radiation losses are only possible with somewhat higher uncertainty. Typically, radiation losses are calculated, as there is no easy way to measure these losses in large-scale experiments. The calculated radiation losses rely on properties such as the surface emissivities that may not be accurately known. The terms on the right hand side of Eqn. (4.47) are significantly larger than the convection loss on the left hand side. Calculating the convective loss as a difference of large quantities leads to a greater relative uncertainty than for the other terms.

A way to reduce the uncertainty is to perform the measurements without solar flux. In this case, the first term on the right hand side of Eqn. (4.47) is eliminated and the radiation losses decrease. The cavity then needs to be heated by the HTF. The advantage of a smaller uncertainty in the measurement comes with the disadvantage that the mode of operation of the receiver might not be represented accurately without flux. In previous studies of our model it was shown that reflection inside the cavity leads to high passive surface temperatures. The passive surfaces have a significant influence on the overall convection loss of the cavity receiver. Just heating the active surfaces in a flux off test would not capture this effect.

In SAND81-8014 (Falcone, P., K. et al., 1981) In SAND81-8014 (Falcone P.K, (1981)), R.J. Gallagher reports results for uncertainty of convective loss measurements in large-scale experiments, as shown in Figure 5.1 and Figure 4.23.

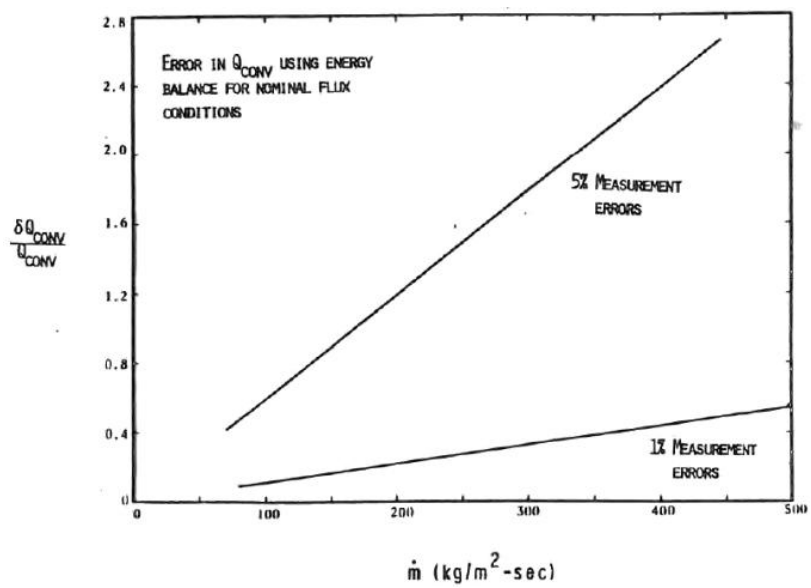

Figure 4.22 – Non-dimensional convective loss measurement uncertainty- <u>flux on</u> test – measurement error as parameter (Falcone, P., K. et al., 1981)

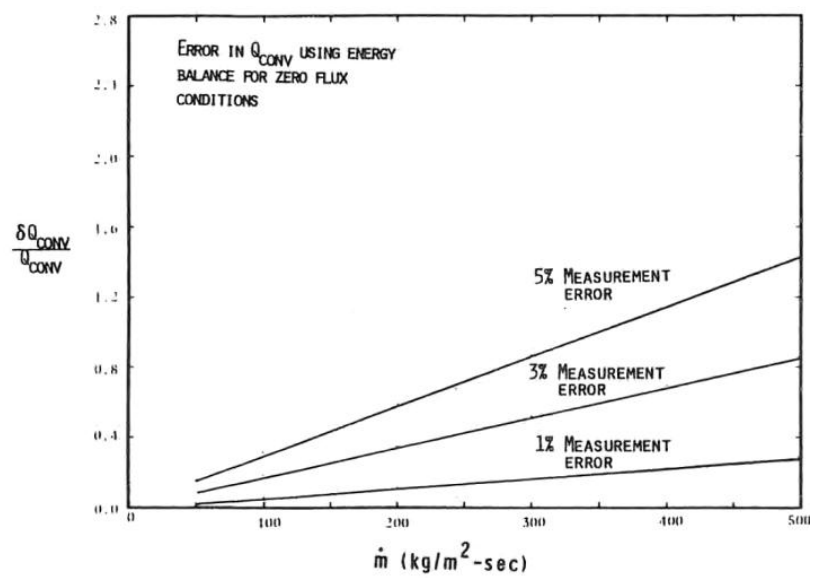

Figure 4.23 – Non-dimensional convective loss measurement uncertainty- <u>flux off</u> test – measurement error as parameter (Falcone, P., K. et al., 1981)

The convective loss was determined using Eqn. (4.47) in Figure 4.22 and Figure 4.23. For an receiver-area-based mass flow rate of 600 kg/m^2-s, the authors report that the uncertainty can be about 300% for *flux on* tests and 120% for *flux off* tests assuming 5% measurement error. The flow rates in our receiver are with 700-2000 kg/m^2-s significantly higher. With this large uncertainty, detailed study of the convective heat loss of a cavity receiver cannot effectively be performed

4.5.4 Measurement of Useful Energy Gain of the HTF

The heat transfer to the HTF depends on the fluid properties, the mass flow rate and the temperature change of the fluid:

$$\dot{Q}_{HTF} = \dot{m}_{HTF} \cdot cp_{HTF} \cdot \left(T_{HTF,out} - T_{HTF,in}\right) \tag{4.48}$$

(Ritchie, J.A., 2010) used K-type thermocouples to measure the temperature of molten salts. The temperature of the HTF in our model varies between 280 K and 580 K. In this temperature range the error of measurement is according to "ANSI Standard Limits of Error" (Weed, 2011) is about 1.4 K.

To determine the mass flow rate of the HTF the flow velocity u_{HTF} has to be measured:

$$\dot{m}_{HTF} = \rho_{HTF} \cdot A_{tube} \cdot u_{HTF} \tag{4.49}$$

(Ritchie, J.A., 2010) uses ultrasonic Doppler flowmeters, which utilize the physical phenomenon that sound waves changes frequency when reflected by moving discontinuities in a flowing liquid (Omega, 2011). The flowmeter measures the difference between the output and input frequencies of the ultrasound waves and translates this difference to the average flow velocity inside the pipe. This method requires a minimum of 100 PPM of suspended solids or bubbles with a size of 100 microns or larger. As this method only returns the average flow velocity, the accuracy depends on the flow velocity profile. Calibrating the flow meter with information about the flow regime such as size, velocity profile, distribution and variation of the sound reflectors, accuracy can be as high as ±1%. As this is usually not possible, a safety factor of 2 is used with a corresponding uncertainty for measuring flow of ±2% using ultrasonic Doppler flowmeters.

An alternative way to measure flow velocity is the use of a Venturi-type flow meter. Here the pressure drop of the flow at throat of the meter is measured. Typical uncertainties in velocity are in the ±1-2% range. A very small uncertainty for the cross-sectional area of the tube is assumed (±0.001%.), because of the high accuracy in the manufacturing process. Using property data for the molten salt from Williams (2006), the propagated relative uncertainty of the useful energy gain of the HTF is about 2 % or 9.6 MW based on the combined uncertainties of the velocity and temperature measurements.

4.5.5 Measurement of the Incoming Solar Flux

The incoming solar radiation cannot easily measured, which is part of the reason that it is calculated in most existing studies (Smith, D.C. and Chavez, J.M. , 1987). A possible measurement method is the use of a heat flux gage. These gages are basically a differential thermocouple measuring the temperature difference between the center and the circumference of a thin circular foil disk, similar to the detectors used in high-accuracy pyranometers. The disk is connected to a heat sink made of copper. The detector foil is made of Constantan; a temperature difference on this thermocouple produces the Seebeck-Voltage that is directly proportional to the absorbed heat flux. These gages detect the total incoming heat flux.

To exclude convection losses the detector foil is concealed with a window. The wavelength band of the radiation that is detected can be chosen with the material of the window. In (Vatell, 2011) a quartz window is proposed for a spectral limit of 0.3-3 μm which could be used to approximately measure thermal and solar radiation separately. Locating the flux gage in the cavity walls would lead to the problem that not only incident solar radiation but also reflected solar radiation and thermal radiation with wavelength smaller 3 μm would be detected. The incident solar flux from the mirror field on the cavity receiver could be estimated with a grid of flux gages at the aperture, facing outward and thereby excluding reflected solar radiation. The thermal radiation heat transfer from the ambient to the cavity is considered to be negligible. The measuring method would provide a useful estimate of the incident solar radiation. Depending on the number of sensors the incident solar radiation for each surface segment might be estimated, an accurate measurement is not possible. Also the measuring apparatus would block part of the aperture, influencing the cavity performance. (Vatell, 2011) claims, that the sensor can achieve accuracies of ±3%, regular calibration suppositional.

As the solar flux is the largest term in the energy balance, Eqn. (4.47), uncertainties of this term result in intolerable high uncertainties of the convection loss. With receiver efficiencies between $90-95\%$ the convective losses can be about 5% of the incident solar radiation. Even small uncertainties in the incoming solar power will lead to high uncertainty of the convective loss. Test methods without solar flux do not have this disadvantage.

4.5.6 Measurement of Radiation Heat Loss

As for the incoming solar radiation, there is no easy method available to accurately measure radiation heat transfer directly. The most common approach is to measure the surface temperatures and estimate the surface properties of the cavity and calculate the radiation loss using a radiation model.

To represent the temperature distribution on the cavity surfaces accurately a large number of measurements are necessary. With at least 2 temperature sensors per surface node, 48 measurements would be necessary for the cavity model applied in this research. (Smith, D.C. and Chavez, J.M. , 1987) report the attempt to use an infrared camera to infer the surface temperatures and the temperature distribution of the cavity receiver. No conclusion concerning the effectiveness of this method is given.

$$\begin{aligned}\dot{Q}_{radiaiton,i} &= \sigma \cdot \varepsilon_{therm,i} \cdot A_i \cdot \sum_{j=1}^{4N+4} \varepsilon_{therm,j} \cdot \hat{F}_{therm,i,j} \cdot \left[\left(1 - f_{0-\lambda_{step},T_i}\right) \cdot T_i^4 - \left(1 - f_{0-\lambda_{step},T_j}\right) \cdot T_j^4 \right] \\ &+ \sigma \cdot \varepsilon_{solar,i} \cdot A_i \cdot \sum_{j=1}^{4N+4} \varepsilon_{solar,j} \cdot \hat{F}_{solar,i,j} \cdot \left[f_{0-\lambda_{step},T_i} \cdot T_i^4 - f_{0-\lambda_{step},T_j} \cdot T_j^4 \right] \\ &+ f_{0-\lambda_{step},T_{sun}} \cdot A_i \cdot \sum_{j=1}^{N} \hat{F}_{solar,i,j} \cdot \left[Flux_{solar,i} \cdot \left(1 - \varepsilon_{solar,i}\right) \cdot \varepsilon_{solar,j} - Flux_{solar,j} \cdot \left(1 - \varepsilon_{solar,j}\right) \cdot \varepsilon_{solar,i} \right] \\ &+ \left(1 - f_{0-\lambda_{step},T_{sun}}\right) \cdot A_i \cdot \sum_{j=1}^{N} \hat{F}_{therm,i,j} \cdot \left[Flux_{solar,i} \cdot \left(1 - \varepsilon_{therm,i}\right) \cdot \varepsilon_{therm,j} - Flux_{solar,j} \cdot \left(1 - \varepsilon_{therm,j}\right) \cdot \varepsilon_{therm,i} \right]\end{aligned}$$

(3.48)

The radiation loss is calculated according to Eqn. (3.48), with *i* representing the aperture surface. Using thermocouples to measure the surface temperatures, the uncertainty can be specified according to “ANSI Standard Limits of Error” (Weed, 2011) 2.4K. According to (Falcone, P., K. et al., 1981), the uncertainty of receiver surface area can be as high as 4%. This relative uncertainty is understandable as the receiver panels are approximated as plane walls for the

modeling process; in fact they are composed of tube banks that convey the HTF. Possible errors in the determination of the view factors are considered with 1%. The uncertainty in the determination of the surface emissivities and reflectivities is set to 0.025. The error in determining the solar flux is estimated to be ±3%, as mentioned in the previous section.

With these uncertainties in the various measurements, the variation of the radiation loss due to measurement errors is about 37% (Table 4.h). This overall uncertainty is almost entirely governed by the uncertainty in the solar emissivities. The change in solar emissivity of the active surfaces by ±0.025 is responsible for 98% of the overall uncertainty. The next largest influences with 0.5% respectively are the uncertainties of the surface area of the aperture and the average solar flux. All other inputs have negligible influence on the uncertainty of the radiation heat transfer calculation.

4.5.7 Flux-On Testing

The loss components are determined on the basis of the energy balance in Eqn.(4.47). To establish the convection losses, all other terms in the energy balance are determined as described above. To calculate the uncertainty of the heat loss determination, the uncertainties in the determination of the remaining terms in the energy balance have to be calculated. The uncertainties are, for the most part caused by measurement errors. The propagation of these measurement errors to the convection heat loss determination is calculated in EES (Klein, S.A., 2011) as described by (Taylor and Kuyatt, 1994). It is assumed that the individual measurements are uncorrelated and random. With $y = f(x_i)$ for i=1..N the uncertainty U can be calculated according to:

$$U_y = \sqrt{\sum_{i=1}^{N} \left(\frac{\partial Y}{\partial X_i} \right)^2 \cdot U_{X_i}^2} \tag{4.50}$$

The resulting uncertainty with that the convective losses can be measured is about ± 70%. Being able to determine convective losses with accuracy in this range does not allow a deeper understanding of the convective heat loss mechanism compared to use of the correlations, as we have been doing. As a result, this measurement approach of convective losses is not entirely helpful. Table 4.g summarizes the assumed uncertainties of the inputs for the overall uncertainty calculation.

Measured physical value	**Measuring method**	**Uncertainty**	**Reference**
HTF - Temperature	K-type thermocouple (280-580K)	±1.4 K	"ANSI Standard Limits of Error" (Weed)
HTF – flow velocity	Ultrasonic Doppler flowmeter	Min: ±1%	*Omega – "ULTRASONIC DOPPLER FLOWMETERS Flow Reference Section"*
	Venturi type	±2%	
HTF - properties	Property data – Williams (2006) - EES	-	Williams (2006)
HTF- tube – cross sectional area	-	±0.001%	assumed
Solar flux	Heat flux gage/ transducer (differential thermocouple)	±3%	Vatell (2011) Wavelength bands 0.3-3 μm / 3-5 μm / 0.6-17 μm
Receiver surface temperature	K-type thermocouple (270-850K)	±2.4K	"ANSI Standard Limits of Error" (Weed)
Receiver surface area	-	±4%	SAND81-8014
View factors	-	±1%	assumed
Surface emissivities	-	±0.025	assumed

Table 4.g - Assumed uncertainties of the measured inputs to evaluate the heat loss components

Table 4.h summarizes the uncertainty with that the energy balance components are determined. The uncertainty is given as a variation of around the true value as a percentage. Also the driving uncertainty influences of the measurements for each component are given.

Energy balance component	**Uncertainty** Variation in percent of particular loss component	**Driving uncertainty influence** Percentage of component uncertainty
Convection	±70%	$Flux_{avg}$≈58% ; u_{HTF}≈22%; ε_{solar}≈12%; Cavity Area ≈6%; $T_{HTF,in/out}$=2% ;
Useful energy gain HTF	±2%	u_{HTF}≈89 $T_{HTF,in}$=5.7% ; $T_{HTF,out}$=5.3%
Radiation loss	±37%	ε_{solar}≈98%
Incident Solar	±3%	$Flux_{avg}$≈92%; Cavity Area ≈8%;

Table 4.h - Flux on - Uncertainty of heat loss component determination

4.5.8 Barron Method and Baker Modification

A way to estimate the thermal losses of a solar central receiver without having to determine the incident solar radiation is the *Barron Method* (Smith, D.C. and Chavez, J.M. , 1987). This method considers two cases, one with the full heliostat field focused on the receiver and one with only 50% of the heliostats reflecting radiation to the receiver. The assumption behind the method is that, despite the different incident solar power, the cavity receiver can be operated at the same average surface temperature by adjusting the HTF mass flow rate. Note that the “energy loss” due to reflection is not considered in this method. For these cases, the temperature-dependent heat loss is assumed to be constant. This assumption oversimplifies the heat transfer situation because it does not consider the influence of the passive surfaces. With varying solar flux the passive surface temperatures change and influence the thermal losses significantly. In contrast to the active surfaces, the temperature of the passive surfaces cannot be controlled with the mass flow rate of the HTF. Also, the thermal losses are not only dependent on the average temperature

level but also by the temperature distribution; this effect is not considered in the Barron Method. For the two different solar flux levels the energy gain of the HTF is measured as $\dot{Q}_{HTF,high}$ and $\dot{Q}_{HTF,low}$. According to Barron, the total heat loss can be calculated with:

$$\dot{Q}_{loss} = \dot{Q}_{HTF,high}{}^{-2} \cdot \dot{Q}_{HTF,low} \tag{4.51}$$

In practice, surface temperatures may exhibit significant variations when the solar flux changes. To account for the resulting variation of the heat loss with the incident flux, Baker modified the Barron Method. The test cycle of the Baker modification contains three measurements. The first and third use complementary numbers of heliostats, the second uses the complete field. The thermal receiver heat loss is calculated according to:

$$\dot{Q}_{loss} = \frac{\dot{Q}_{HTF,2} \cdot \left(\dot{Q}_{HTF,1} \cdot IR_1 + \dot{Q}_{HTF,3} \cdot IR_3 \right)}{IR_1 \cdot LR_1 + IR_3 \cdot LR_3 - 1} \tag{4.52}$$

The indices represent the measurement number. IR_i is the ratio of solar energy incident at measurement i (one or three) to the solar energy at measurement two. Analogously, LR_i is defined for the thermal loss. The loss ratios are taken from a calculation model. The idea behind this method is that the ratio of the heat losses for different flux levels may be known with better accuracy than the absolute values.

This method does not require the measurement of the incident solar power; however, it is not expected to provide detailed information about the convective losses. It might be a convenient way to approximate the total thermal losses of central receiver without the need to measure the incident solar power but the assumptions made in this method oversimplify the heat transfer process inside the cavity resulting in significant uncertainty. With our model, it was observed that the temperature distribution inside the cavity (and not only the average wall temperature) has a major influence on the energy loss from the cavity. Measuring the surface temperatures and surface properties of the cavity makes it possible to calculate the long-wave radiation loss. In this way, the convection loss can be determined from the total heat loss. The use of loss ratios to determine the heat loss requires the implementation of a particular convection heat loss model. The question which convection model is appropriate is the purpose of this measuring method. Consequently this approach is not particularly helpful.

4.5.9 Flux Off Testing

In the previous sections it was found that the incoming solar flux is the dominant source of uncertainty when measuring heat loss of a solar central receiver. Because the heat loss is estimated to be 5-15% of the incident solar radiation, even small uncertainties in the determination of this value cause significant uncertainty in the determination the heat loss.

With this finding in mind, the uncertainty in measuring the heat loss could be greatly reduced for measurements without incident solar radiation (at night), using the so called "flux-off tests". To reproduce a similar thermodynamic situation as at daytime with solar flux, the cavity surfaces have to be heated to the appropriate temperatures. The thermal radiation loss can be determined with good accuracy, using a radiation model with the given surface temperatures if the surface properties and cavity geometry are known. The heat input to each cavity section must be controlled to maintain the representative surface temperatures. With an energy balance of the receiver, the convection losses can be determined.

$$\dot{Q}_{convection-loss} = \dot{Q}_{Heating} - \dot{Q}_{radiation-loss} \tag{4.53}$$

The assumed uncertainties of the inputs are given in Table 4.h. In the testing process, the heat input will be measured. To determine the uncertainty of this method, the heat input has to be estimated in this study using a convection model. For this purpose the updated (Clausing, 1987) model is used. In Table 4.i, the relative uncertainty of each component and the particular major influence is given.

Energy balance component	**Uncertainty** Variation in percent of particular loss component	**Driving uncertainty influence** Percentage of component uncertainty
Convection	±13%	Heating≈91% ; ε_{therm}≈7% ; $\varepsilon_{therm,passive}$≈2%
Heat input	±10% - assumed	-
Radiation loss	±16%	ε_{therm}≈76% ; $\varepsilon_{therm,passive}$≈18%; $A_{aperture}$≈6%

Table 4.i - Flux off uncertainty of heat loss component determination

Using the flux-off method, the relative uncertainty of the determined convection loss is about 13%. The relevant influences on the accuracy of this value are the uncertainty of the measured heat input and less importantly the thermal emissivity that dominate the thermal radiation loss.

The radiation is calculated assuming an emissivity distribution inside the cavity with ε_{solar}=0.95; ε_{therm}=0.1; $\varepsilon_{solar\text{-}passive}$=0.1; $\varepsilon_{therm\text{-}passive}$=0.1, that results in minimum heat losses. For this cavity configuration at normal flux-on operation, the receiver surface temperatures are between 540-850 K. To represent these operational conditions in a flux-off test, the surfaces have to be heated to reach the same temperatures. The required heating power is in the range of 20 MW. For cavity surfaces with higher emissivities, the required heating power can be up to 60 MW. That is an unrealistic requirement for electrical heaters.

A more realistic means of heating the active surfaces is to use the stored hot molten salt to provide basic heating to all surfaces in place of electrical resistance heaters. Since the outlet temperature of the HTF is about 847 K, the pumped HTF should be able to provide most of the heating power required for the test. The problem with this method is that the surface temperatures cannot be controlled independently. Consequently it will be very difficult to precisely reproduce the surface temperature distribution that is observed under flux on conditions.

4.5.10 Daytime Flux Off Transient Testing

In the previous section (4.5.9), it was shown that the convection losses of a cavity receiver can be measured with acceptable accuracy when there is no incoming solar flux. To obtain representative surface temperatures of the cavity receiver for flux-off testing, a heating power of up to 20MW is necessary. Because of the large heating power, electrical heaters are not feasible. Using the HTF from the hot reservoir as a heat source the representative surface temperature distribution inside the cavity may not be reproducible; therefore, heat loss measurements would not be representative for normal operational conditions.

An approach to achieve the reduced uncertainty in measuring the convective losses of a flux-off method that does not require surface heating, is daytime flux-off testing. The testing scheme is shown in Figure 4.24. The underlying idea of this method is that, for a representative mode of operation of the cavity receiver during daytime, the heliostat field is defocused (time = t_1). At this point the surface temperatures are representative for operational conditions of the cavity

receiver. Without solar flux the surface temperatures decrease, resulting in decreasing heat loss. While no significant solar energy is incident on the receiver the HTF from the cold reservoir is pumped continuously through the receiver. At time t_2 the receiver temperature reaches a new thermal equilibrium, the heat loss is constant. At t_3 the heliostat field is refocused on the receiver, the surface temperatures and heat loss rises until they reach the initial equilibrium state at t_4.

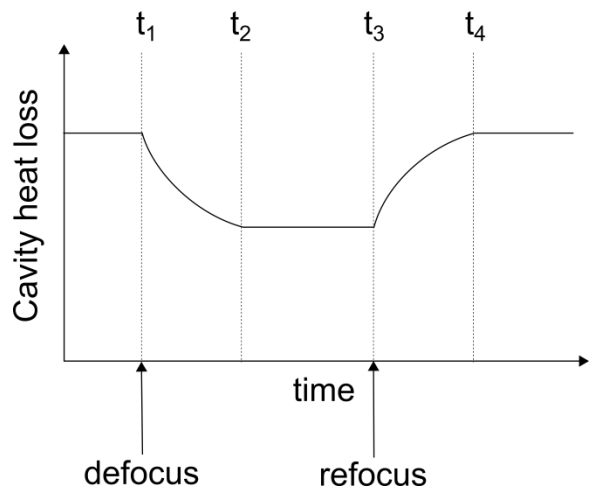

Figure 4.24 - Daytime flux-off testing scheme

Convection losses can be measured between time t_1 and t_3 when no flux is incident on the receiver and the measuring accuracy is acceptable. Measurements close to t_1 are most relevant because the cavity surface temperatures are closest to the operational conditions.

The measurement method uses the following energy balance of the receiver to determine convective losses:

$$\dot{Q}_{\text{convection}} = \dot{Q}_{\text{HTF}} + \dot{Q}_{\text{stored}} - \dot{Q}_{\text{radiation}} \tag{4.54}$$

The heat transfer from/to the HTF can be determined according to Eqn. (4.48), measuring mass flow rate, inlet- and outlet temperature of the HTF. Radiation losses are calculated with Eqn.(3.48), representative measurements of the surface temperatures of the cavity, surface emissivities and surface area are necessary. Additionally for daytime flux-off testing, the change in stored thermal energy in the receiver material has to be taken into account.

In the following analysis, a lumped capacitance assumption is used for the cavity surfaces in order to model the transient heat transfer from the cavity receiver. The internal conduction resistance of the receiver walls is assumed to be small in relation to the external heat transfer

resistances. An appropriate resistance ratio (Biot number) in Eqn. (4.55) validates the use of this assumption.

$$R_{ratio} = \frac{R_{cond}}{R_{HTF} + R_{rad} + R_{conv}} \tag{4.55}$$

Conduction resistance:

$$R_{cond} = \frac{L}{k \cdot A_c} = \frac{V_{cavity}}{k \cdot A_c \cdot A_s} \tag{4.56}$$

HTF resistance:

$$R_{HTF} = R_{HTF,cond} + R_{HTF,conv} = \frac{\ln\left(\frac{D_{tube,outer}}{D_{tube,inner}}\right)}{\pi \cdot L_{tube} \cdot k_{tube,avg} \cdot N_{tubes}} + \frac{2}{h_{HTF,avg} \cdot L_{tube} \cdot D_{tube,inner} \cdot \pi \cdot N_{tubes}} \tag{4.57}$$

Radiation resistance:

$$R_{rad} = \frac{T_{s,avg} - T_{amb}}{\dot{Q}_{radiation}} \tag{4.58}$$

Convection resistance:

$$R_{conv} = 0 \tag{4.59}$$

The convection resistance from the cavity surfaces to the ambient air is subject of the measurement method and is consequently not known. Setting this resistance to zero leads to a larger resistance ratio and therefore to a more conservative verification of the lumped capacitance approximation.

For representative modes of operation of the cavity receiver the resistance ratio R_{ratio} is between 0.02-0.035 which is sufficiently smaller than unity. The assumption, that the temperature drop due to internal conduction is negligible, is valid. The external heat transfer resistances dominate the heat transfer behavior of the system.

Assuming lumped capacitance behavior, the time constant of the cavity receiver can be determined according to Eqn. (4.60)

Time constant: $$\tau = R \cdot M \cdot c \tag{4.60}$$

The time constants for active and passive surfaces are calculated separately. For the active surfaces, the heat transfer resistance includes convection to/from the HTF, Eqn. (4.57) and radiation, Eqn.(4.58). Thermal mass of the tube material as well as the HTF is considered:

$$\tau_{active} = \left(R_{rad} + R_{conv,HTF}\right) \cdot \left(M_{\text{cavity}} \cdot c_{\text{cavity}} + M_{HTF} \cdot c_{HTF}\right) \tag{4.61}$$

The time constant for the passive surfaces only considers the radiation heat transfer resistance and the mass of the passive surfaces. While the wall thickness of the tubes that comprise the active surfaces is very small (about 1.25mm), we do not know the thickness or material type for the passive surfaces. We have assumed that the portion of the passive surfaces taking part in transient heat exchange is 3 times the tube wall thickness of the active surfaces.

$$\tau_{passive} = R_{rad} \cdot M_{\text{cavity}} \cdot c_{\text{cavity}} \tag{4.62}$$

The resulting time constant for the <u>active surfaces is 17 min</u>, and the time constant for the <u>passive surfaces</u> about <u>53 min</u>. The *time constant* is the time required for a surface to thermally respond after a change in the radiative flux. In comparison to the active surfaces, the passive surfaces are expected to experience insignificant temperature change during the testing process. With the given time constant, it can be taken that the most representative convection measurements can be done in the time window of about 15 min after the heliostat field is defocused. In that time the cavity has not fully thermally responded yet, the surface temperatures and the heat loss are near the same level as they were during flux-on cavity operation.

To assess the uncertainty in measuring the convective losses with this method, the influence of the stored energy inside the cavity material has to be considered. A first approximation is to determine the internal energy of the active and passive surfaces.

$$U_{active} = M_{active} \cdot c_{active} \cdot \left(T_{active,avg} - T_{amb}\right) \tag{4.63}$$

$$U_{passive} = M_{passive} \cdot c_{passive} \cdot \left(T_{passive,avg} - T_{amb}\right) \tag{4.64}$$

The resulting heat transfer from storage can be approximated with Eqn. (4.65)

$$\dot{Q}_{stored} = \frac{U_{active}}{3 \cdot \tau_{active}} + \frac{U_{passive}}{3 \cdot \tau_{passive}} \tag{4.65}$$

It is assumed that the stored energy inside the cavity elements is transferred to the ambient within the time of three time constants of the particular cavity element. For simplification, this heat transfer rate is assumed to be constant during the measurement. With these assumptions, the heat transfer due to storage is about 0.5% of the initial incident solar radiation or about a fifth of the convection loss that is predicted using the (Clausing, 1987) correlation. Consequently for daytime flux-off testing to give measurements with good accuracy, the influence of the stored energy inside the cavity material has to be known in detail. In general, the accuracy of daytime flux off testing with the given uncertainties in the measurement in Table 4.g is expected to be about 14% (Table 4.i). In our approximate calculation, the heat transfer due to the stored energy can be up to 20% of the convective losses. Not considering this effect would lead to unacceptably high uncertainties in the measuring of convection losses. A transient model of the cavity that simulates the thermal response of the cavity when radiation changes is necessary to measure convective losses accurately with the day time flux-off method.

5 Cavity Receiver Model in TRNSYS/SAM

The following section describes the implementation of the governing heat transfer equation in SAM using TRNSYS. The model is coded in FORTRAN, the code is attached in the digital supplement. It describes the structure of the TRNSYS model and the way the code is set up.

5.1 Cavity Heat Transfer Model

The global energy balance of the cavity receiver is given in Eqn. (5.1). The solar energy that is incident on the cavity can either be absorbed by the cavity surfaces or reflected out of the cavity, which is referred to as solar radiation loss. The energy that is absorbed by the cavity surfaces can either be transferred to the HTF as a useful energy gain of the system or lost due to temperature driven radiation loss or convective losses to the bulk air inside the cavity.

$$\text{Solar}_{\text{in}} = \underbrace{\text{SolarRadiation}_{\text{out}}}_{\text{reflected}} + \text{Heat}_{\text{HTF,out}} + \text{ThermalRadiation}_{\text{out}} + \text{Convection}_{\text{out}} \tag{5.1}$$

To analyze the thermodynamic system of the cavity receiver the energy balance will be solved for each computational surface segment of the cavity. As described in Section 2 and shown in Figure 2.1 the cavity is divided into surface segments that are assumed to be at constant temperature and that have constant properties. Our computational model is restricted to four panels, allows 1-10 nodes per panel and one node per passive surface. The energy balances for active and passive surfaces differ in the sense that the passive surfaces are assumed to not be irradiated directly by solar energy and not to transfer heat to the HTF. The energy balances are given on a nodal basis with four panels, N being the number of nodes per panel and the three passive surfaces. The energy balances are not solved for the opening of the cavity which is denoted as surface number $4N+4$. The cavity opening represents the ambient conditions and is therefore set constant to the ambient temperature provided by the weather data for the particular time step.

$$\dot{Q}_{solar,i} = \dot{Q}_{HTF,i} + \dot{Q}_{rad,thermal,i} + \dot{Q}_{rad,solar,i} + \dot{Q}_{convection,i} \quad \text{for } i = 1...4N+3 \tag{5.2}$$

The incident solar radiation $\dot{Q}_{solar,i}$ is taken from a flux map provided by a function included in SAM, this feature is described in Section 5.3. With the flux map the incident solar radiation is calculated as:

$$\dot{Q}_{solar,i} = A_i \cdot Flux_i \quad \text{for } i = 1...4N \tag{5.3}$$

Figure 5.1 show the separation of the cavity receiver in computational surface segments (nodes) and the number assignment.

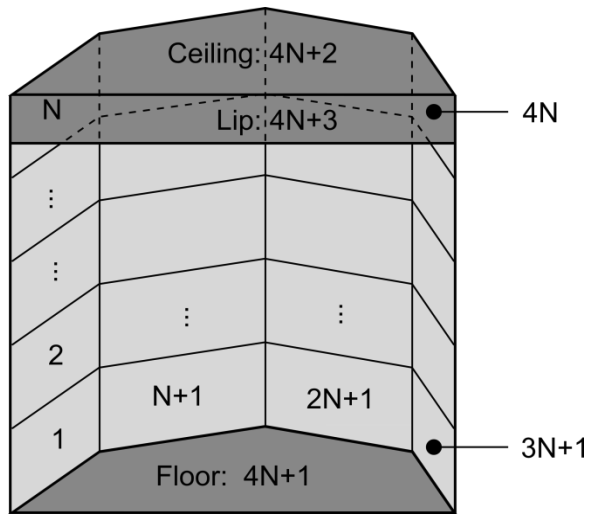

Figure 5.1 – Computation surface segments of the cavity receiver geometry

5.1.1 Heat transfer to the HTF

The heat transfer to the HTF at each node is calculated according to Eqn. (5.4),

$$\dot{Q}_{HTF,i} = UA_i \cdot \left(T_{s,i} - T_{HTF,i}\right) \tag{5.4}$$

The conductance UA_i combines the heat transfer resistances from the absorber surfaces to the HTF. The cavity receiver geometry is described in Section 2. The absorber surfaces consist of tube banks, half of the outer tube surface is irradiated, the HTF is conveyed inside the tube. UA_i consists of the conduction heat transfer resistance $R_{cond,i}$ through the pipe wall and the convection heat transfer resistance $R_{convection,i}$ from the internal pipe surface to the HTF.

$$UA_i = \frac{1}{R_{conduction,i} + R_{convection,i}} \tag{5.5}$$

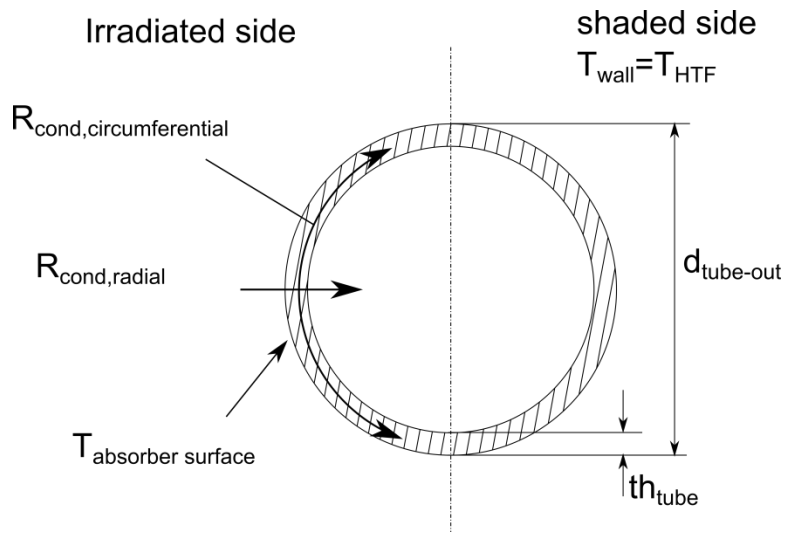

Figure 5.2 - Scheme of the heat transfer model of the HTF pipe

Heat conduction in circumferential direction will be neglected because it is small in relation to the conduction heat transfer in radial direction. To show this the Biot number, which in this case represents the ratio of the two heat transfer resistances, is calculated.

$$Bi = \frac{R_{cond,radial}}{R_{cond,circumferrential}} = \frac{\dfrac{\ln\left(\dfrac{r_{out}}{r_{in}}\right)}{2\pi Lk}}{\dfrac{2\pi \cdot r_{in}}{k \cdot \left(r_{out} - r_{in}\right) \cdot L}} = \frac{\left(r_{out} - r_{in}\right) \cdot \ln\left(\dfrac{r_{out}}{r_{in}}\right)}{4\pi^2 \cdot r_{in}} \tag{5.6}$$

For an outer tube diameter of d_{tube}=40 mm and a wall thickness of th_{pipe}=1.25 mm the Biot number is Bi=0.000109. These values are the defaults given by the System Advisor Model (SAM). But even for wall thicknesses that are ten times larger than the default value the Biot number is significantly smaller than 1. This result shows that the heat transfer resistance in circumferential direction is much higher than the heat transfer resistance in radial direction. The heat transfer in radial direction is dominant; in relation to that, the heat transfer in circumferential direction is negligible. Following this assumption we assume that the irradiated side of the HTF pipe is at the surface temperature of the absorber surface, while the opposite side is at the temperature of the HTF. In the calculation of the heat transfer resistances from the absorber surface to the HTF only half of the tube surface needs to be considered. Consequently the radial conduction resistance is calculated as:

$$R_{conduction,i} = \frac{\ln\left(\frac{D_{tube,outer}}{D_{tube,inner}}\right)}{\pi \cdot L_{tube\ per\ node} \cdot k_{tube,i} \cdot N_{tubes}} \tag{5.7}$$

With N_{tubes} being the number of parallel tubes in the surface segment and $k_{tube,i}$ the conductivity of the tube material. The convection heat transfer from the internal tube surface to the HTF is calculated according to:

$$R_{convection,i} = \frac{2}{h_{htf,i} \cdot L_{tube\ per\ node} \cdot D_{tube,inner} \cdot \pi \cdot N_{tubes}} \tag{5.8}$$

The convective heat transfer coefficient is calculated using laminar and turbulent flow correlations given in (Nellis, G. and Klein, S.A., 2009). As heat exchange surface only half of the pipe surface is considered.

5.1.2 Radiation Heat Transfer Model

The radiation heat transfer model is described in detail in Section 3.2.3. The thermal radiation heat transfer is calculated according to Eqn. (3.43) .

$$\begin{aligned}\dot{Q}_{therm,i,j} &= \sigma \cdot \varepsilon_{therm,i} \cdot \varepsilon_{therm,j} \cdot A_i \cdot \hat{F}_{therm,i,j} \cdot \left[\left(1 - f_{0-\lambda_{step},T_i}\right) \cdot T_i^4 - \left(1 - f_{0-\lambda_{step},T_j}\right) \cdot T_j^4 \right] \\ &+ \sigma \cdot \varepsilon_{solar,i} \cdot \varepsilon_{solar,j} \cdot A_i \cdot \hat{F}_{solar,i,j} \cdot \left[f_{0-\lambda_{step},T_i} \cdot T_i^4 - f_{0-\lambda_{step},T_j} \cdot T_j^4 \right]\end{aligned} \tag{3.43}$$

The solar radiation heat transfer is calculated accordingly by summing Eqn. (3.46)

$$\begin{aligned}\dot{Q}_{therm,i} &= \sigma \cdot \varepsilon_{therm,i} \cdot A_i \cdot \sum_{j=1}^{4N+4} \varepsilon_{therm,j} \cdot \hat{F}_{therm,i,j} \cdot \left[\left(1 - f_{0-\lambda_{step},T_i}\right) \cdot T_i^4 - \left(1 - f_{0-\lambda_{step},T_j}\right) \cdot T_j^4 \right] \\ &+ \sigma \cdot \varepsilon_{solar,i} \cdot A_i \cdot \sum_{j=1}^{4N+4} \varepsilon_{solar,j} \cdot \hat{F}_{solar,i,j} \cdot \left[f_{0-\lambda_{step},T_i} \cdot T_i^4 - f_{0-\lambda_{step},T_j} \cdot T_j^4 \right]\end{aligned} \tag{3.46}$$

5.1.3 Convective Heat Loss Model

The convection loss from each surface segment is calculated according to Eqn. (5.9) with $h_{conv,i}$ the convection heat transfer coefficient from each node and the bulk temperature of air inside the cavity according to (Clausing, 1983) presented in Section 4.2.1.

$$\dot{Q}_{conv,i} = A_i \cdot h_{conv,i} \cdot \left(T_i - T_{bulk}\right) \tag{5.9}$$

Eqn. (5.9) requires a local convective heat transfer coefficient for every surface segment in the cavity. In Section 0 several convection correlations are presented. (Clausing, 1983) offers the only established correlation that provides a local heat transfer coefficient for the vertical panels, the upward facing cavity floor and of the surfaces in the stagnant zone. All other correlations only provide an overall heat transfer coefficient of the cavity. Because the (Clausing, 1983) correlation provides a comparably low overall heat loss, more recent correlations that predict higher losses are favored. Two methods to implement convective losses in the heat transfer model are described and applied in the software to work around this problem. Detailed description can be found in Section 5.3.1 and 5.3.2.

5.2 Model of the Solar Tower Power Plant in TRNSYS

The model of the power plant is simulated using the Transient System Simulation Tool, TRNSYS (Klein, S.A. et al., 2007). TRNSYS enables the user to simulate any type of thermodynamic system as an interacting network of components. This system can be solved for time dependent weather input data. TRNSYS is used to do a quasi transient simulation of our solar tower power plant model. The steady state solution for hourly weather data input, such as Direct Normal Irradiation (DNI), temperatures etc, is used.

The components that are called by TRNSYS to simulate the model are independent subprograms written in FORTRAN that are compiled into the TRNDll.dll. These subprograms are built according to a template that makes it possible to create user specified components, modeling thermodynamic processes that are not represented by the components in the TRNSYS library. These components are also called TYPEs with a consecutive definite 3 digit number. To model the solar tower power plant the following main components are used.

Component name	**TYPE number**	**Author**
Weather Data	15	TRNSYS integrated
Substance properties	229	M.Wagner
Interpolator	9	TRNSYS integrated
Heliostat Field	221	R. Pitz-Paal ,M.Wagner
Cavity Receiver	232	L.Feierabend, M.Wagner, S.Teichel
CSP plant controller (includes HTF storage tanks and piping)	251	M.Wagner
Rankine Cycle	224	M.Wagner
Parasitic Losses	228	M.Wagner

Table 5.a - TRNSYS Types that comprise the Solar Tower Model

To model a solar tower power plant with a cavity receiver, the cavity receiver subprogram (TYPE 232) was written by Lukas Feierabend. The changes in the radiation heat transfer model of the cavity receiver have to be implemented only in this component.

5.3 Implementation of the Cavity Receiver Model in FORTRAN

The structure of the TYPE 232 will be described in order to give an understanding of how the subroutine of the cavity receiver model works and how the modifications of the radiation heat transfer model are implemented.

Like every component in TRNSYS, the TYPE 232 is defined as a subroutine with the same set of subroutine parameters: Simulation time; array of inputs (time dependent); array of outputs, set of arrays defining the derivatives of variables with respect of time; array of parameters (inputs that are independent of time) and a set of arrays that controls the calculation procedure inside the subroutine.

In the following lines of the TRNSYS template, the variables are defined and the elements of the arrays are associated with more distinct variable names to identify their purpose in the following code. The variable association is controlled to happen at certain times of the simulation, inputs, parameters and control variables are defined at the very beginning of the simulation, the output variables are associated at the end of the simulation. After all initialization steps at the beginning of the simulation are done the actual receiver model is run. Complex processes needed to solve the cavity receiver model are either annexed as a subroutine in the type itself or are included in the TRNDll as a separate TYPE and can be called by the cavity receiver model.

The general structure of the cavity receiver component TYPE 232 is shown in Figure 5.3.

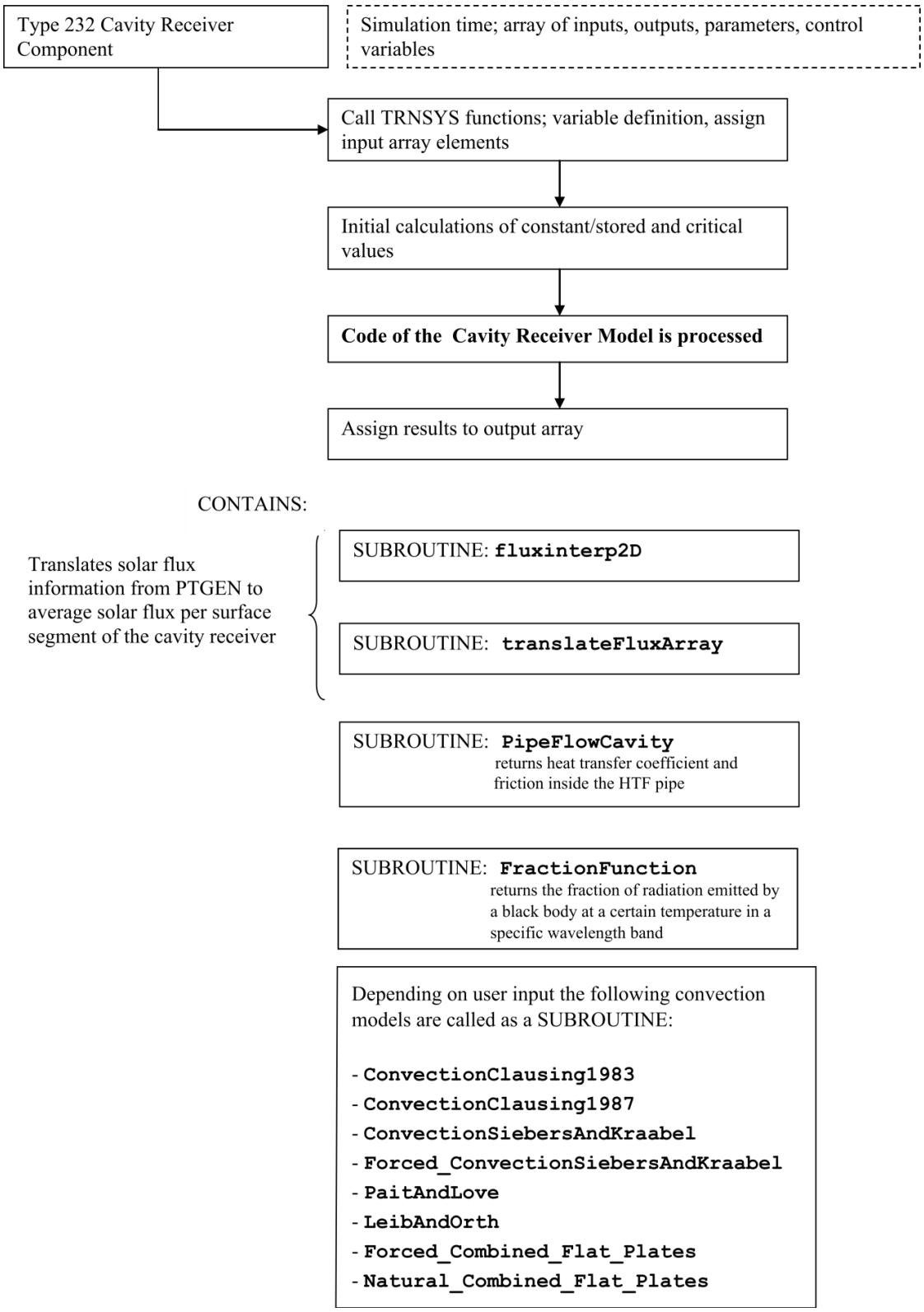

Figure 5.3 – General structure of TYPE 232

At the beginning of the cavity receiver model code, calculations are done that only need to be calculated once at the beginning of the simulation and not for every time step or iteration loop. The geometric quantities of the cavity receiver such as, panel height, angle of aperture, width of the receiver, geometry of the lip, etc. are calculated from the input parameters. With this information, external subroutines are called to calculate the view factors of the surface segments of the cavity receiver geometry. These subroutines were written by (Feierabend, 2009). After the definition of the view factors, the $\hat{F}$ - parameters are calculated. Two sets of $\hat{F}$ - parameters are calculated one for the solar and one for the thermal emissivity as described in Section 3.2.3. The calculation of the view factors and the $\hat{F}$ - parameters needs only to be done once in a simulation, although the radiation model needs to be solved for every iteration in every time step. The FORTRAN code is written so that the $\hat{F}$ - parameters are calculated only when parameter $INFO(7) = -1$, at the very first step in the simulation. This implementation results in significantly shorter computation time. Compared to the radiosity method, one significant advantage of the $\hat{F}$ - method is that the $\hat{F}$ - parameters only require this initial calculation whereas the radiosity method require updated vales to be calculated at each time step in order to properly account for the radiation heat transfer. The $\hat{F}$ - parameters that include for reflection in the model only depend on cavity geometry and emissivity which are constant over the simulation time. Using the radiosity method (Section 3.2.1) accounts for reflection also in dependence on surface temperature. The reflection influence needs to be recalculated every time step. The $\hat{F}$ - parameters are determined with the Eqn. (3.21) which cannot be solved without knowing all interacting parameters.

$$\hat{F}_{i,j,\lambda} = F_{i,j} + \sum_{k=1}^{n} \rho_{k,\lambda} \cdot F_{i,k} \cdot \hat{F}_{k,j,\lambda} \quad \text{for } i = 1..N \text{ and } j = 1..N \tag{3.21}$$

The equation is solved using a successive substation iteration method, the view factor provide a good initial value. The $\hat{F}$ - parameters are determined with a high absolute tolerance of 10^{-30} which can be usually obtained in less than 20 iteration steps.

At the beginning of each time step, the solar flux map is read to calculate the incident solar radiation on the panels using the subroutines `fluxinterp2D` and `translateFluxArray` (Feierabend, 2009). The subroutine `fluxinterp2D` reads the fluxmap output by the PTGEN.exe program (Wagner, 2008) and locates the flux map closest to the requested azimuth,

zenith angle, returning it in an array. The `translateFluxArray` subroutine translates the ourput flux array from `fluxinterp2D` in an array with averaged flux values for each panel node. This flux map depends on weather data included into TRNSYS and the heliostat component, providing field efficiency. Startup requirements for the cavity receiver are specified in the initiation code in order to avoid unnecessary mass flow of heat transfer fluid through the cavity receiver during times of insufficient solar radiation. A critical solar radiation is defined as a fraction the total incoming solar radiation. Final plausibility checks of the determined values representing the incident radiation are done, to make sure the solar position called is plausible, before the solar flux map is translated to an average incident solar flux on each surface segment of the cavity receiver. In the next step, the initial guess values of the surface temperature and the heat transfer fluid are set. Guess values for the surface temperatures of the cavity are set to the desired outlet temperature of the heat transfer fluid; the opening of the cavity is set to sky temperature for all time steps. The temperature of the heat transfer fluid at every node of the cavity panel surfaces is set to the mean of the predefined in- and outlet temperature of the HTF.

$$\begin{aligned} T_{s,X} &= T_{htf-hot-design} \\ T_{opening} &= T_{sky} \\ T_{ht,fX} &= \frac{\left(T_{htf-out-design} + T_{htf-in-design}\right)}{2} \end{aligned} \tag{5.10}$$

With the guess values of the temperatures and an assumed initial guess value for the thermal efficiency of the cavity receiver, the first guess properties, mass flow and temperatures of the HTF for each panel, depending on the chosen flow pattern can be calculated.

$$\dot{m}_{htfX,panel} = \frac{\eta_{thermalX} \cdot \dot{q}_{solar,panel}}{c_{htf} \cdot \left(T_{htf,hot} - T_{htf,cold}\right)} \tag{5.11}$$

$$T_{htf,i} - T_{htf,htf,i-1} = \frac{\eta_{thermalX} \cdot \dot{q}_{solar,i}}{c_{htf} \cdot \dot{m}_{htfX,i}} \tag{5.12}$$

With these first guess values, an iteration process is used to solve the energy balance of cavity surface to obtain surface temperatures, the temperature of the HTF at every node of the cavity model and subsequently the heat losses and performance of the receiver.

Different energy balances of the surface nodes are used, depending on the implementation method of the convective losses. The code provides two different methods to include convective

losses in the cavity receiver model. This implementation was necessary because the energy balance for each surface as it is stated in Section 5.1 requires a convective loss coefficient for each computational surface segment of the cavity receiver. However, none of the correlations presented in Section 0 provides this information. Except for the cavity receive correlation from (Clausing, 1983) all correlations only provide an overall convective loss coefficient for the receiver. (Clausing, 1983) divides the receiver in three different convective loss zones with separate heat transfer coefficients; absorber panels, floor and stagnant zone at the top of the receiver.

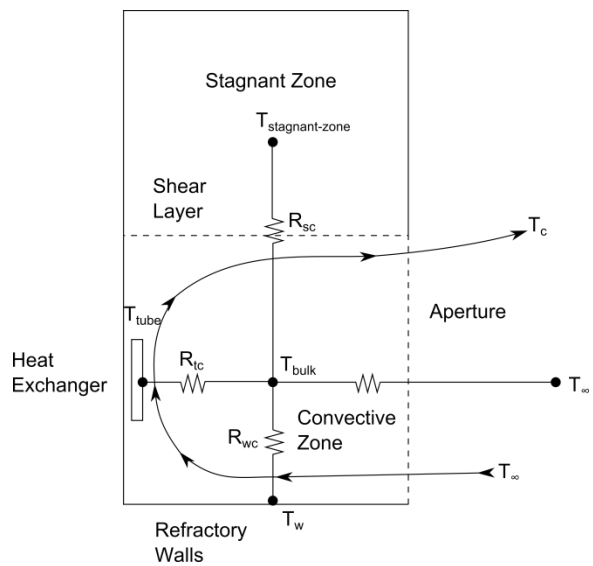

Figure 4.3 - Network representation of the convection loss mechanism – from (Clausing, 1983).

5.3.1 Uncoupled Convection Implementation

For his model (Feierabend, 2009) uses the uncoupled convection model which excludes the convection loss from the energy balances. The cavity surface temperatures and the temperatures of the HTF are calculated independently of convection loss. With these temperatures the total convection loss of the cavity is calculated using one of the presented convection correlations. To account for convective losses, the heat transfer to the HTF (the useful energy gain) is reduced by the convection losses.

$$\dot{Q}_{HTF,with\ convection\ loss} = \dot{Q}_{HTF,without\ convection\ loss} - \dot{Q}_{convection\ loss} \tag{5.13}$$

In this way convection losses can be included in the overall receiver performance without the need of local convective loss coefficients for each cavity surface segment. Because the surface temperatures are calculated without convective losses, this method predicts surface temperatures that are too high, leading to increased radiation and convective losses. On the other hand this method makes it possible to account for convective losses of the cavity without making assumptions about the convective loss distribution inside the cavity.

5.3.2 Coupled Convection Implementation

In the coupled convection implementation method, convection losses are included in the energy balance of each surface. The surface temperatures are determined in dependence on (coupled with) convective losses. This leads to a more physical simulation of the cavity receiver but also requires an assumption of the convection loss distribution inside the cavity, since this information in not given by any of the established convection correlations. The only published correlation that provides local convection losses coefficient is (Clausing, 1983), shown in Section 4.2.1. This correlation provides three heat transfer coefficients to consider the different convection loss mechanism of the surface segments in the cavity receiver.

Convection heat transfer from the cavity floor is represented as:

$$\dot{Q}_{conv,floor} = A_{floor} \cdot h_{conv,floor} \cdot \left(T_{floor} - T_{bulk}\right) \tag{5.14}$$

Convection heat transfer from the unshaded vertical surface segments to the surroundings is given by:

$$\dot{Q}_{conv,active,i} = A_i \cdot h_{conv,active} \cdot \left(T_{s,i} - T_{bulk}\right) \quad \text{with: } i = 1..\ 4 \cdot N \tag{5.15}$$

The overall heat transfer from the stagnant zone is given by:

$$\dot{Q}_{conv,stag,i} = \frac{A_{floor}}{3} \cdot h_{conv,stag} \cdot \left(T_{stag} - T_{bulk}\right) \tag{5.16}$$

The effective heat exchange surface between stagnant zone and bulk flow is given by Clausing to be one-third of the contact area. The temperature of the stagnant is calculated as the mean

temperature of all surfaces in the stagnant zone. The (Clausing, 1983) correlations are only valid for temperature ratios $1 < T_W / T_\infty < 2.6$. For higher temperature ratios the correlations lead to unreasonable results. To avoid computational problems in the code the surface temperatures used in the implementation of this correlation in the cavity model are limited to values of that ratio, even if higher surfaces temperatures are calculated. The Clausing model provides convective loss coefficients for the surfaces on the absorber panels and the floor but not for the individual surfaces in the stagnant zone. While the coefficients for floor and panels can be used directly, steps have to be taken to approximate the heat transfer coefficients form the computational nodes in the stagnant zone. To do so the convective loss distribution from each surface in the stagnant zone is area weighted.

$$\dot{Q}_{conv,stag,i} = \dot{Q}_{conv,stag} \cdot \frac{A_i}{\sum_{i=m\cdot N-S+1}^{m\cdot N} A_i} \quad \text{with } m = [1,2,3,4] \tag{5.17}$$

The parameter S in represents the number of surfaces in the stagnant zone, which includes ceiling, lip and a section of the active surfaces. S is calculated as:

$$S = \left\lceil \frac{H_{lip}}{H_{panel} \cdot \frac{1}{N}} \right\rceil \tag{5.18}$$

The ceiling value is used in Eqn. (5.18), including the total surface of the row of computational nodes of the active surface that are only partially located in the stagnant zone. For these partially shaded surfaces that are denoted with $m \cdot N - S$, the local convective heat transfer is calculated as an area weighted sum of convective losses corresponding to the unshaded active surfaces and from the stagnant zone:

$$\dot{Q}_{conv,stag,i} = h_{convection,active} \cdot \underbrace{\left(S \cdot A_i - W_{panel} \cdot H_{lip}\right)}_{\substack{\text{surface area that is not} \\ \text{in the stagnant zone}}} \cdot \left(T_{s,i} - T_{bulk}\right) + \dot{Q}_{conv} \cdot \underbrace{\frac{\left|(S-1) \cdot A_i - W_{panel} \cdot H_{lip}\right|}{A_{stag}}}_{\substack{\text{fraction of surface area of i} \\ \text{in the stagnant zone}}}$$

$$\text{with } i = m \cdot N - S \;; \quad m = [1,2,3,4] \tag{5.19}$$

The individual convective heat transfer coefficient is then calculated according Eqn. (5.20), using the current surface temperatures.

$$h_{conv,i} = \frac{\dot{Q}_{conv,i}}{A_i \cdot \left(T_{s,i} - T_{bulk}\right)} \tag{5.20}$$

This approximation makes clear that there is a need to improve the convection model. To obtain reliable results using the coupled convection method, more accurate information about the spatial distribution of the convection loss inside the cavity is necessary.

To be able to use other convection correlations than (Clausing, 1983) the same relative convective loss distribution is used. With a scale factor the total convection loss is adjusted to obtain the same over all convection loss, which is predicted by more recent models.

$$h_{conv,i} = f_{scale} \cdot h_{\text{Clausing}(1983),i} \tag{5.21}$$

With:

$$f_{scale} = \frac{\text{total convection loss - current convection model}}{\text{total convection loss - Clausing}(1983)} \tag{5.22}$$

An approach to approximate forced convective loss of the cavity receiver was described by (Siebers, D. and Kraabel, J., 1984), presented in Section 4.2.3. To include the forced convection effect given by that section the resulting forced convection heat transfer coefficient is added to the coefficient obtained in Eqn. (5.21).

$$h_{conv,mixed,i} = h_{conv,i} + h_{conv,\,forced} \quad \text{for } i = 1...4N+3 \tag{5.23}$$

Input parameters are defined in the code to enable the user to choose how to consider convective losses in the cavity receiver simulation.

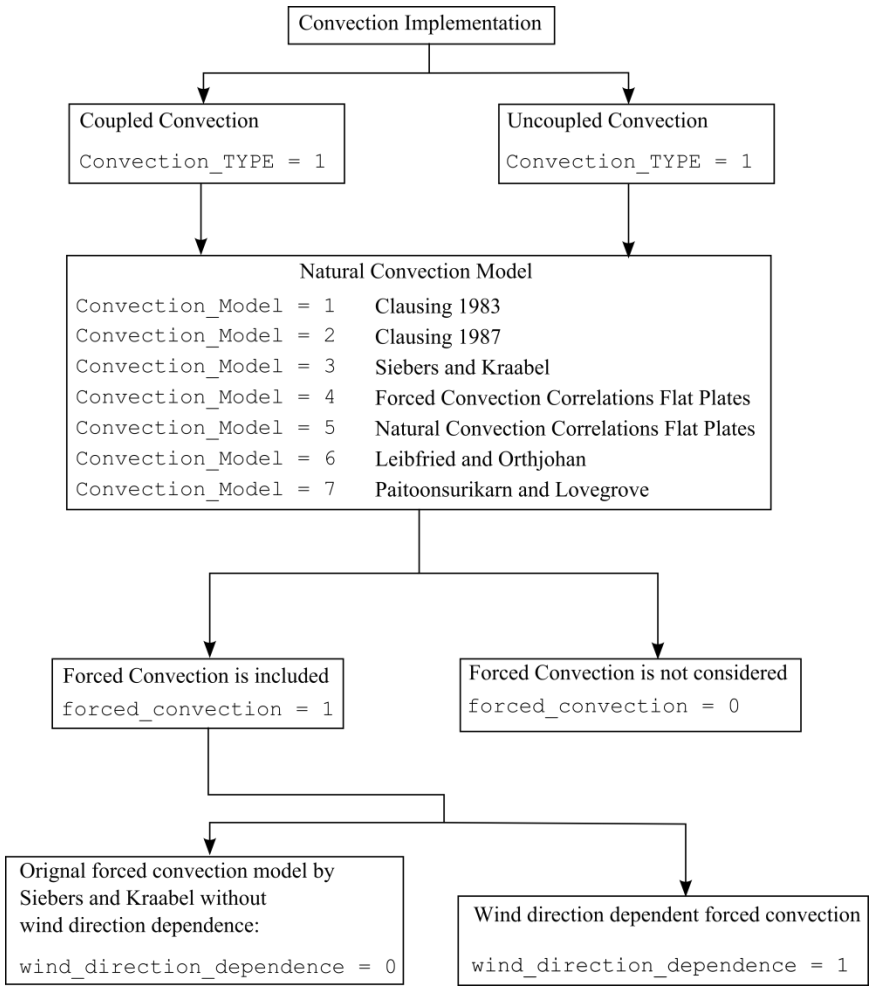

Figure 5.4 – Parameters in the model to choose the convection implementation method

5.3.3 Iterative scheme to solve the energy balances

The iterative scheme of the cavity model changes, depending on the convection implementation method. The implementation of the coupled convection method will be discussed in greater detail here because it is the more complex and the more relevant method. The uncoupled method can be understood as a simplification of the coupled convection implementation method.

To solve for the surface temperatures in dependence on all loss mechanism using the coupled convection method, two nested iteration loops are used. The schematic structure is shown in Figure 5.5.

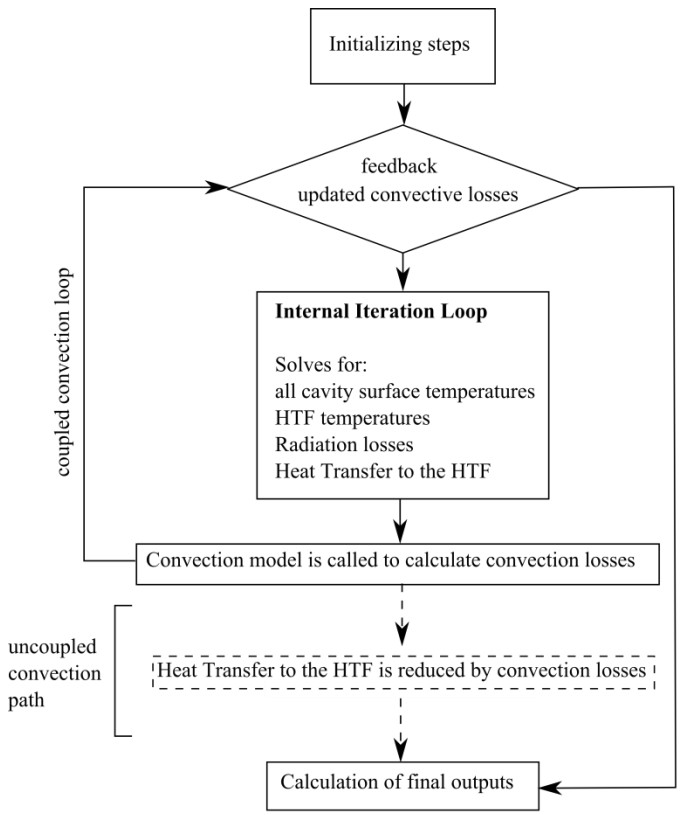

Figure 5.5 – Simplified Schematic Iteration Method

To calculate the convection loss one of the convection correlations described in Section 0 is called as a subroutine. The subroutines require the surface temperatures of the cavity as an input. To avoid convergence problems with the convection model due to unrealistic input temperatures that occur during the temperature iteration process it is called independently in an external iteration loop. The internal iteration loop solves for the surface temperature considering

temperature dependent radiative losses and transfer to the HTF and constant convection losses. The convection losses are then updated using the current surface temperatures. This process is repeated by the external iteration loop until the relative change of the updated convection loss is smaller than 10^{-6} or 100 iterations were done. If the tolerance is not reached within 100 iteration steps the program proceeds with the last result. Even if no convergence is obtained the convection loop is not expected to provide unreasonable results for the convection loss. The temperature iteration is the less stable process; if a problem occurs in the code it will cause the internal iteration loop to break before the external loop is processed.

$$error_{convection} = \frac{\dot{Q}_{convection,OLD} - \dot{Q}_{convection,NEW}}{\dot{Q}_{convection,NEW}} \tag{5.24}$$

For the first temperature iteration process no convection loss is assumed. For the uncoupled convection implementation the external loop is disabled, the receiver temperatures obtained without convective losses are used to determine the final receiver performance.

To determine the cavity temperatures in the internal iteration loop the energy balances need to be solved. The equations with subscripts *i,j* are solved for all surfaces in the cavity, with N being the number of surfaces per panel, there are four panels and three passive surfaces. The temperature of the opening surface is representing the ambient and is therefore set constant to ambient temperature. With the coupled convection implementation the general energy balance for the cavity surfaces is according to Section 5.1:

$$\dot{Q}_{solar,i} = \dot{Q}_{HTF,i} + \dot{Q}_{rad,thermal,i} + \dot{Q}_{rad,solar,i} + \dot{Q}_{convection,i} \quad \text{for } i = 1...4N+3 \tag{5.2}$$

$$A_i \cdot Flux_i = UA_i \left(T_{s,i} - T_{HTF,i}\right) + A_i \cdot \sum_{j=1}^{4N+4} \left[h_{rad,therm,i,j} \cdot \left(T_{s,i} - T_{s,j}\right)\right] + \dot{Q}_{rad,solar,i} + A_i \cdot h_{conv,i} \cdot \left(T_{s,i} - T_{bulk}\right) \quad \text{for } i, j = 1...4N+4 \tag{5.25}$$

Eqn. (5.25) is solved for the receiver surface temperatures $T_{s,i}$.

$$A_i \cdot Flux_i = UA_i \cdot T_{s,i} - UA_i \cdot T_{HTF,i} + A_i \cdot T_{s,i} \sum_{j=1}^{4N+4} \left[h_{rad,therm,i,j} \right] - \sum_{j=1}^{4N+4} \left[h_{rad,therm,i,j} \cdot T_{s,j} \right] + \dot{Q}_{rad,solar,i} + A_i \cdot h_{conv,i} \cdot T_i - A_i \cdot h_{conv,i} \cdot T_{bulk} \tag{5.26}$$

$$T_{s,i} = \frac{A_i \cdot Flux_i + UA_i \cdot T_{HTF,i} + \sum_{j=1}^{4N+4} \left[h_{rad,therm,i,j} \cdot T_{s,j} \right] - \dot{Q}_{rad,solar,i} + A_i \cdot h_{conv,i} \cdot T_{bulk}}{UA_i + A_i \sum_{j=1}^{4N+4} \left[h_{rad,therm,i,j} \right] + A_i \cdot h_{conv,i}} \tag{5.27}$$

Because the solar radiation heat transfer is independent of surface temperature it can be calculated by summing Eqn. (3.45) for every surface j and be included directly in Eqn. (5.26).

$$\begin{aligned} \dot{Q}_{solar,i,j} = {} & f_{0-\lambda_{step},T_{sun}} \cdot \hat{F}_{solar,i,j} \cdot A_i \cdot \left[Flux_{solar,i} \cdot \left(1-\varepsilon_{solar,i}\right) \cdot \varepsilon_{solar,j} - Flux_{solar,j} \cdot \left(1-\varepsilon_{solar,j}\right) \cdot \varepsilon_{solar,i} \right] \\ & + \left(1 - f_{0-\lambda_{step},T_{sun}}\right) \cdot \hat{F}_{therm,i,j} \cdot A_i \cdot \left[Flux_{solar,i} \cdot \left(1-\varepsilon_{therm,i}\right) \cdot \varepsilon_{therm,j} - Flux_{solar,j} \cdot \left(1-\varepsilon_{therm,j}\right) \cdot \varepsilon_{therm,i} \right] \end{aligned} \tag{3.45}$$

$$\dot{Q}_{solar,i} = \sum_{j=1}^{4N+4} \dot{Q}_{solar,i,j} \tag{5.28}$$

The radiation heat transfer rates require the fraction $f_{0-\lambda_{step},T}$. This is done in the subroutine `FractionFunction`. Because it is not practical to solve the integral in Eqn. (3.35) in a computational model like this cavity receiver model, the series expansion provided by (Siegel R.and Howell J.R., 2002) is used.

$$f_{0-\lambda_{step},T} = \frac{15}{\pi^4} \sum_{n=1}^{\infty} \left[\frac{\exp(-n\zeta)}{n} \left(\zeta^3 + \frac{3\zeta^2}{n} + \frac{6\zeta}{n^2} + \frac{6}{n^3} \right) \right] \tag{5.29}$$

Following the advice by (Beckman, 1968) the summation of ten terms is considered to provide sufficient accuracy.

To include the temperature driven radiation heat transfer model in a way that makes it possible to solve for the surface temperature Eqn. (3.46) is stated in terms of a heat transfer coefficient shown in Eqn. (5.30) and Eqn. (5.31).

$$\begin{aligned} \dot{Q}_{therm,i} = {} & \sigma \cdot \varepsilon_{therm,i} \cdot A_i \cdot \sum_{j=1}^{4N+4} \varepsilon_{therm,j} \cdot \hat{F}_{therm,i,j} \cdot \left[\left(1 - f_{0-\lambda_{step},T_{s,i}}\right) \cdot T_{s,i}^4 - \left(1 - f_{0-\lambda_{step},T_{s,j}}\right) \cdot T_{s,j}^4 \right] \\ & + \sigma \cdot \varepsilon_{solar,i} \cdot A_i \cdot \sum_{j=1}^{4N+4} \varepsilon_{solar,j} \cdot \hat{F}_{solar,i,j} \cdot \left[f_{0-\lambda_{step},T_{s,i}} \cdot T_{s,i}^4 - f_{0-\lambda_{step},T_{s,j}} \cdot T_{s,j}^4 \right] \end{aligned} \tag{3.46}$$

$$\dot{Q}_{rad,thermal,i,j} = h_{rad,therm,i,j} \cdot A_i \cdot \left(T_{s,i} - T_{s,j}\right) \tag{5.30}$$

$$h_{rad,therm,i,j} = \sigma \cdot \varepsilon_{therm,i} \cdot \frac{\sum_{j=1}^{4N+4} \varepsilon_{therm,j} \cdot \hat{F}_{therm,i,j} \cdot \left[\left(1 - f_{0-\lambda_{step},T_{s,i}}\right) \cdot T_{s,i}^4 - \left(1 - f_{0-\lambda_{step},T_{s,j}}\right) \cdot T_{s,j}^4 \right]}{\left(T_i - T_j\right)} + \sigma \cdot \varepsilon_{solar,i} \cdot \frac{\sum_{j=1}^{4N+4} \varepsilon_{solar,j} \cdot \hat{F}_{solar,i,j} \cdot \left[f_{0-\lambda_{step},T_{s,i}} \cdot T_{s,i}^4 - f_{0-\lambda_{step},T_{s,j}} \cdot T_{s,j}^4 \right]}{\left(T_{s,i} - T_{s,j}\right)} \tag{5.31}$$

For the implementation of Eqn. (5.31) in the FORTRAN code, there are situations where $T_{s,i} = T_{s,j}$ leading to division by zero. This situation occurs for $i = j$ and in the first iteration of each time step because the surface temperatures are set to the outlet temperature of the HTF as a first guess. An `IF-statement` is used to set the heat transfer coefficient to 10^{-6} for these cases. From the physical standpoint a very small value makes sense because there will be no temperature driven heat transfer between two surfaces with the same temperatures. The thermal radiation heat transfer coefficient is not set to zero, Eqn. (5.27) however divides by the sum of the heat transfer coefficients and there are cases where a thermal radiation heat transfer coefficient of zero results in a division by zero for this equation. To avoid this issue the heat transfer is set to a very small value for the case of a driving temperature difference of zero.

The radiation heat transfer coefficient is used to solve for the surface temperatures (Eqn. (5.27)) using the guess values of the surface temperatures. With the new surface temperatures the heat transfer rate to the HTF at each surface node is determined with Eqn. (5.5).

$$\dot{Q}_{HTF,i} = UA_i \cdot \left(T_{s,i} - T_{HTF,i}\right) \tag{5.5}$$

The thermal radiation heat transfer between all surfaces is also calculated with the new surface temperatures, according to Eqn. (3.43).

$$\dot{Q}_{therm,i,j} = \sigma \cdot \varepsilon_{therm,i} \cdot \varepsilon_{therm,j} \cdot A_i \cdot \hat{F}_{therm,i,j} \cdot \left[\left(1 - f_{0-\lambda_{step},T_i}\right) \cdot T_i^4 - \left(1 - f_{0-\lambda_{step},T_j}\right) \cdot T_j^4 \right] + \sigma \cdot \varepsilon_{solar,i} \cdot \varepsilon_{solar,j} \cdot A_i \cdot \hat{F}_{solar,i,j} \cdot \left[f_{0-\lambda_{step},T_i} \cdot T_i^4 - f_{0-\lambda_{step},T_j} \cdot T_j^4 \right] \tag{3.43}$$

The solar radiation heat transfer was calculated earlier in the program, together with the thermal radiation heat transfer coefficients. The total radiation heat transfer between all surfaces is now calculated as the sum of thermal and solar radiation. The net heat transfer rates are calculated by summing the heat transfer rates for each surface *j*. Also the convection loss from each surface is

calculated according to Eqn. (5.9) as well as the total convection loss of the cavity by summing the individual convection losses.

In the next step in the program, the heat transfer to the HTF per panel is calculated by summation of the heat transfer rates per node of each surface. Using the new surface temperature $T_{s,i}$, the heat transfer rate to the HTF is updated. To maintain the same inlet and outlet temperatures of the HTF, the mass flow rate has to be corrected, according to the flow pattern in the active surfaces with:

$$\dot{m}_{HTF,panel} = \frac{\dot{Q}_{HTF,panel}}{c_{HTF} \cdot \left(T_{HTF,hot} - T_{HTF,cold}\right)} \tag{5.32}$$

To calculate the resulting temperature of the HTF at each node of a panel the following equation based on an energy balance on the HTF is applied. Depending on the chosen flow pattern of the HTF along the receiver surfaces the location of the downstream receiver surfaces (i-1) changes

$$T_{HTF,i} = \frac{\dot{Q}_{HTF,i}}{c_{HTF} \cdot \dot{m}_{HTF,panel}} + T_{HTF,i-1} \tag{5.33}$$

These calculations are done for all surfaces in the cavity. The passive surfaces however are assumed to be adiabatic which simplifies the energy balance. The same equations are solved but the irrelevant terms are set to zero. With no incoming solar flux and no heat transfer to the HTF the energy balance in Eqn. (5.2) simplifies to Eqn.(5.34) for the passive surface temperatures:

$$0 = \dot{Q}_{rad,thermal,i} + \dot{Q}_{rad,solar,i} + \dot{Q}_{convection,i} \quad \text{for } i = 4N+1 \ldots 4N+3 \tag{5.34}$$

Solving for the passive surface temperatures consequently leads to:

$$T_{s,i} = \frac{\sum_{j=1}^{4N+4} \left[h_{rad,therm,i,j} \cdot T_{s,j} \right] - \dot{Q}_{rad,solar,i} + A_i \cdot h_{conv,i} \cdot T_{bulk}}{A_i \sum_{j=1}^{4N+4} \left[h_{rad,therm,i,j} \right] + A_i \cdot h_{conv,i}} \tag{5.35}$$

As mentioned before all these equations are solved in the internal iteration loop. Convergence is reached when the relative change of HTF outlet temperature and HTF mass flow are below a certain value within the maximum step of iterations. If no convergence could be obtained, all

receiver parameters are set to their non-operation-values and the simulation of the next time step starts.

$$error_{T_{HTF,out}} = abs\left(\frac{T_{HTF,out,NEW} - T_{HTF,out,OLD}}{T_{HTF,out,OLD}}\right) \tag{5.36}$$

$$error_{\dot{m}_{HTF,out}} = abs\left(\frac{\dot{m}_{HTF,out,NEW} - \dot{m}_{HTF,out,OLD}}{\dot{m}_{HTF,out,OLD}}\right) \tag{5.37}$$

To obtain better convergence a successive relaxation method is used. The obtained HTF, and surface temperatures from the last iteration step are not used as a direct input for the following iteration step but instead a weighted mean temperature of last and current temperature is used. This “relaxation temperature” is calculated according to:

$$T_{relaxation} = \gamma \cdot T_{new} + (1-\gamma) \cdot T_{old} \tag{5.38}$$

The relaxation factor γ is defined as one of the elements of the predefined relaxation factor array $\gamma = [1,\ 0.8,\ 0.6,\ 0.4,\ 0.2,\ 0.1,\ 0.05]$. The initial value of γ is unity, it decreases step wise if no convergence was obtained within a maximum iteration step number of 100. With lower values for the relaxation factor the calculation of each iteration step takes more time, but it is more robust. The FORTRAN model is programmed to choose the highest possible gamma value to obtain convergence. With this method very low convergence tolerances can be realized. All calculations can be solved for a tolerance of 10^{-14}. To reduce the calculation time of the model the tolerance is set to 10^{-8}.

After the external and internal iteration loop reached convergence, the heat losses, surfaces temperatures and the temperature of the HTF in the receiver are known. The total mass flow rate of the HTF is updated to obtain the predefined HTF outlet temperature according to:

$$\dot{m}_{HTF,total} = \frac{\dot{Q}_{HTF,total}}{c_{HTF} \cdot \left(T_{HTF,hot} - T_{HTF,cold}\right)} \tag{5.39}$$

Plausibility checks are done to make sure that the HTF mass flow is within predefined limits. Also the operational mode of the power plant is updated. If the heat transfer to the HTF is not sufficient to provide power to the plant, it is shut off or set into startup mode.

In the following step the cavity receiver efficiency is calculated:

$$\eta_{thermal} = \frac{\dot{Q}_{htf,total}}{\dot{Q}_{solar,total}} \tag{5.40}$$

The last modeling steps in the code determine the required power to maintain the mass flow of the HTF with:

$$\dot{W}_{pump} = \dot{m}_{htf,total} \left(H_{tower} \cdot g_{grav} + \frac{\Delta p_{avg}}{\rho_{htf}} \right) \cdot \frac{1}{\eta_{pump}} \tag{5.41}$$

The average pressure drop Δp_{avg} inside the receiver tubes is calculated as a mass flow rate weighted average per tube. Depending on the flow pattern of the HTF along the absorber surfaces flow resistances such as bends and tube length are taken into account. A detailed description of the available flow patterns, the implementation method and the influence on the receiver performance can be found in (Feierabend, 2009). Since the heat transfer situation to the HTF did not change significantly this study is still valid although it was done for black surfaces.

The final computational steps in TYPE232 calculate the significant output values and assigns these to the `OUT-array`. The subroutines that are exclusive for the cavity type are included at the end of the code. The basic structure of the subroutine is shown in Figure 5.6; the dashed line indicates the external iteration loop necessary for the coupled convection model.

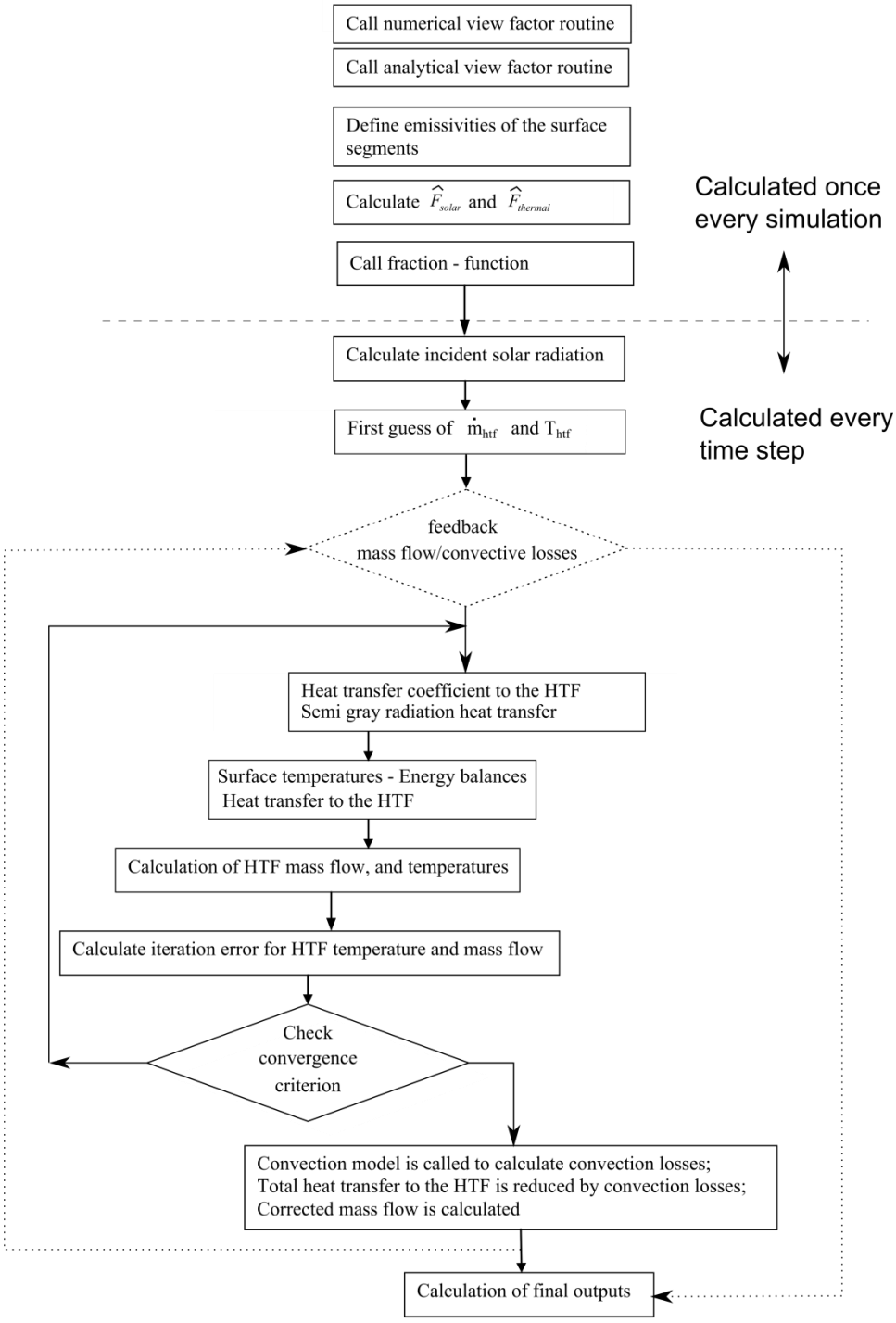

Figure 5.6 – Code Structure Cavity Receiver Model

6 Results

The model presented in this work is used to study the influence of cavity surface emissivity on the performance of the receiver with the described geometry. All results presented are integrated over a simulation time of one year using TMY-data from Blythe, California, USA. To calculate the convection loss the upper bound of natural convection loss, described in Section 4.2.7 is used. Integrated receiver efficiency for annual operation is used as the key measure of overall receiver performance. The receiver efficiency is defined as the ratio of useful HTF energy gain to the total incoming solar radiation to the receiver.

$$\eta = \frac{\int \dot{Q}_{\mathrm{HTF}}\ dt}{\int \dot{Q}_{\mathrm{incident\ solar}}\ dt} \tag{6.1}$$

Heat losses from the cavity are given as a fraction of the incident solar energy, according to Eqn. (6.1).

6.1 Performance of the Cavity Receiver

Table 6.a provides a summary of the receiver performance results for different cavity surface emissivities and the emissivity step wavelength λ_{step} of the two band selective surfaces at 5μm.

ε_{solar}	$\varepsilon_{thermal}$	$\varepsilon_{solar\text{-}passive}$	$\varepsilon_{thermal\text{-}passive}$	Incident solar energy	Efficiency (Energy gain)	Convection loss	Total radiation loss	Solar radiation loss	Thermal radiation loss	Average passive surface temperature
[-]	[-]	[-]	[-]	[TWh]	[%]	[%]	[%]	[%]	[%]	[K]
1	1	1	1	1.13	93.1%	4.5%	2.3%	0.0%	2.3%	664
0.95	0.95	0.95	0.95	1.12	89.8%	5.3%	4.9%	2.4%	2.5%	776
0.95	0.1	0.95	0.1	1.12	90.3%	5.4%	4.3%	2.8%	1.5%	790
0.95	0.1	0.1	0.1	1.12	91.7%	3.7%	4.5%	3.2%	1.3%	553
0.95	0.1	0.1	0.95	1.12	91.8%	3.7%	4.5%	3.1%	1.4%	530
0.85	0.85	0.85	0.85	1.09	83.2%	6.3%	10.5%	7.6%	2.9%	932
0.85	0.1	0.85	0.1	1.09	83.4%	6.6%	10.0%	8.0%	2.0%	968
0.85	0.1	0.1	0.1	1.09	84.8%	4.8%	10.5%	9.1%	1.3%	738
0.85	0.1	0.1	0.85	1.09	85.3%	4.2%	10.5%	9.0%	1.5%	643

Table 6.a - Results table – variation of emissivity distribution – λ_{step}=5μm

The first row represents the theoretical performance for a cavity with black surfaces while the remainder of the table shows results for varying band-emissivities for the active and passive surfaces. Because the performance of the cavity will obviously be driven by the solar emissivity of the active (absorbing) surface, two limits for the performance evaluation were chosen. The high emissivity is 0.95, 0.85 was chosen as the lowest emissivity that is of interest for the technical application of an absorber surface.

The first row of each block shows the performance for the cavity receiver with gray surfaces, where the emissivity is the same for each surface and independent of wavelength. The efficiency of the gray receiver with emissivity 0.95 is about 3% lower than a cavity with black surfaces. The lower efficiency is mostly caused by solar radiation that is not absorbed by the receiver and reflected out of the cavity. The higher average passive surface temperatures indicate higher temperature driven radiation loss from these surfaces with correspondingly higher convective losses. The temperatures of the active surfaces are not given in Table 6.a because of the constant temperature rise of the HTF across the receiver; the average absorber panel temperature varies about 3K over the whole emissivity range. Table 6.a shows that with a high surface solar absorptivity and low surface emissivity in the thermal band, the receiver efficiency increases by 0.5% due to decreased thermal radiation losses. The solar reflective losses increase with lower thermal emissivity because a fraction of the incoming solar radiation occurs in the thermal emissivity band. Figure 6.2 to Figure 6.5 show the distribution of thermal and solar radiation losses from the cavity for gray surfaces (Table 6.a; Row 2) and semi gray surfaces (Table 6.a; Row 3). The sum of the two radiation loss components for each surface represents the total radiation loss from that surface. The radiation loss for any surface is calculated as the radiation that originates from that surface (by either reflection of incoming solar flux or emission) and is incident on the cavity opening either directly or by various reflections at intermediate surfaces. There is no solar radiation from the passive surfaces because all solar radiation that is reflected by these surfaces and is lost through the cavity opening originated from one of the active surfaces; therefore the solar loss is assigned to those surfaces.

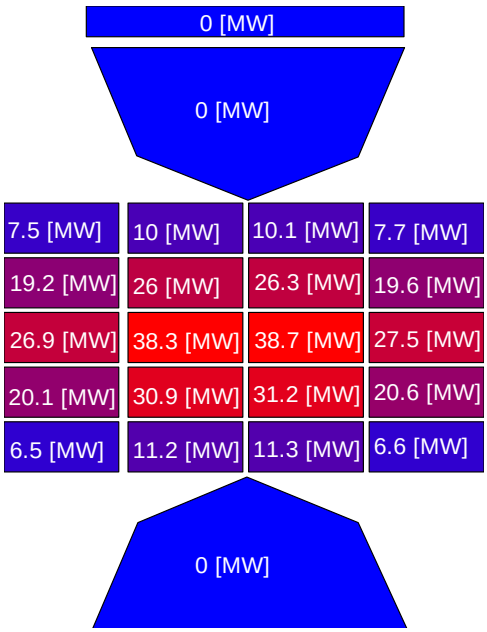

Figure 6.1 - Annual average incident solar radiation on the receiver

Figure 6.3 and Figure 6.5 show that the solar reflective solar loss is concentrated in the center region of the cavity where the distribution of incident solar flux is highest (see Figure 6.1). As expected, lowering the thermal emissivity of the cavity receiver surfaces lowers the thermal losses. Relative to the loss decrease at the active surfaces, the losses from the receiver floor and ceiling decrease less. For the receiver lip an increase in radiation loss is shown.

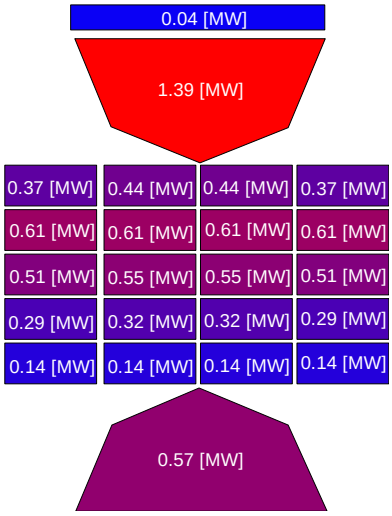

Figure 6.2 - Thermal radiation loss distribution –gray surfaces, $\varepsilon_{solar}=0.95$; $\varepsilon_{thermal}=0.95$; $\varepsilon_{solar\text{-}passive}=0.95$; $\varepsilon_{thermal\text{-}passive}=0.95$

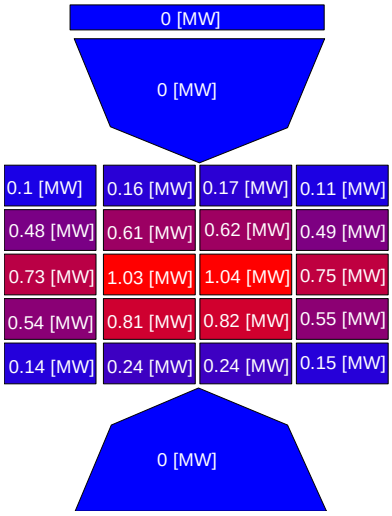

Figure 6.3 - Solar radiation loss distribution gray surfaces, $\varepsilon_{solar}=0.95$; $\varepsilon_{thermal}=0.95$; $\varepsilon_{solar\text{-}passive}=0.95$; $\varepsilon_{thermal\text{-}passive}=0.95$

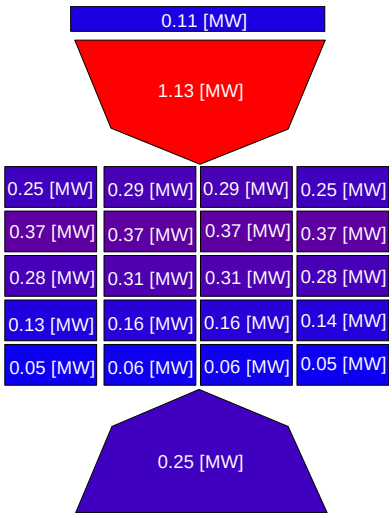

Figure 6.4 - Thermal radiation loss distribution – semi-gray surfaces, $\varepsilon_{solar}=0.95$; $\varepsilon_{thermal}=0.1$; $\varepsilon_{solar\text{-}passive}=0.95$; $\varepsilon_{thermal\text{-}passive}=0.1$

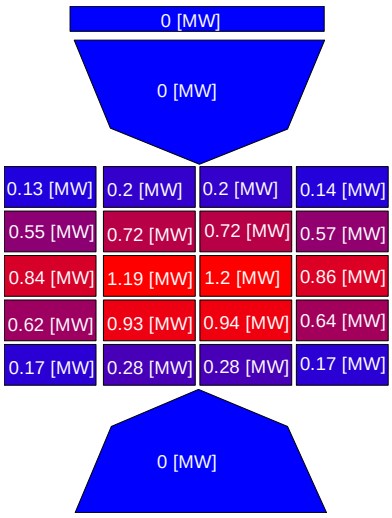

Figure 6.5 - Solar radiation loss distribution gray surfaces, $\varepsilon_{solar}=0.95$; $\varepsilon_{thermal}=0.1$; $\varepsilon_{solar\text{-}passive}=0.95$; $\varepsilon_{thermal\text{-}passive}=0.1$

Figure 6.6 and Figure 6.7 show the total thermal heat loss for all the passive surfaces (floor, ceiling and lip) for an emissivity wavelength step of 5μm and 2μm, respectively. Because the passive surfaces only receive solar radiation by reflection, higher solar reflectivity leads to an increase in indirect solar radiation on the passive surfaces. With higher solar reflectivity of the cavity, the solar absorptivity of the surfaces decreases as well. For the passive surfaces, the decrease in absorbed solar radiation is overpowered by the increase of incident radiation due to reflection; thereby leading to a total increase of heat input to these surfaces. Because the passive surfaces are assumed to be adiabatic, an increase of the heat input leads to an increase in heat loss. Therefore, the thermal heat loss from the passive surfaces is increased for lower solar emissivity.

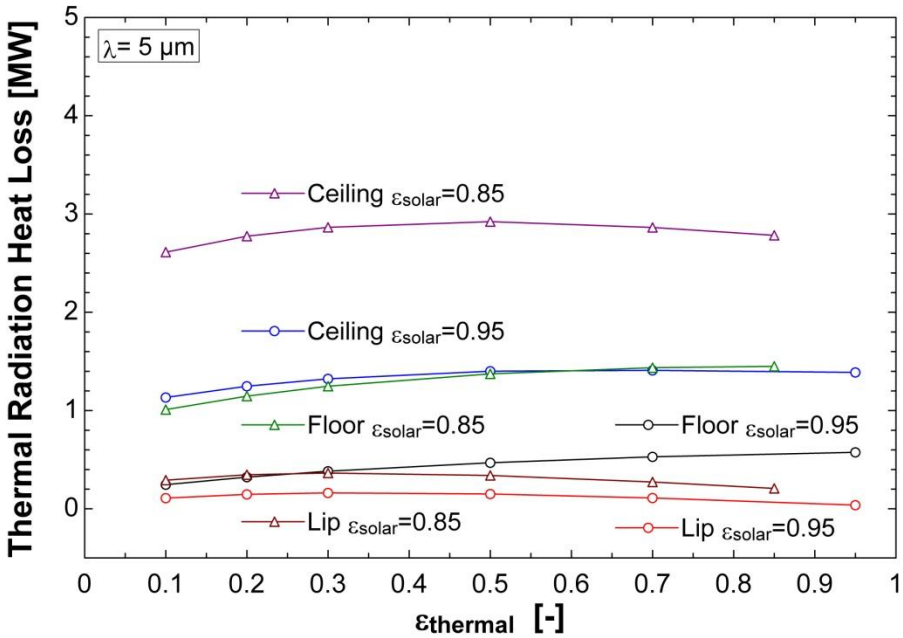

Figure 6.6 - Thermal radiation loss from the passive surfaces as a function of thermal emissivity for different solar emissivities; λ_{step}=5μm.

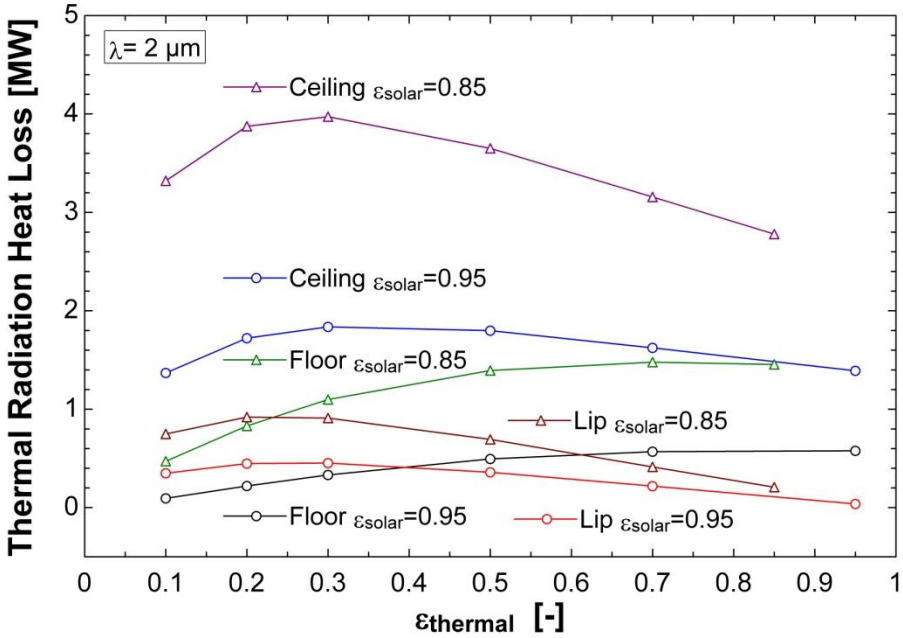

Figure 6.7 - Thermal radiation loss from the passive surfaces as a function of thermal emissivity for different solar emissivities; λ_{step}=2μm.

The same argument can be made for the thermal radiation. While decreasing thermal emissivity decreases losses from the active surfaces, it also increases the thermal reflection inside the cavity. As for the solar reflection, this leads to an increased thermal heat input on the passive surfaces resulting in a heat loss increase with decreasing thermal emissivity. The influence of this effect depends on the overlap of thermal radiation in the solar wavelength band. In situations where the majority of thermal radiation occurs in the thermal emissivity band, changes in thermal emissivity will have a more significant influence on the thermal radiation losses. This is the case for λ_{step} =2μm (Figure 6.7) where only 2-28% of the thermal radiation occurs in the solar emissivity band.

For λ_{step} =5μm (Figure 6.6), 50-83% of the thermal radiation occurs in the solar emissivity band with comparably high emissivity. For this case the majority of the thermal losses are not affected by changes the thermal emissivity. A reallocation of the radiation loss from the passive surfaces can be observed. Because a significant fraction of the thermal radiation loss from the passive surfaces is reflected by the active surfaces before it exits the cavity through the opening (Figure 6.8), the reflection of the intermediate surfaces is an important factor. If a growing majority of the thermal losses occur in the solar emissivity band, with comparably high emissivity, it become less likely that radiation from the passive surfaces is reflected at intermediate surfaces. Instead it will be absorbed and consequently contribute to the thermal losses of the absorbing surface. This effect leads to an apparent decrease in radiation loss from the passive surfaces, but it does not necessarily decrease the total radiation losses of the cavity.

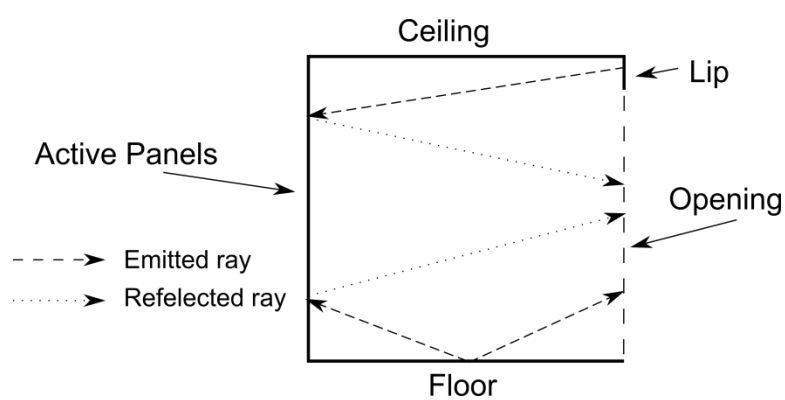

Figure 6.8 - two dimensional vertical sectional view of the cavity receiver, illustrating radiation loss paths from the passive surfaces

These effects are influenced by the temperature of the passive surfaces. The passive surfaces are in thermal equilibrium with the enclosure. For low thermal emissivity a larger temperature

gradient from the passive surfaces to the enclosure is necessary to reach thermal equilibrium, leading to higher surface temperatures.

It is shown in Figure 3.3 that the maximum of emitted thermal radiation shifts to longer wavelength for lower temperatures. The temperatures of the passive surfaces are shown in Figure 6.9 and Figure 6.10 for λ_{step} =5μm and λ_{step} =2μm, respectively. The temperatures are higher for lower solar emissivity because of the increased heat input by reflection of solar radiation to the passive surfaces. The temperature increase with decreasing thermal emissivity is caused by the increasing thermal radiation heat transfer resistance from the passive surfaces. For λ_{step} =5μm the temperature rise with decreasing emissivity is less distinctive because of the significant overlap of thermal radiation in the solar wavelength band.

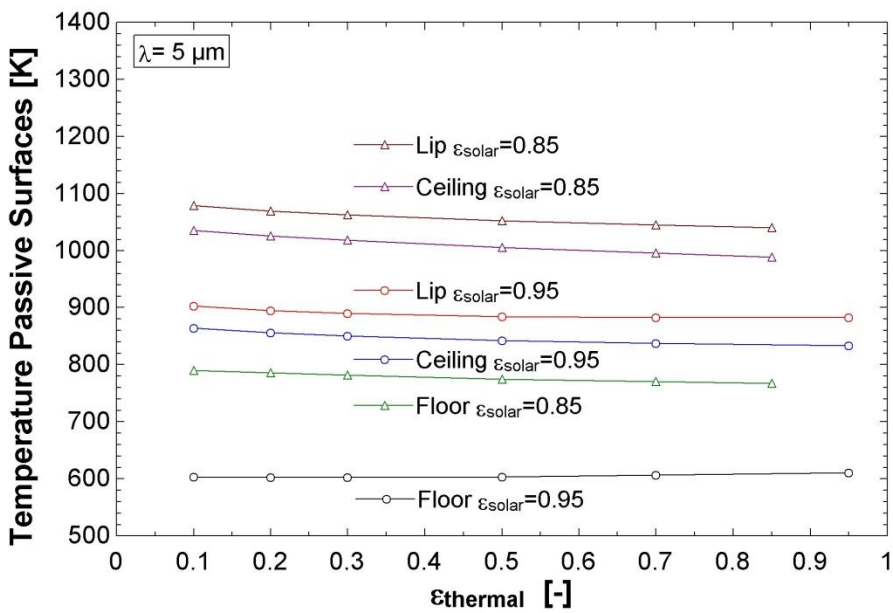

Figure 6.9 – Temperatures of the passive surfaces as a function of thermal emissivity for different solar emissivities; λ_{step}=5μm.

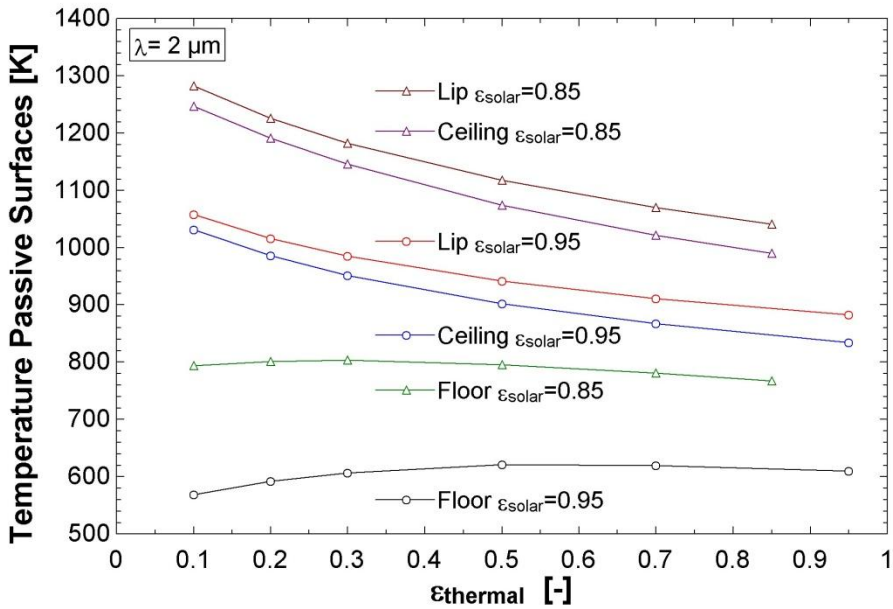

Figure 6.10 - Temperatures of the passive surfaces as a function of thermal emissivity for different solar emissivities; λ_{step}=2μm.

Reallocation of thermal radiation losses from the passive surfaces with increasing difference of thermal- and solar emissivity and a significant overlap of thermal radiation in the solar emissivity band causes the inflection point of thermal losses in Figure 6.7 for λ_{step} =2μm. Also contributing to this effect is the shift of the maximum intensity of thermal radiation with increasing surface temperature towards short wavelength and therefore to the solar emissivity band. Figure 6.6 does not show a distinct inflection point because the thermal losses are decreasing with decreasing thermal emissivity right from the start. For λ_{step} =5μm, there is no initial increase of thermal radiation losses as shown for λ_{step} =2μm because of the high fraction of thermal radiation in the solar emissivity band.

The high solar absorptivity of the passive surfaces lead to a significant heat input and consequently to high surfaces temperatures and high thermal losses. As shown in Figure 6.10, the theoretical temperatures of the passive surfaces reach up to 1300K. Surface temperatures in this magnitude are prohibitive because of material property constraints.

To optimize the receiver efficiency we chose to minimize passive surface temperatures and radiation loss from the passive surfaces. To accomplish this objective, the heat input of the passive surfaces can be reduced by reducing the absorbed solar radiation. The optimal thermal

emissivity of the passive surfaces depends on the convection correlation used and the overall reflectance of the cavity. High thermal emissivity increases the thermal losses from the passive surfaces but decreases the surface temperatures. Depending on the overlap, higher passive surface emissivities also reduce solar losses due to the decreased reflectivity. Lower passive surface temperatures reduce the convective losses and can, depending on the convection correlation, lead to a notably increase in receiver efficiency. Convection correlations that are less dependent on the passive surface temperatures will not lead to a significant loss increase. The decision whether high or low thermal emissivities of the passive are desirable come down to the question if it is more important to minimize thermal radiation losses or to minimize convection loss due to high passive surface temperatures. Because of this strong dependence on the convection correlation, which are source of great uncertainty, we chose to reduce radiation losses in the thermal wavelength band by minimizing the thermal emissivity of all surfaces

In Table 6.a we can see that by reducing the solar emissivity of the passive surfaces the surface temperatures drop by about 200K. Because of the decreased heat input to the passive surfaces, the thermal losses decrease by about 0.3%, as well as the convection losses. Due to the higher solar reflectivity the solar losses increase by 0.4%, leading to a total receiver efficiency increase of 0.2%.

Figure 6.11 and Figure 6.12 show the radiation loss distribution inside the cavity for this emissivity distribution. It can be seen that the radiation losses from the passive surfaces decreased significantly in comparison to Figure 6.2 and Figure 6.4. The thermal and solar radiation losses from the active surfaces however increased leading to a total radiation loss increase of 0.1%. The lower convection losses due to the lower passive surface temperatures lead to the efficiency increase for this emissivity distribution. The passive surface temperatures are shown in Figure 6.13.

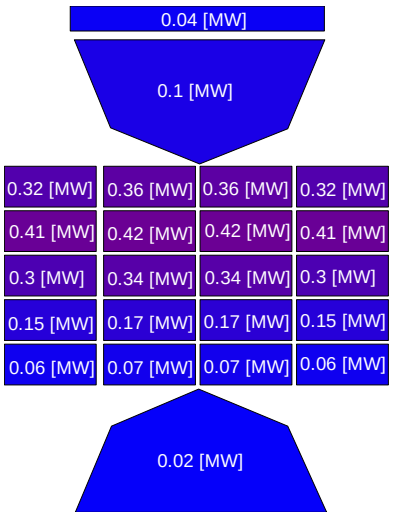

Figure 6.11-Thermal radiation loss distribution gray surfaces $\varepsilon_{solar}=0.95$; $\varepsilon_{thermal}=0.1$; $\varepsilon_{solar\text{-}passive}=0.1$; $\varepsilon_{thermal\text{-}passive}=0.1$

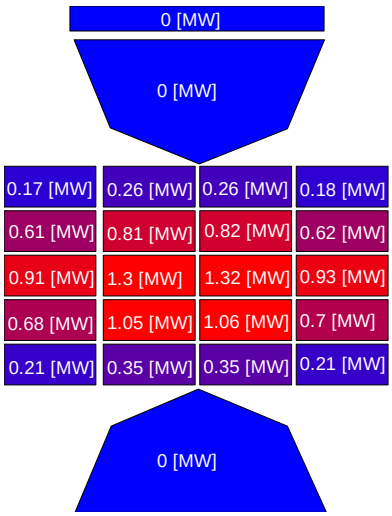

Figure 6.12 - Solar radiation loss distribution gray surfaces, $\varepsilon_{solar}=0.95$; $\varepsilon_{thermal}=0.1$; $\varepsilon_{solar\text{-}passive}=0.1$; $\varepsilon_{thermal\text{-}passive}=0.1$

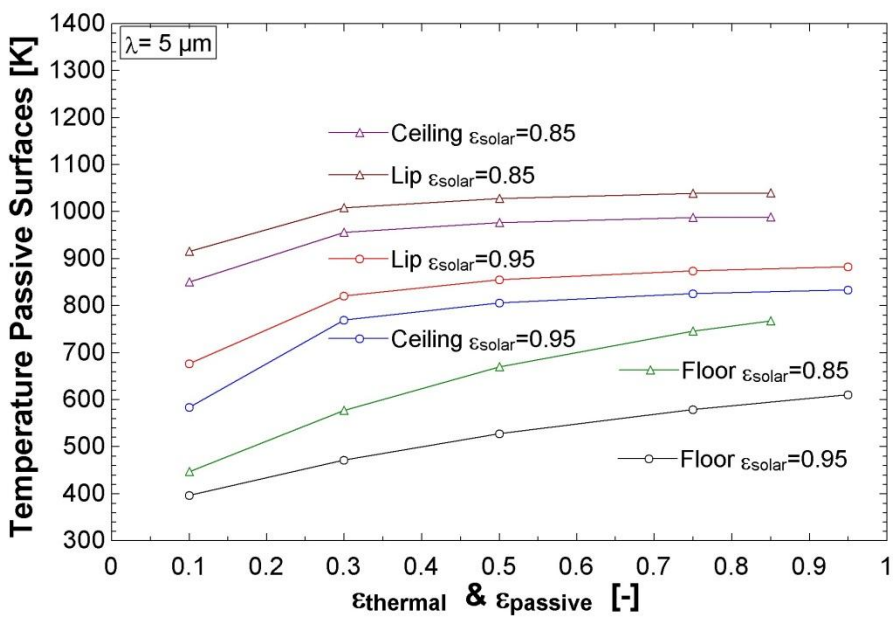

Figure 6.13 – Temperatures of the passive surfaces as a function of thermal emissivity and emissivity of the passive surfaces for different solar emissivities; $\lambda_{step}=5\mu m$.

The significance of the emissivity step wavelength was shown in the discussion of the radiation heat transfer inside the cavity and by the results shown in Figure 6.9 and Figure 6.10.

Reflective passive surfaces are beneficial for the receiver performance. The application of selective surfaces properties for the passive surfaces did not lead to an overall performance increase for the cavity. This can be illustrated by modeling the passive surfaces as gray surfaces with the same emissivity as the active surfaces in the thermal wavelength band. The solar emissivity of the active surfaces is fixed at 0.95 and the thermal emissivity of the active and passive surfaces and the emissivities of the passive surfaces are varied simultaneously. Figure 6.14 shows the overall thermal efficiency of the receiver as a function of emissivity for emissivity steps between 2 and 5 μm. The limiting case that assumes no overlap of the two radiation bands is also included. The no-overlap-line assumes that all solar radiation occurs in the solar emissivity band, accordingly for thermal radiation.

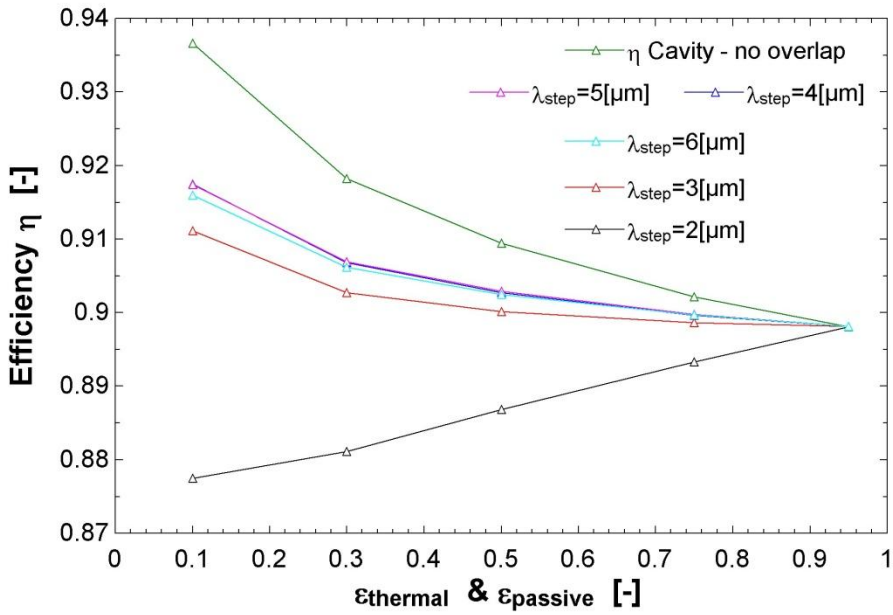

Figure 6.14 - Cavity receiver efficiency as a function of emissivity for different emissivity step wavelengths.

It can be seen in Figure 6.14 that the receiver efficiency increases with decreasing emissivity for λ_{step} around 3μm and larger. The best performance occurs for the hypothetical case in which there is no overlap of the solar and thermal radiation. The efficiency increase becomes smaller as the wavelength of the emissivity step is reduced. For the case with the emissivity step at 2μm, the receiver efficiency decreases with emissivity. In Table 3.a, it is shown that the fraction of solar

radiation that is in the solar emissivity wavelength band decreases, with decreasing emissivity step wavelength. At the same time the fraction of thermal radiation that is in the thermal emissivity wavelength band increases. An optimum step wavelength for a two band surfaces seems to be between 4 and 5μm. In Figure 6.14 it can be seen that the efficiency for an emissivity step wavelength of 4μm is significantly higher than for 3μm. The increase in efficiency at a step of 5μm is almost not noticeable, for 6μm the efficiency is lower.

As stated before, the efficiency of the receiver increases with decreasing emissivity because the losses due to thermal radiation (Figure 6.15) and convection (Figure 6.16) decline. This effect is due to the lower thermal emissivity of the cavity surfaces and the falling surface temperature of the passive surfaces due to the decreasing solar absorptivity of these surfaces.

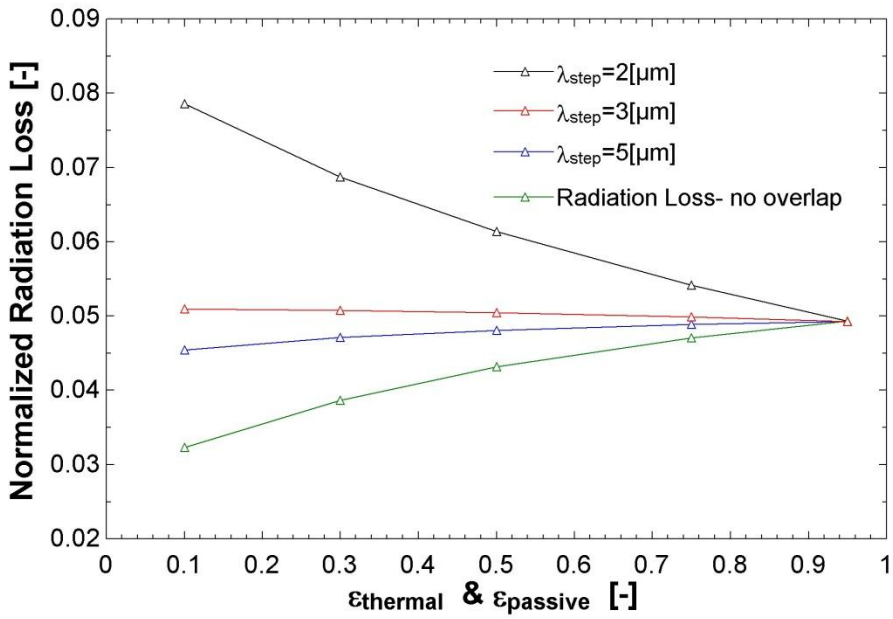

Figure 6.15 - Radiation loss of the cavity as a function of emissivity for different emissivity step wavelengths.

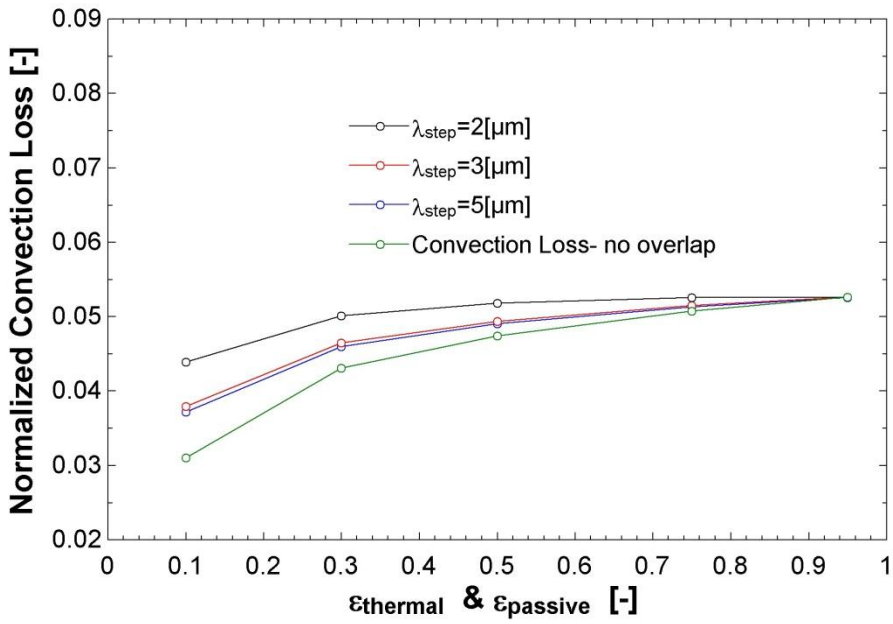

Figure 6.16 - Convection loss of the cavity as a function of emissivity for different emissivity step wavelengths.

With decreasing emissivity step wavelength the fraction of solar radiation in the thermal emissivity band increases, which mainly results in higher solar reflection of the active surfaces, resulting in higher reflective losses. The losses in the solar wavelength band are dominant, increasing solar losses result in decreasing receiver efficiency.

All in all the applied optimizations of the emissivity distribution in the cavity receiver leads to an increase in efficiency of about 0.6-0.7% compared to a gray surface cavity receiver with high emissivity. The efficiency gain is lower for lower solar emissivity of the active surfaces because for these cases more solar radiation is incident on the passive surfaces. The increase solar loss from the passive surfaces has consequently a stronger influence.

6.2 Sensitivity of the Model to the Number of Bands

To study the effect the number of bands has on the results of the model, two surface types with different emissivity distribution characteristics are modeled with a varying number of bands.

The first surface type is a hypothetical two band absorber surface, with high emissivity (0.9-0.95) for short wavelength, an emissivity drop around 3-6 μm and low emissivity (0.2-0.05) for longer wavelength. The emissivity distribution as a function of wavelength is shown in Figure 6.17

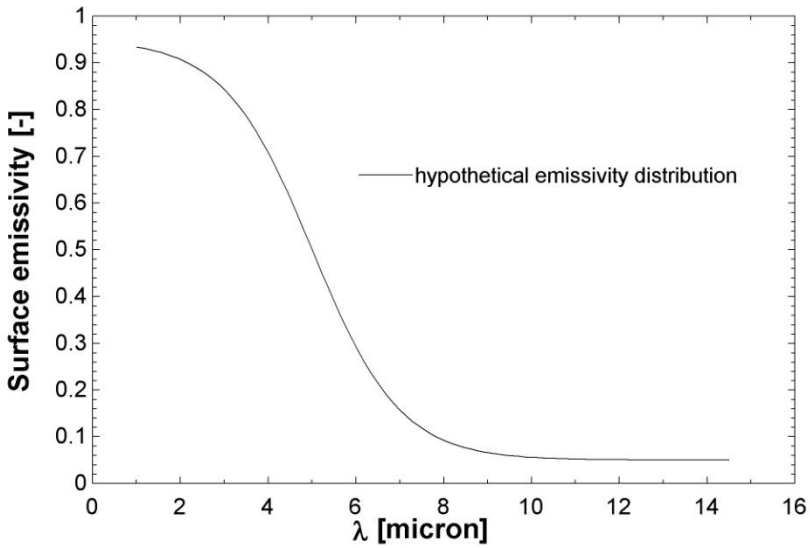

Figure 6.17 – Emissivity distribution of a hypothetical absorber surface

The approximation of this emissivity distribution with 1-7 bands is shown in Figure 6.18 to Figure 6.24. The blue curves represent the emissivity distributions, the green curves the spectral emissive power of solar radiation and the red curves the spectral emissive power of thermal radiation.

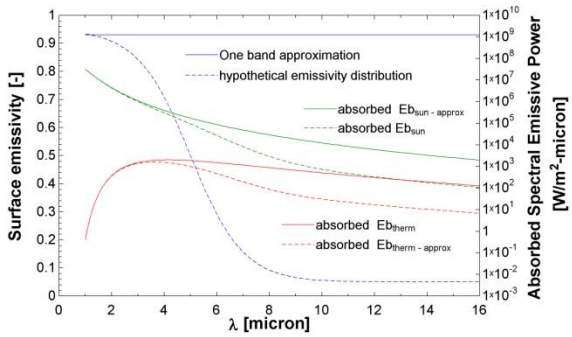

Figure 6.18 - One band approximation, hypothetical surface

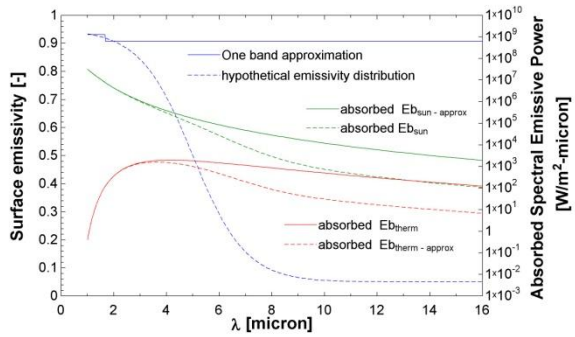

Figure 6.19 - Two band approximation, hypothetical surface

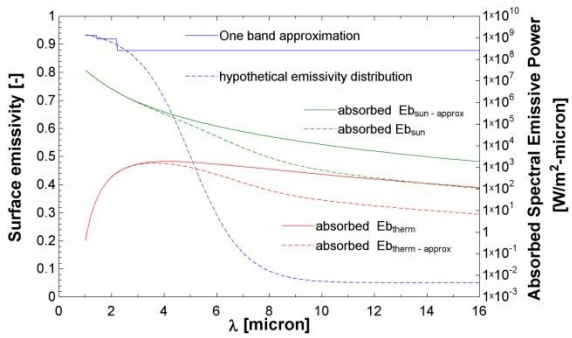

Figure 6.20 - Three band approximation, hypothetical surface

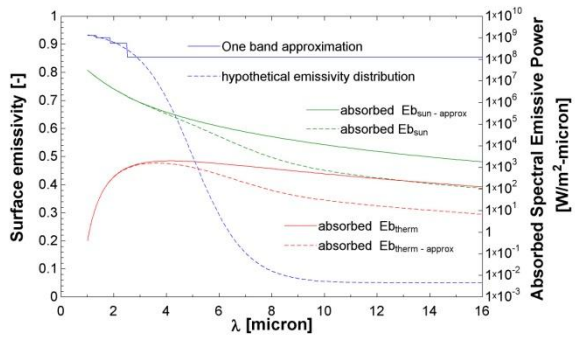

Figure 6.21 - Four band approximation, hypothetical surface

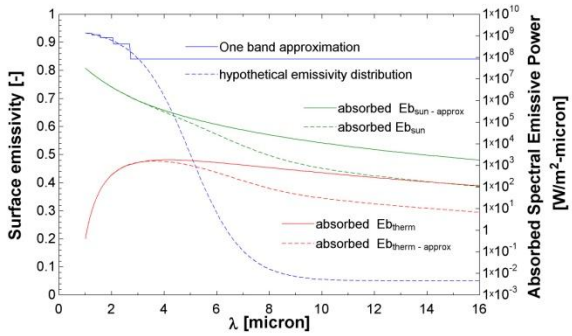

Figure 6.22 - Five band approximation, hypothetical surface

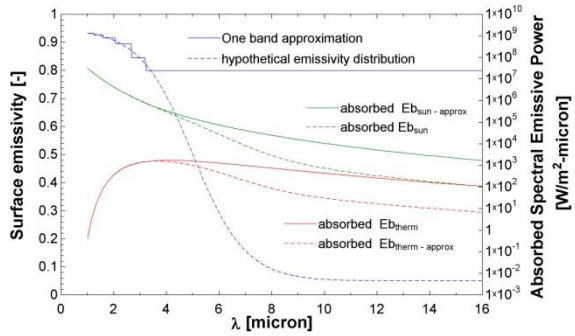

Figure 6.23 - Six band approximation, hypothetical surface

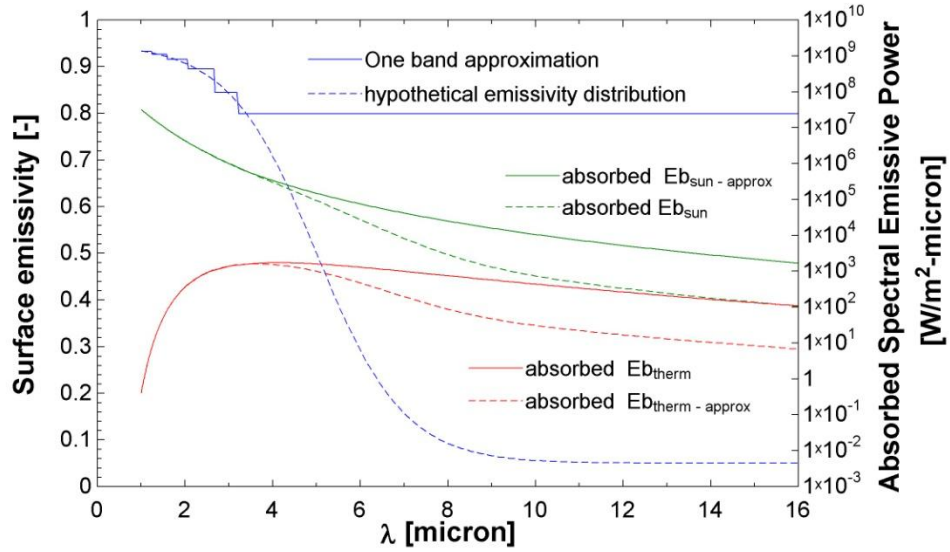

Figure 6.24 - Seven band approximation, hypothetical surface

The emissivities and step wavelengths were chosen in a way that minimizes the difference of absorbed spectral emissive power ($\Delta_{absorbed-E_{b,\lambda}}$) between the original surface and the approximated emissivity distribution. The spectral emissive power of the sun ($E_{b,sun,T=5800K}$) at sun temperature and the spectral emissive power of the cavity surfaces ($E_{b,therm,T=700K}$) at the average surface temperature of 700K are considered. The difference is calculated according to Eqn. (6.2):

$$\Delta_{absorbed-E_{b,\lambda}} = \int_{\lambda=0}^{\lambda_{end}} E_{b,sun,T=5800K} \cdot \left(\varepsilon_{hypo} - \varepsilon_{approx}\right) + \int_{\lambda=0}^{\lambda_{end}} E_{b,therm,T=700K} \cdot \left(\varepsilon_{hypo} - \varepsilon_{approx}\right) \qquad (6.2)$$

The theoretical integration limits are 0 and ∞. Since these limits are not feasible for the calculation process, 180 μm is chosen as the upper integration limit for the hypothetical surface. At this wavelength the spectral emissive power reduced from 10^8 to 10^{-1}; it is reduced to a level where a larger integration range does not lead to significantly different results (Figure 6.25).

The emissivity steps for the band approximations are found using an optimization process in EES (Klein, S.A., 2011) in order to minimize the difference in absorbed spectral emissive power according to Eqn. (6.2). This approach leads to an unexpected result since the band approximations of the surface, in Figure 6.18 to Figure 6.24, do not closely resemble the actual

emissivity distribution of the surface over the full range of wavelengths. Keep in mind that Figure 6.18 to Figure 6.24 only show the significant wavelengths range of 0-16μm, the optimization however was carried out for the wavelength range from 0-180 μm. The emissivity distribution of the hypothetical surface and the spectral emissive powers for the full integration range is shown in Figure 6.25. It can be seen that the intensity of solar and thermal emissive power is largest for wavelength smaller 4 μm and decreasing significantly with increasing wavelength. The peak solar intensity is many orders larger than the thermal emissivity. The band approximation follows the hypothetical emissivity distribution closely for short wavelength for these reasons. The deviation in emissivity for larger wavelengths is not significant because of the low intensity of the spectral emissive power.

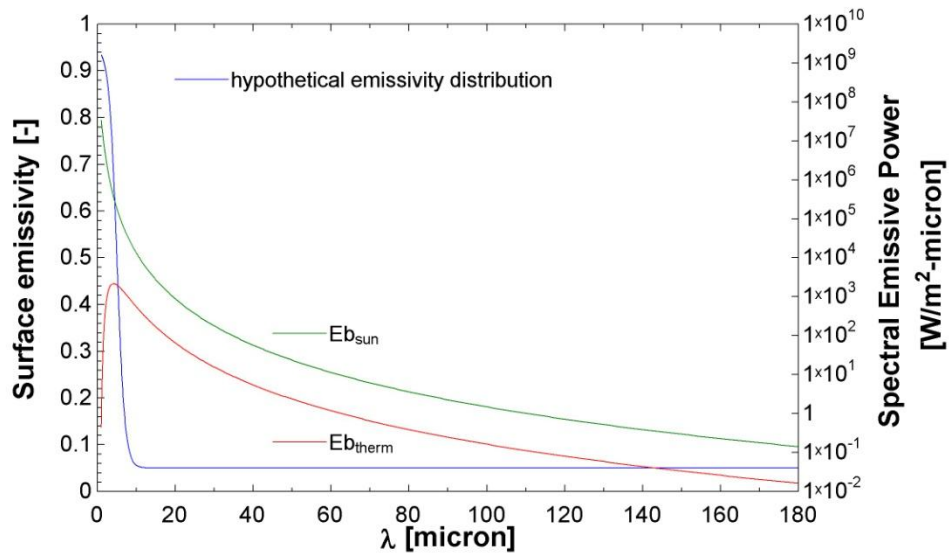

Figure 6.25 - Emissivity distribution of a hypothetical absorber surface and spectral emissive powers for the full integration range.

Figure 6.26 to Figure 6.29**Error! Reference source not found.** show the influence of the number of bands used to approximate the emissivity distribution of the hypothetical absorber surface on the receiver performance. The blue curves show the receiver efficiency for the band approximations shown in Figure 6.18 to Figure 6.24. The red curves show the absolute value of the relative deviation of the efficiency values from the value provided using seven bands. This value, $\Delta_{rel,i}$, is calculated according to Eqn. (6.3).

$$\Delta_{rel,i} = \left| \frac{\eta_i - \eta_{\max}}{\eta_{\max}} \right| \tag{6.3}$$

η is the efficiency, i represents the number of bands and the subscript *max* the maximum number of bands, in this case seven.

Figure 6.26 to Figure 6.29 show the receiver performance resulting from several runs of the same model with the same inputs. It can be seen that results for the receiver efficiency vary by about $5 \cdot 10^{-4}$ from run to run. This variation is most likely caused by the slight variation of the view factors in the model. Some of the view factors are calculated using the Monte Carlo Method, a statistical method that introduces uncertainty to the system.

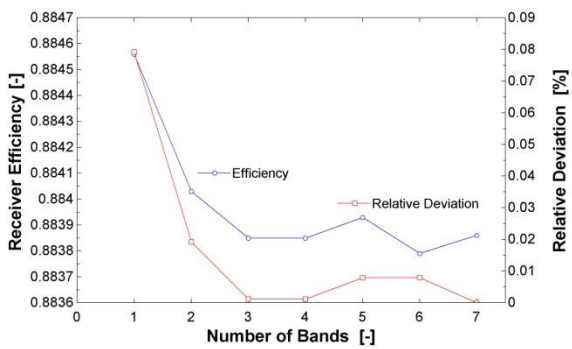

Figure 6.26 - Influence of the number of bands on receiver performance – run #1

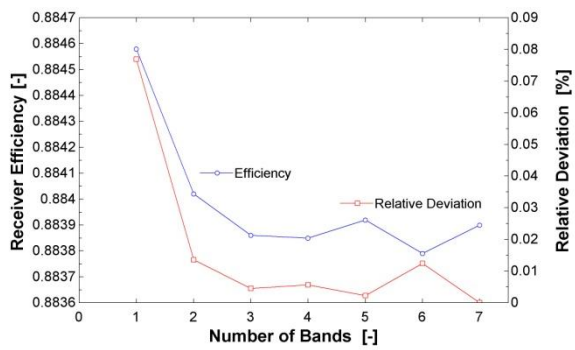

Figure 6.27 - Influence of the number of bands on receiver performance – run #2

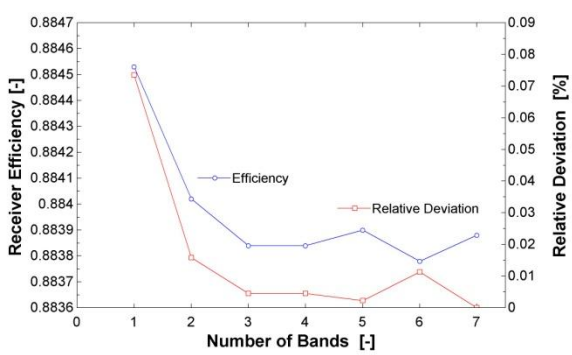

Figure 6.28 - Influence of the number of bands on receiver performance – run #3

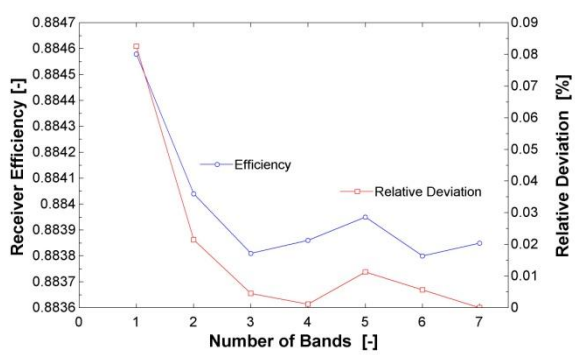

Figure 6.29 - Influence of the number of bands on receiver performance – run #4

Since a higher number of bands leads to a closer approximation of the actual surface properties, it is assumed that the seven band approximation provides the most accurate result of the approximations shown here.

Compared to this value the results using two bands to approximate the surface emissivity leads to better agreement than using one band, the deviation is reduced from 0.08% to 0.03-0.04%. Using three bands reduces the deviation further but not significantly. For higher band numbers the results oscillate around 0.01% deviation which is due to the uncertainty of the model. We can assume that the results do not change significantly for band number larger than 3. For a surface (Tempil, 2012). The use of a two band surface characteristic is the underlying assumption for the studies described in this thesis.

To study the sensitivity to the number of bands for a more complex surface characteristic, emissivity data of the absorber surface coating "Pyromark 2500", distributed by (Tempil, 2012), is used. The emissivity of this surface coating together with the spectral emissive powers as a function of wavelength is given in Figure 6.30. The emissivity varies in a smaller range, between 0.975 and 0.725, in comparison to the hypothetical emissivity distribution in Figure 6.17. Pyromark 2500 surface coating shows a distinct emissivity drop from 2-5 μm but emissivity peaks for higher wavelength are also noticeable.

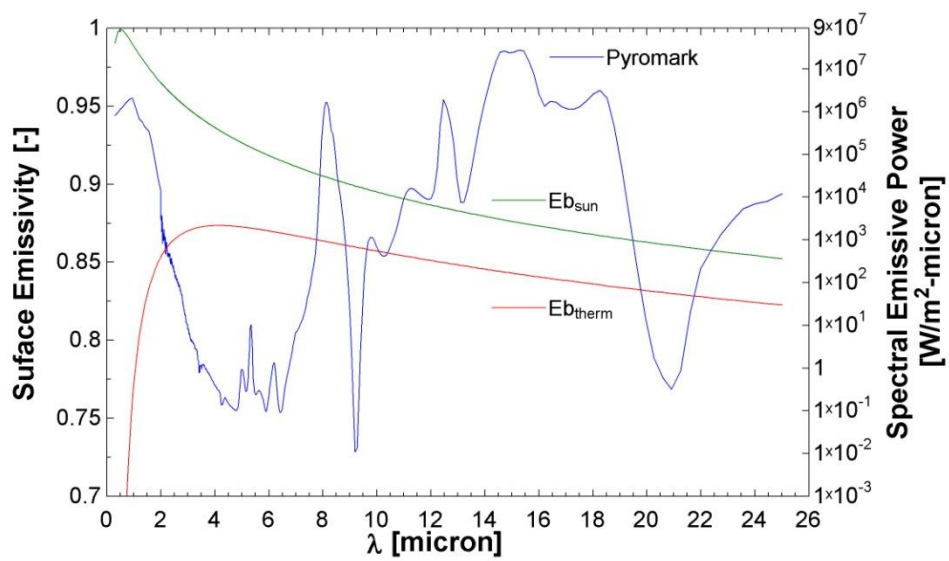

Figure 6.30 - Emissivity of Pyromark 2500 surface coating as a function of wavelength, (Tempil, 2012)

The green and red line in Figure 6.30 represent the solar and thermal spectral emissive power that interact with the surface. Four approaches with one, two, five and ten band are done to approximate the real emissivity distribution, shown in Figure 6.31 to Figure 6.34.

It can be seen in Figure 6.30 that the majority of the spectral emissive power occurs in wavelength between 0 – 4 μm. The goal of the band approximation is to model the absorption characteristic of a surface and not the emissivity distribution. This is the reason why additional bands are used to match the emissivity distribution of the surface in between wavelength 0 – 4 μm more closely, since the spectral emissive power is largest in this range.

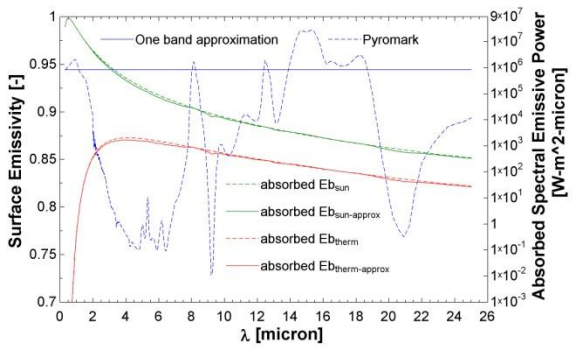

Figure 6.31 – One band approximation

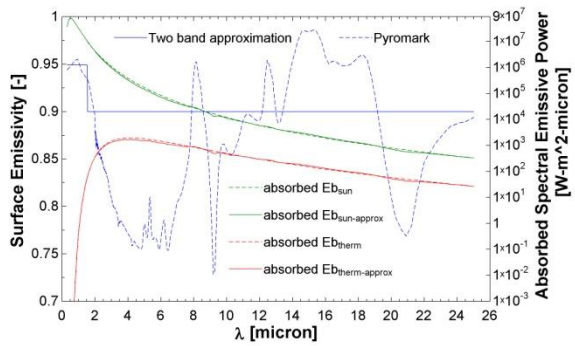

Figure 6.32 - Two band approximation

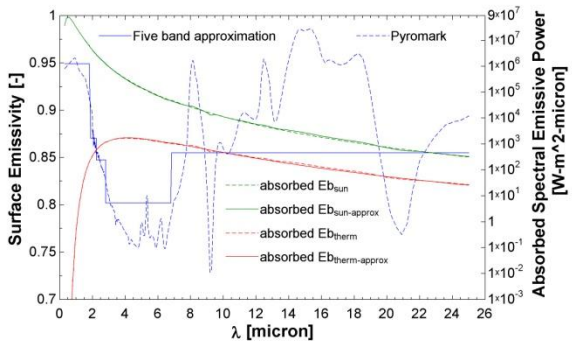

Figure 6.33 – Five band approximation

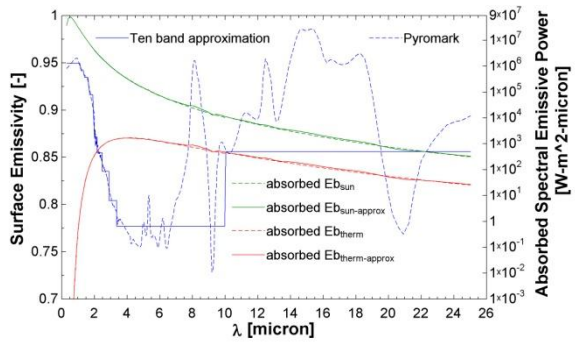

Figure 6.34 - Ten band approximation

As it was done for the hypothetical emissivity distribution, the change of receiver efficiency with number of bands is used as a measure to determine how many bands are necessary to model the surface emissivity. In Figure 6.35 this is shown.

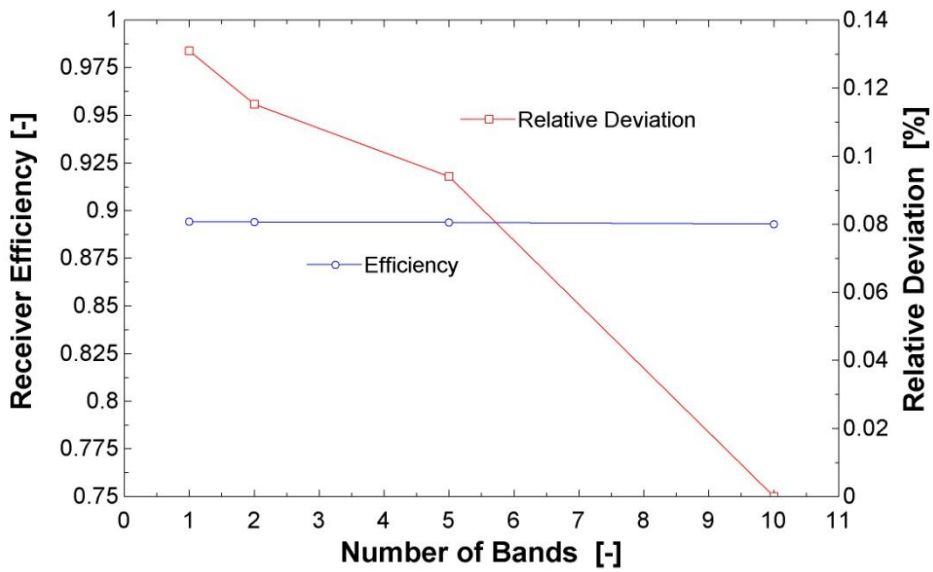

Figure 6.35 - Influence of the number of bands on receiver performance; Pyromark 2500

It can be seen, that the receiver efficiency does not change significantly with the number of bands. The relative deviation between the efficiency obtained assuming gray surfaces (one band) and the efficiency determined with 10 bands is about 1.2%. This suggests that the gray surface assumption is a useful approximation for modeling Pyromark 2500 surface coating and surfaces with similar characteristics.

The use of more bands does not lead to a significant change in receiver efficiency because the emissivity only varies over a range of 0.2. In the previous example of the hypothetical surface emissivity distribution the emissivity step between each significant band was larger.

The number of bands that are supported by the SAM model is limited due to way it was implemented. Since a large number of bands does not influence the results of the significantly, it is concluded that twenty is an appropriate upper limit of the number of bands to approximate an absorber surface for central receiver with sufficient accuracy. If necessary this number can be easily modified to support more bands.

6.3 Comparison of the Convection Correlations

The convection correlations by (Siebers, D. and Kraabel, J., 1984) are presented in Section 4.2.3. A significant finding of their studies is that the natural convection losses of large cavities are similar to that of flat plates. With the goal to develop a model that provides a realistic upper bound of natural convection loss from a cavity receiver, we modeled the cavity as a combination of semi-infinite flat plates. The underlying assumption was that the restriction of free flow along the surfaces in a cavity leads to lower convective losses than expected for the unrestricted flow along independent flat plates. Natural convection correlations for vertical and horizontal up- and down facing plates, respectively, were used. This correlation is described in Section 4.2.6. Surprisingly, the result of this approach is an overall convection coefficient of the cavity that is lower than the one predicted by available models for cavity receivers (Figure 6.36). Studies of smaller cavity receivers (Leibfried, U. and Orthjohan, J., 1995), Section 4.2.5, observe flow patterns inside the cavity caused by buoyancy differences that resemble forced convection-like heat transfer situations. This effect may cause the convection losses of the cavity to be larger than for independent flat plates. To account for the forced convection heat transfer driven by a flow that is caused by natural convection effects, the model of independent flat plates can be extended. Instead of simply relying on natural convection correlations for flat plates, forced convection correlations with turbulent flow parallel to the surface are used to find an upper bound of the natural convection loss of the cavity receiver (Section 4.2.7). In this case, the flow velocity is assumed to be the average characteristic velocity for natural convection.

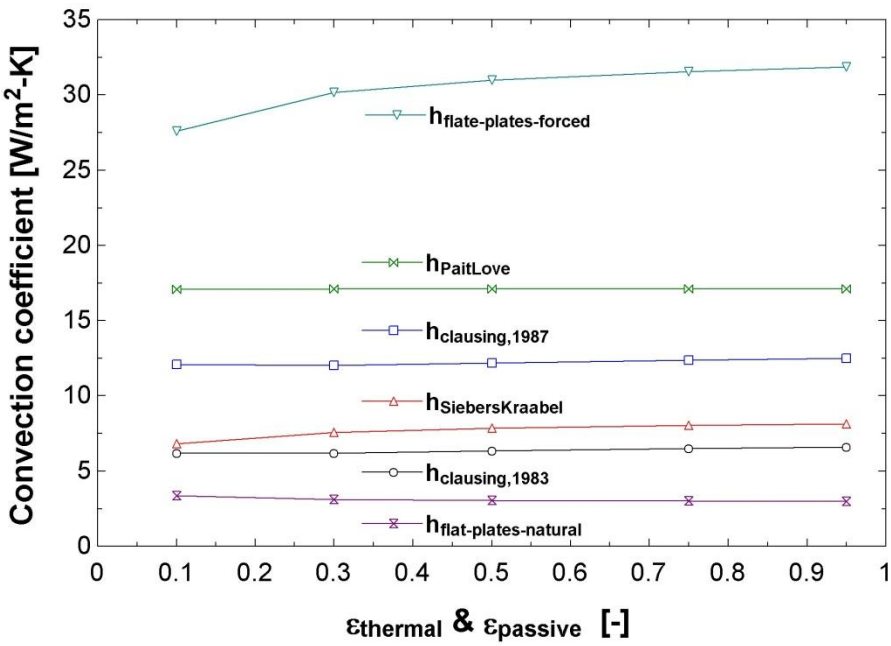

Figure 6.36 - Overall convection loss coefficient in respect of emissivity. Solar emissivity of the active surfaces is 0.95, all other emissivity vary with $\varepsilon_{thermal}$; λ_{step}=5μm.

The overall convection loss coefficient of the cavity is shown in Figure 6.36 for different cavity convection correlations and for our two independent flat plates models as a function of surface emissivity. The optimum radiative surface properties found in Section 6.1 are used for the calculations. The passive surface are defined to be gray surfaces, the emissivity varies together with the thermal emissivity of the active surfaces. The solar emissivity of the active surfaces is set to a high value, here 0.95. The emissivity step between the two bands occurs at 5 µm. The overall convection loss coefficient of the cavity is defined in Eqn.(4.38) as:

$$h_{cavity} = \frac{\dot{Q}_{convection}}{\left(T_{wall} - T_{bulk}\right) \cdot A_{cavity}} \tag{4.38}$$

As stated before in Section 4.2.7, the wall temperature is calculated as an area averaged temperature of the cavity surfaces according to Eqn. (4.43)

$$T_{wall} = \frac{\sum_{i=1}^{4N+4} T_{s,i} \cdot A_i}{\sum_{i=1}^{4N+4} A_i} \tag{4.43}$$

The bulk temperature is calculated using the energy balance in (Clausing, 1983), Section 4.2.1. In Figure 6.36 it can be seen that the established large cavity correlations by(Clausing, 1983), (Clausing, 1987) and (Siebers, D. and Kraabel, J., 1984) are in a range of 5-12 W/m^2-K. The correlation for smaller cavities, typically used in solar dish applications, by (Paitoonsurikarn, S. and Lovegrove K., 2006) provides a convection coefficient of about 17 W/m^2-K. Calculating the overall natural convection coefficient of the cavity as a combination of independent natural convection from flat plates leads to a lower bound of about 3 W/m^2-K. The approach of modeling the overall cavity natural convection coefficient of the cavity using forced convection correlations for a set of independent flat plates results in an upper bound of convection loss of 25-33 W/m^2-K.

6.3.1 Behavior and Characteristics of the Correlations

It can be seen in Figure 6.36 that the convection coefficients determined using natural convection correlations (except the Siebers and Kraabel correlation) are approximately independent of emissivity, while the correlation using forced convection decreases with decreasing emissivity. The emissivity primarily influences the temperature of the passive surfaces. The temperature of the active surface is approximately constant with respect to emissivity. This is attributable to the fact that changes in the absorbed radiation are compensated by reducing or increasing the mass flow rate of the HTF to obtain a constant HTF outlet temperature.

As the emissivity of the passive surfaces is decreased, less radiation is absorbed on the passive surfaces and the passive surface temperatures decrease. Changes in the passive surface temperatures have an influence on the average cavity surface temperature, which is used to determine the film temperature for the purpose of evaluation of the fluid properties and determining the overall driving temperature difference in the calculation of the convection heat transfer coefficient.

The natural convection correlations in this study all depend on the Grashof number (*Gr*) and Prandtl number (*Pr*).

$$Gr = g \cdot \beta \cdot \frac{\rho^2}{\mu^2} \cdot \left(T_{wall} - T_{amb}\right) \cdot L^3 \tag{6.4}$$

$$\mathrm{Pr} = \frac{cp \cdot \mu}{k} \tag{6.5}$$

With lower film temperature, the fluid property term $\beta \cdot \rho^2 / \mu^2$ increases and the temperature difference $\left(T_{wall} - T_{amb}\right)$ decreases, resulting in an overall increase of the Grashof number. Together with the increasing Prandtl number with decreasing average wall temperature these effects lead to a higher Nusselt number (*Nu*).

$$Nu = \frac{h \cdot L}{k} \tag{6.6}$$

For the natural convection correlations where the properties are evaluated at the film temperature, the lower conductivity k for lower temperatures leads to an insignificantly small change in heat transfer coefficient h despite the higher Nusselt number.

The correlations from (Siebers, D. and Kraabel, J., 1984) and the developed model using forced convection correlations of flat plates show significant decrease of the heat transfer coefficient with decreasing average wall temperature. These correlations determine the fluid properties at the ambient or bulk temperature, which is essentially independent of receiver emissivity.

Considering Eqn. (6.4), a lower average wall temperature with constant fluid properties leads to a lower Grashof number resulting in lower Nusselt numbers and lower corresponding heat transfer coefficients.

An additional effect can be observed for the forced convection correlation, which causes a higher sensitivity to the temperature of the passive surfaces than for the natural convection correlations. The higher sensitivity is caused by the different distribution of convection loss inside the cavity. Using the natural convection correlation, the convection loss from the active surfaces is responsible for about 80-90% of the total convection loss of the cavity. Because the forced convection is driven by an external flow, the convective loss is not dependent on the orientation

of the surfaces. The heat loss is now mostly temperature driven, resulting in a loss contribution of the active surfaces of about 50-70% and correspondingly higher losses from the passive surfaces. The higher contribution to the total convection loss of the passive surfaces causes an increasing convection loss for decreasing emissivities.

6.3.2 Influence of the Correlations on the Receiver Model

In this section, the influence of the different convection correlations on the overall receiver performance is shown. The coupled convection implementation method described in Section 5.3.2 is used. For this implementation method, the convection correlations are used to determine the overall convection loss of the cavity receiver. To be able to couple the convection losses with the surfaces temperatures, a convection loss for each surface segment has to be known. As the Clausing correlation from 1983 is the only established correlation that provides this information, the convection loss distribution provided by this correlation is used. To obtain the same overall convective heat loss that is predicted by one of the more recent models shown in Figure 6.36, the Clausing correlation from 1983 is scaled accordingly.

$$f_{scale} = \frac{\dot{Q}_{convection-loss}\left(correlation\ i\right)}{\dot{Q}_{convection-loss}\left(Clausing\ 1983\right)} \tag{5.22}$$

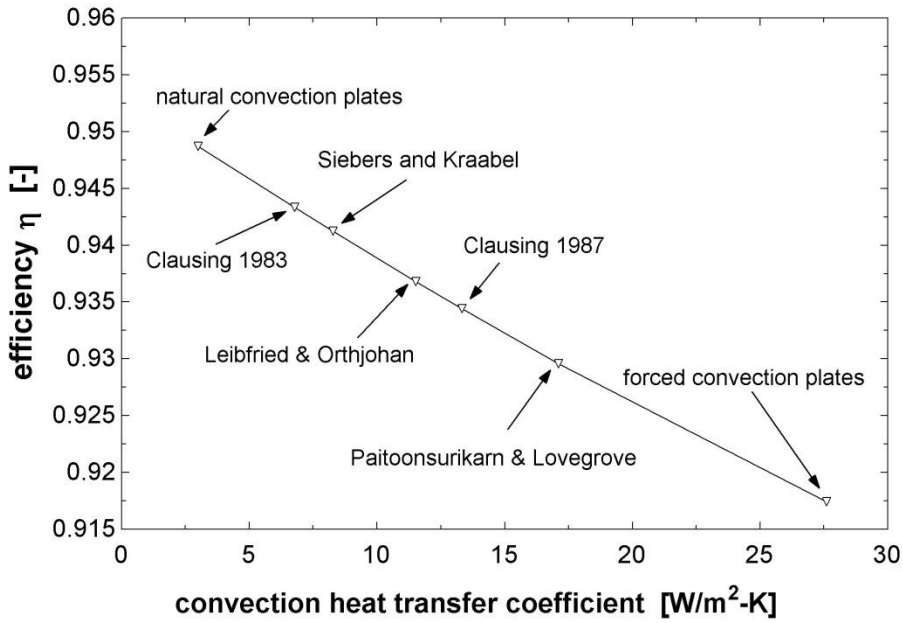

Figure 6.37 - Cavity efficiency for different convection correlations with $\varepsilon_{solar,active}$ = 0.95 and $\varepsilon_{solar,passive}$. = $\varepsilon_{thermal}$=0.1

The effect of the different magnitudes of convective loss on the cavity efficiency is given in Figure 6.37. Because the different convection correlations are just used to scale the convection loss but do not affect the convection loss distribution inside the cavity the efficiency decreases linearly with increasing convection loss. Increasing the convection coefficient by about 18 W/m^2-K from the Clausing 1983 correlation to our estimated upper bound reduces the receiver efficiency by approximately 2.5%. In Figure 6.38Figure 6.38 the total radiation loss of the cavity and the convection loss as a function of overall convection coefficient are shown. While the convection loss increases linearly with the convection coefficient the radiation loss decreases only slightly. The temperature decrease caused by increased convection is comparably small and does not reduce the radiation losses significantly.

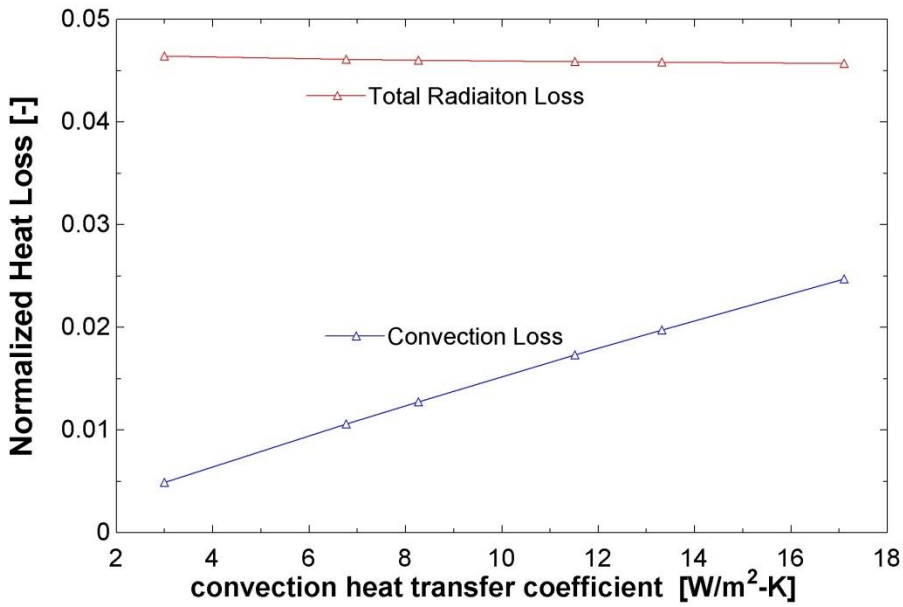

Figure 6.38 – Heat losses normalized by incident solar radiation for different convection correlations

6.3.3 Influence of the Forced Convection

The way wind induced forced convection is approximated is described in Section 4.3. Figure 6.39 show the convective heat transfer coefficients of the natural convection correlation, and the increase of coefficient when mixed convection is considered using either the original (Siebers, D. and Kraabel, J., 1984) approach or the extension that considers wind direction. It can be seen that the increase of the convective heat transfer coefficient is approximately constant for the different natural convection correlations. Slight differences are due to the different surface temperatures of the cavity. Lower overall convection coefficients lead to higher cavity surface temperatures, therefore higher film temperatures influence the fluid properties which are the driving influence to determine the forced heat transfer coefficient, Eqn.(4.44)

$$Nu_{forced} = 0.287 \cdot \mathrm{Re}_w^{0.8} \cdot \mathrm{Pr}^{1/3} \tag{4.44}$$

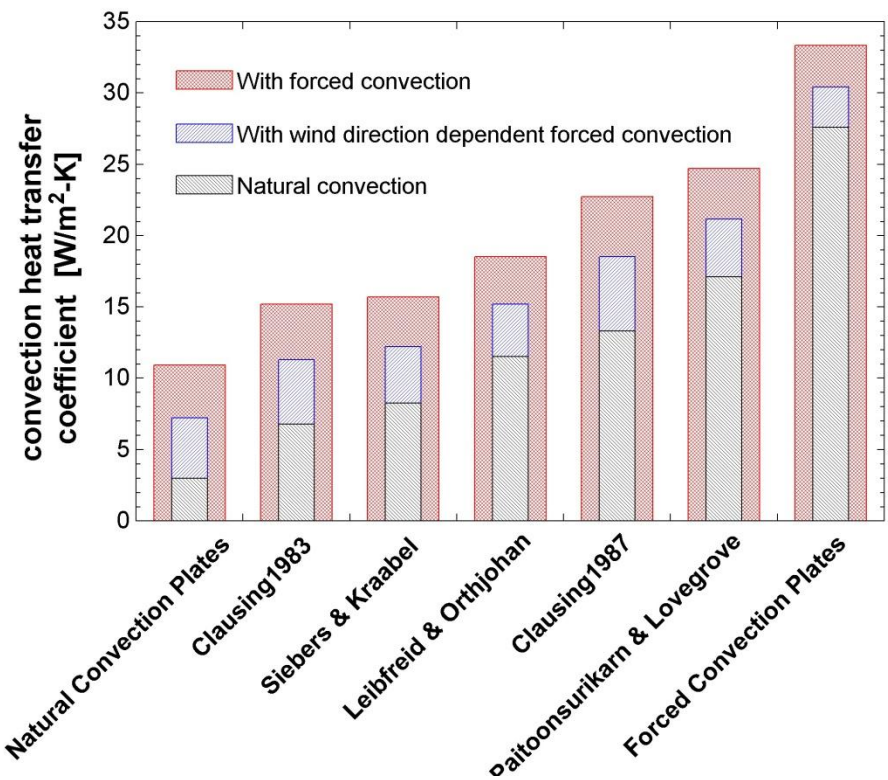

Figure 6.39 – Convective heat transfer coefficients of the natural convection correlation, including the implementation methods of forced convection

Figure 6.40 shows the effect the forced convection approximation has on the overall receiver efficiency. The original (Siebers, D. and Kraabel, J., 1984) approach leads to a reduction in annual receiver efficiency of 0.5-1%. The wind direction dependent model predicts lower efficiency reductions of about 0.1-0.6%. Here the beneficial effect that the cavity shades the internal receiver surfaces from direct wind to reduce forced convection losses is approximated.

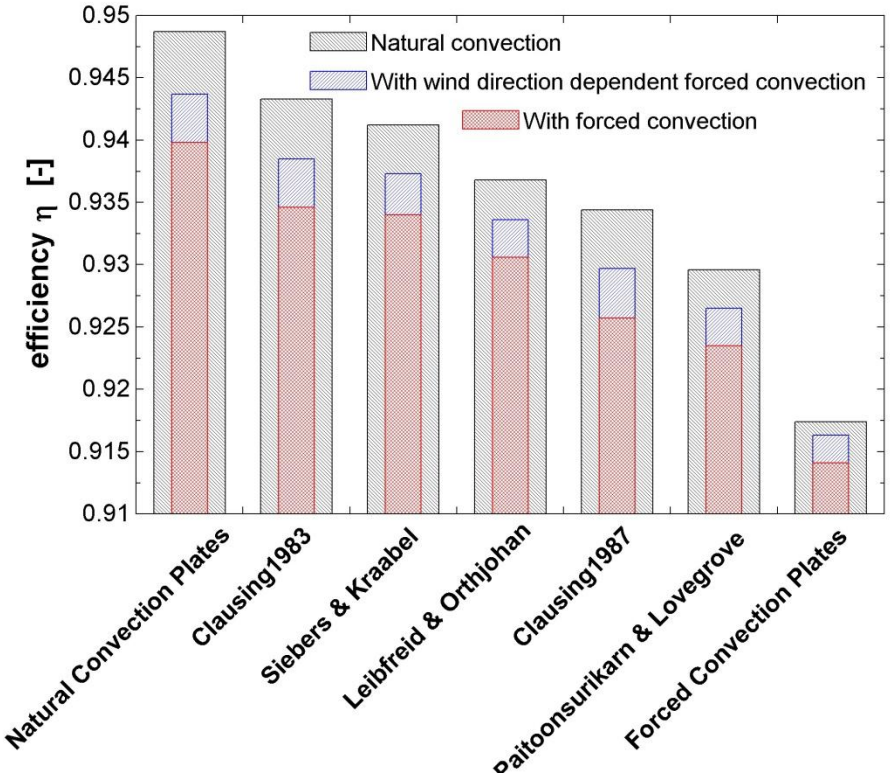

Figure 6.40– Receiver efficiency for the different natural convection correlation, including the implementation methods of forced convection

6.4 Comparison Cavity vs. External Receiver

Of great interest for the development of solar tower receivers is the performance characteristic of different receiver geometries. With the completed cavity receiver model and the external cylindrical receiver in SAM, both models can be used for performance comparison in respect to various parameters. With the developed extension of the cavity receiver model and the implementation of these modifications in the external cylindrical receiver model, the influence of selective surfaces on the performance of the two receiver types will be shown here.

6.4.1 External Receiver Model – Implementation of Semi-Gray Surfaces

The model of the external receiver for a solar tower in SAM was developed by (Wagner, 2008), detailed information about the model can be found in his Master's Thesis. The existing external receiver model in SAM considers gray surfaces; to put the two models on the same basis of comparison the semi-gray radiation model is implemented. The basic structure is similar to that of the cavity receiver model described in Section 5.3.3. The surface temperatures are calculated by solving the energy balance similarly to Eqn.(5.27). Radiation heat transfer is considered using a radiation heat transfer coefficient as it was done in the cavity receiver model.

The radiation heat transfer situation of the external receiver is less complex than for the cavity receiver because no interaction between the absorber surfaces has to be considered. All radiation that is emitted or reflected by the receiver surfaces contribute to the heat loss of the receiver. The external receiver radiation model separates thermal radiation loss along the horizon line. It assumes that half of the irradiated radiation is incident on the area below the horizon line resulting in thermal radiation heat exchange with the ground/ambient at ambient temperature. The other half is incident on the heat transfer surface above the horizon line at sky temperature. Both temperatures are given by TRNSYS depending on hourly weather data.

$$\dot{Q}_{therm,i} = \dot{Q}_{therm,i,amb} + \dot{Q}_{therm,i,sky} \tag{6.7}$$

The radiation heat transfer equation can be derived from the more complex model developed for the cavity receiver in Eqn. (3.43), j represent any of the receiver surfaces and the two interacting heat transfer surfaces *ambient* and *sky* with any of the receiver surfaces i .

$$\dot{Q}_{therm,i,j} = \sigma \cdot \varepsilon_{therm,i} \cdot \varepsilon_{therm,j} \cdot A_i \cdot \hat{F}_{therm,i,j} \cdot \left[\left(1 - f_{0-\lambda_{step},T_{s,i}}\right) \cdot T_{s,i}^4 - \left(1 - f_{0-\lambda_{step},T_{s,j}}\right) \cdot T_{s,j}^4 \right]$$
$$+ \sigma \cdot \varepsilon_{solar,i} \cdot \varepsilon_{solar,j} \cdot A_i \cdot \hat{F}_{solar,i,j} \cdot \left[f_{0-\lambda_{step},T_{s,i}} \cdot T_{s,i}^4 - f_{0-\lambda_{step},T_{s,j}} \cdot T_{s,j}^4 \right]$$

(3.43)

It is assumed that all radiation that leaves a receiver surfaces is gets either absorbed by the *ambient* or the *sky*, the corresponding emissivities are unity. It is further assumed that half of the radiation leaving each receiver surfaces is incident on the ground (ambient), the other half is incident on the sky; the corresponding $\hat{F}$ values are half. The receiver surfaces don't see each other and therefore do not exchange radiation; all $\hat{F}$ values between the receiver surfaces are zero. For any value of *j* representing a receiver surfaces, Eqn. (3.43) results in no radiation heat transfer. For j representing the ground at ambient condition the equation can be stated as:

$$\dot{Q}_{therm,i,amb} = \sigma \cdot \varepsilon_{therm,i} \cdot A_i \cdot \frac{1}{2} \cdot \left[\left(1 - f_{0-\lambda_{step},T_{s,i}}\right) \cdot T_{s,i}^4 - \left(1 - f_{0-\lambda_{step},T_{amb}}\right) \cdot T_{amb}^4 \right]$$
$$+ \sigma \cdot \varepsilon_{solar,i} \cdot A_i \cdot \frac{1}{2} \cdot \left[f_{0-\lambda_{step},T_{s,i}} \cdot T_{s,i}^4 - f_{0-\lambda_{step},T_{amb}} \cdot T_{amb}^4 \right] \quad (6.8)$$

Accordingly the thermal radiation heat transfer between the receiver surfaces and the sky can be stated. To be able to solve for the surface temperatures of the receiver the radiation heat transfer is expressed as a heat transfer coefficient according to Eqn. (5.30) and (5.31).

$$h_{rad,amb,i} = \frac{1}{2} \cdot \frac{\sigma}{T_{s,i} - T_{amb}} \cdot \left(\begin{array}{l} \varepsilon_{therm,i} \cdot \left[\left(1 - f_{0-\lambda_{step},T_{s,i}}\right) \cdot T_{s,i}^4 - \left(1 - f_{0-\lambda_{step},T_{amb}}\right) \cdot T_{amb}^4 \right] \\ + \varepsilon_{solar,i} \cdot \left[f_{0-\lambda_{step},T_{s,i}} \cdot T_{s,i}^4 - f_{0-\lambda_{step},T_{amb}} \cdot T_{amb}^4 \right] \end{array} \right) \quad (6.9)$$

$$h_{rad,sky,i} = \frac{1}{2} \frac{\sigma}{T_{s,i} - T_{sky}} \cdot \left(\begin{array}{l} \varepsilon_{therm,i} \cdot \left[\left(1 - f_{0-\lambda_{step},T_{s,i}}\right) \cdot T_{s,i}^4 - \left(1 - f_{0-\lambda_{step},T_{sky}}\right) \cdot T_{sky}^4 \right] \\ + \varepsilon_{solar,i} \cdot \left[\left(f_{0-\lambda_{step},T_{s,i}}\right) \cdot T_{s,i}^4 - \left(f_{0-\lambda_{step},T_{sky}}\right) \cdot T_{sky}^4 \right] \end{array} \right) \quad (6.10)$$

The total thermal radiation transfer from the receiver surfaces to ambient and sky can be expressed in terms of heat transfer coefficients as:

$$\dot{Q}_{therm} = \sum_{i=1}^{surface\ number} h_{rad,amb,i} \cdot A_i \cdot \left(T_{s,i} - T_{amb}\right) + h_{rad,sky,i} \cdot A_i \cdot \left(T_{s,i} - T_{sky}\right) \tag{6.11}$$

The reflective solar loss of the external receiver can be expressed as the reflected solar radiation distributed over the two emissivity bands:

$$\dot{Q}_{solar} = \underbrace{f_{0-\lambda_{step},T_{sun}} \cdot \left(1-\varepsilon_{solar}\right) \cdot \dot{Q}_{incident-solar}}_{\text{reflective solar loss in the solar emissivity band}} + \underbrace{\left(1-f_{0-\lambda_{step},T_{sun}}\right) \cdot \left(1-\varepsilon_{therm}\right) \cdot \dot{Q}_{incident-solar}}_{\text{reflective solar loss in the thermal emissivity band}} \tag{6.12}$$

6.4.2 Comparison Cavity vs. External Receiver

For comparison, SAM is used to obtain the optimum plant design for each receiver type. Both types are designed to have a net electric output at the design point of 100 MWe. Given the same power block design, this results in the same design receiver thermal power of 514.1 MWth.

The plots in this chapter show the efficiency and heat loss of the two receiver types for two values of the solar emissivity of the active surfaces (0.95 and 0.85) with varying emissivities in the thermal wave length band and the passive surfaces. The emissivity step wavelength is varied between 2 and 5 µm to show its influence on the receiver performance. Both the cavity and the receiver model consider wind induced forced convection in the comparisons shown in the plots of this section. For the cavity the wind direction dependent model described in Section 4.3 is used. Figure 6.41 illustrates the dimensions of external and cavity receiver using this comparison. Although the absorber surface area of the external receiver is small than that of the cavity receiver, both provide the same design thermal output.

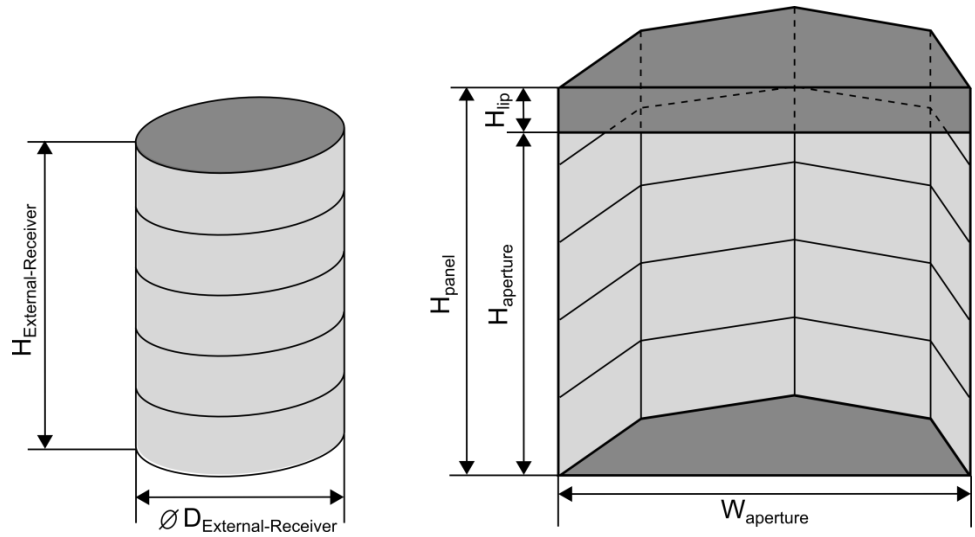

Figure 6.41 – Dimensions of External and Cavity Receiver in Comparison

Because of the passive surfaces, the total internal surface area is about twice as large as the surface area of the external receiver. Another parameter, shown in Table 6.b that is worth mentioning in a comparison of the two receiver types is the tower height. Due to the same thermal output the total size of the heliostat field is about the same for each receiver type. Because the external receiver is located in the center of the field, the maximum distance between tower and heliostats is less than it is for a cavity type receiver, where the tower is located on the south side of the field. With the distance of the tower to the heliostats the focal point of the field needs to be higher above ground, resulting in a significantly greater tower height using cavity receivers.

	External Receiver	Cavity Receiver
Height	18.8 m	23.95 m
Diameter/Width	12.44 m	25.78 m
Active surface area	734.73 m^2	945 m^2
Passive surface area	0 m^2	540.85 m^2
Tower Height	183.33 m	312.34 m

Table 6.b - Selected dimension of External and Cavity Receiver in Comparison

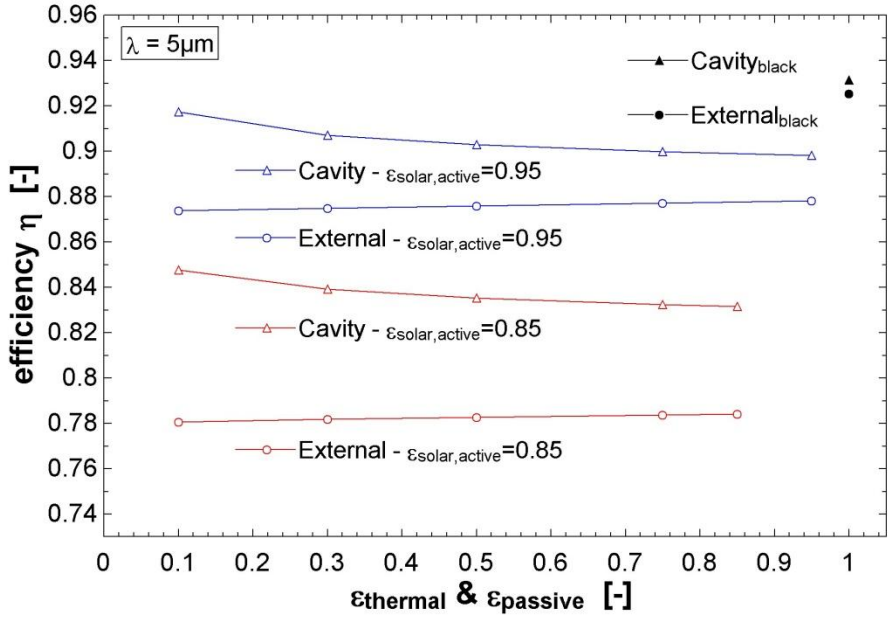

Figure 6.42 - Thermal efficiencies of cavity and external receiver for different emissivities; Emissivity step wavelength is at 5μm

As shown in Figure 6.42, the receiver efficiency of the cavity receiver is larger than for the cylindrical external receiver. For high solar absorbance ($\varepsilon_{solar\text{-}active}$=0.95) of the active surfaces, the difference is about 1-4% in total efficiency. For lower solar absorbance of the active surfaces ($\varepsilon_{solar\text{-}active}$=0.85), the efficiency of the cavity is about 4-6% larger than the efficiency of the external receiver. The efficiency of both receiver types assuming black surfaces is also given. Due to the higher solar absorbance, the efficiency is higher than for semi-gray surfaces. It is notable that the external receiver has a higher efficiency for black surfaces than the cavity receiver. The efficiency advantage of the cavity only comes into play for reflective surfaces. The heat losses for both receiver types are shown in Figure 6.43 and Figure 6.44 for different solar emissivities of the active surfaces. It can be seen that the radiation loss of the cavity is about half of that of the external receiver. The assumed higher convective losses for the cavity reduce the efficiency noticeably but still result in an efficiency advantage for the cavity receiver. The magnitude and characteristic of the convective losses are governed by the applied convection model and described in Section 6.3.1.

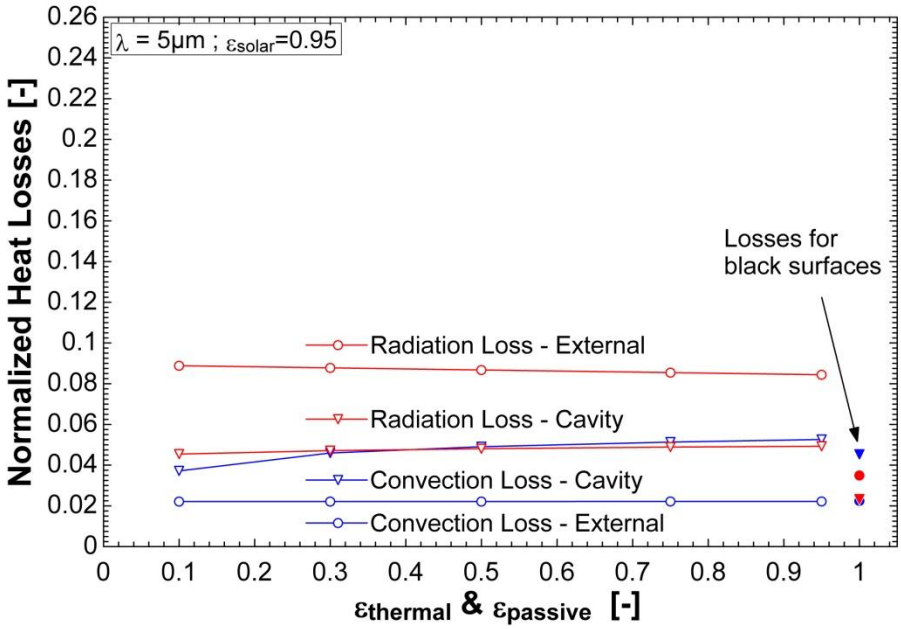

Figure 6.43 – Normalized radiation- and convection loss of cavity and external receiver for different emissivities – $\varepsilon_{solar\text{-}active}$=0.95

In comparison to Figure 6.43, the solar emissivity of the active surfaces in Figure 6.44 is lower. This results in higher solar reflective losses, for both the external and the cavity receiver. Because the cavity geometry is able to capture part of this reflected radiation, the radiation losses are about half of that of the external receiver. For decreasing solar emissivity the radiation losses account larger fractions of the total heat loss. Consequently, the difference in efficiency of the cavity and the external receiver increase.

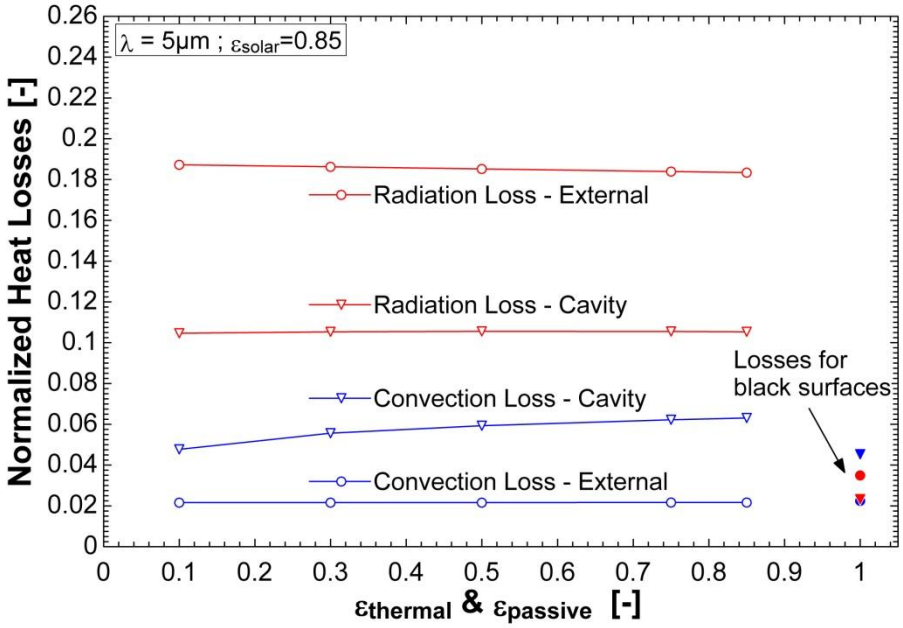

Figure 6.44 - Normalized radiation- and convection loss of cavity and external receiver for different emissivities – $\varepsilon_{solar\text{-}active}$=0.85

The plots show that the radiation loss of the external cylindrical receiver is significantly larger than for the cavity. The cause for these higher losses can be seen in Figure 6.45. All incident radiation on the external receiver that is not absorbed by the surfaces is reflected to the surroundings and lost for the purpose of heating the HTF. The cavity however is able to capture some of the reflected and emitted radiation that would otherwise be lost to the surroundings for the external receiver. Because of this radiation capturing effect, the reflective losses of the cavity receiver are about half of the reflective losses of the external receiver.

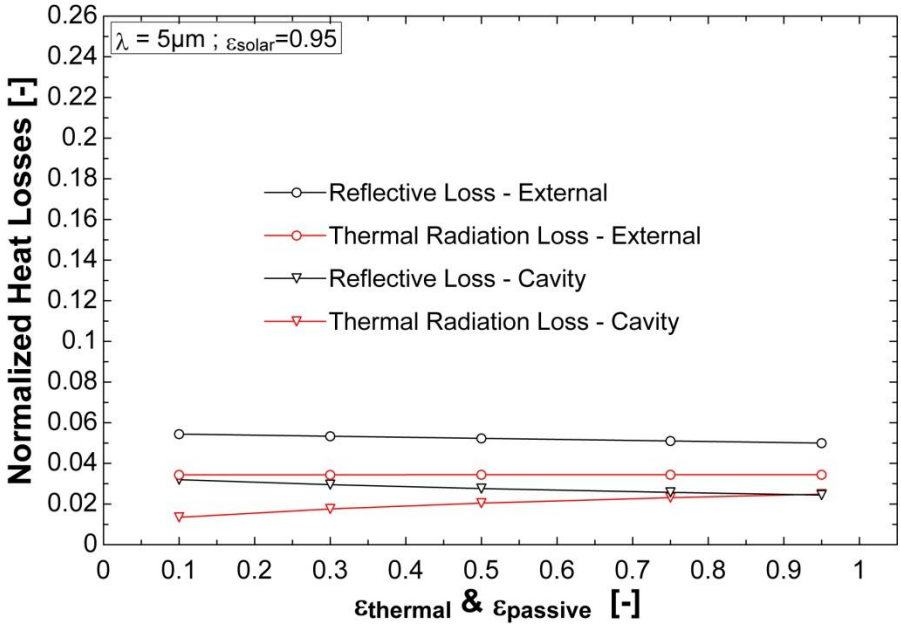

Figure 6.45 - Normalized reflective- and thermal radiation loss of cavity and external receiver for different emissivities – $\varepsilon_{solar\text{-}active}$=0.95

It is interesting that the radiation losses vary by less than 1% of the incoming solar radiation over the range the full thermal emissivity range. A more detailed description of the radiation heat transfer effects inside the cavity is given in Section 6.1. The general behavior of cavity and external receiver in Figure 6.45 however is very similar. With decreasing thermal emissivity the solar losses increase because of the overlap of solar radiation in the thermal emissivity band. The increasing reflectivity of the passive surfaces of the cavity increases the solar losses as well. The thermal radiation losses of both receive types decreases with decreasing thermal emissivity. These effects counter act, resulting in only slight variation in total radiation losses. The increase in efficiency of the cavity with decreasing thermal emissivity is almost entirely caused by the lower convection losses due to lower surface temperatures. Using the upper bound of natural convection coupled with the forced convection approximation our model predicts significantly higher convective losses for the cavity than for the external receiver. This result contradicts the underlying assumption of the cavity receiver design that a cavity should lead to lower convective losses than an exposed external receiver. This result is non-intuitive and illustrates the uncertainty with that convective losses of the cavity are modeled in this simulation. Obviously there is a need

for further research to be able to model convective losses of a large concentrated solar power cavity receiver reliably.

The previous results are given for an emissivity step wavelength of 5μm. Considering the same situation for an emissivity step at λ=2μm the characteristic of the receivers change in that the distribution of the different radiation types in the two emissivity bands changes.

As shown in Table 3.a, for λ=5μm, almost all solar radiation occurs in the solar emissivity band, as well as 48-80% of the temperature driven radiation. For λ=2μm the temperature driven radiation almost entirely occurs in the thermal emissivity band, as well as a non-negligible (6%) fraction of the solar radiation. This distribution changes the characteristic of the radiation loss progression with decreasing emissivity. While in the previous case lower emissivities resulted in only slight change of the radiation losses the losses increase significantly for λ=2μm. Because about 6% of the incident solar radiation now occurs in the thermal emissivity band, this fraction contributes more to the reflection losses with decreasing the thermal emissivity. As shown in Figure 6.46 the efficiency of external and cavity receiver now decrease with decreasing emissivity, the efficiency of the cavity is still 2-7% higher than for the external receiver. As mentioned before, this effect is caused by the dominating influence of radiation loss on the receiver efficiency. Because the cavity is able to capture some of the emitted and reflected radiation from the receiver to the surroundings, the radiation loss is generally lower for the cavity. This loss characteristic can be observed in Figure 6.47 and Figure 6.48.

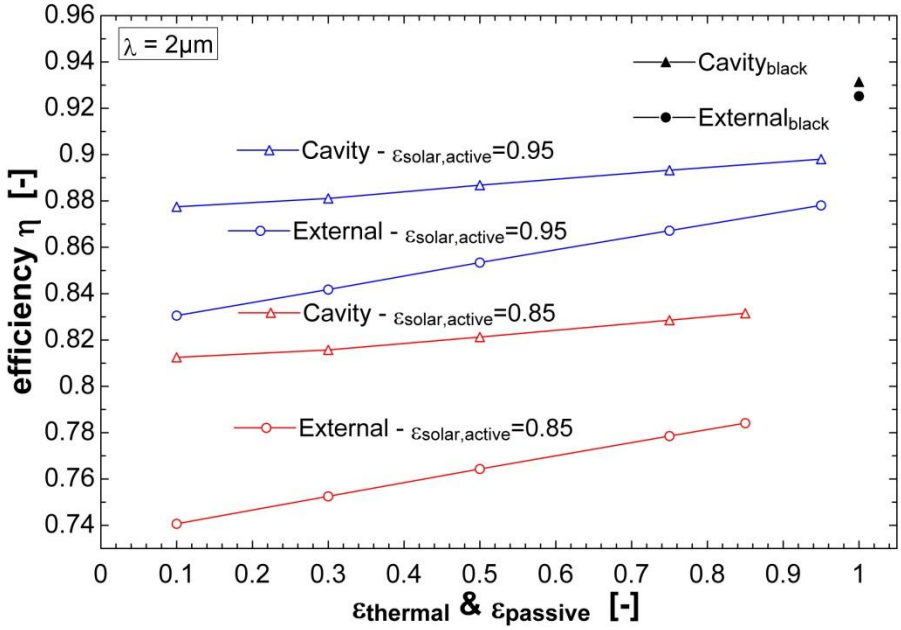

Figure 6.46 - Thermal efficiencies of cavity and external receiver for different emissivities; Emissivity step wavelength is at 2μm

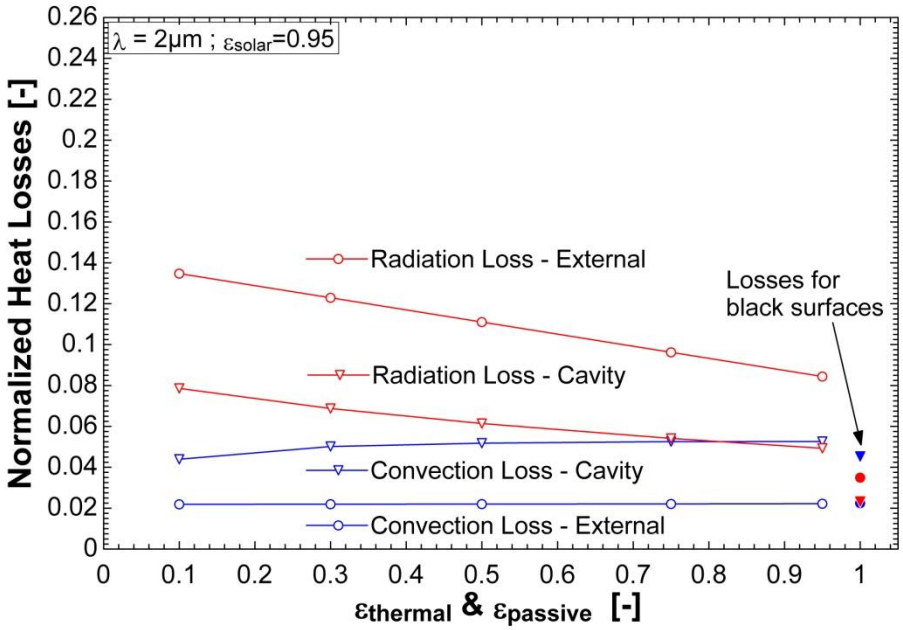

Figure 6.47 - Normalized radiation- and convection loss of cavity and external receiver for different emissivities – $\varepsilon_{solar\text{-}active}$=0.95

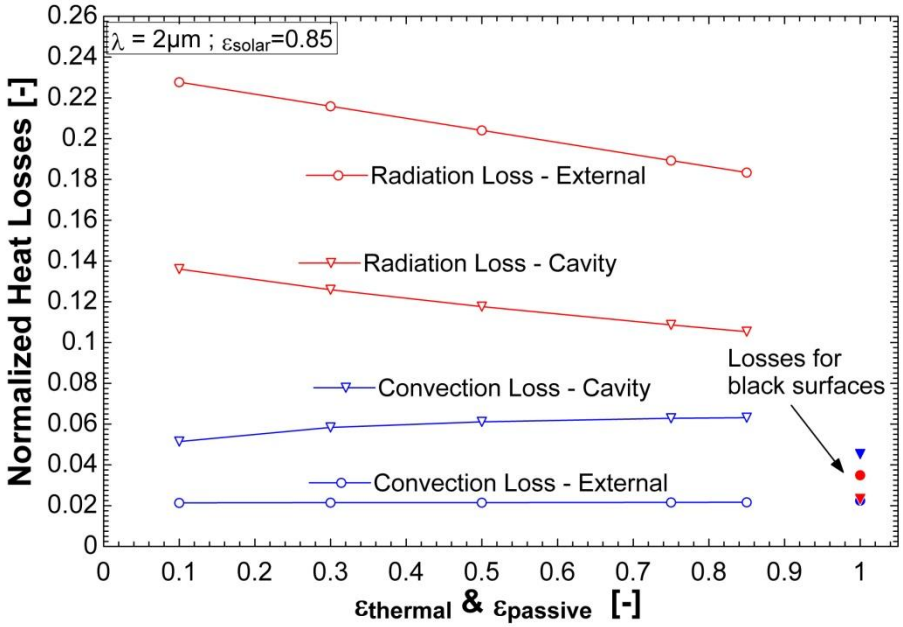

Figure 6.48 - Normalized radiation- and convection loss of cavity and external receiver for different emissivities – $\varepsilon_{solar\text{-}active}$=0.85

As described above you can see in Figure 6.49 that because of the higher fraction of solar radiation in the thermal emissivity band, the reflective losses of the receivers increase with decreasing thermal emissivity. The thermal losses still decrease but are overpowered by the increasing reflective loss.

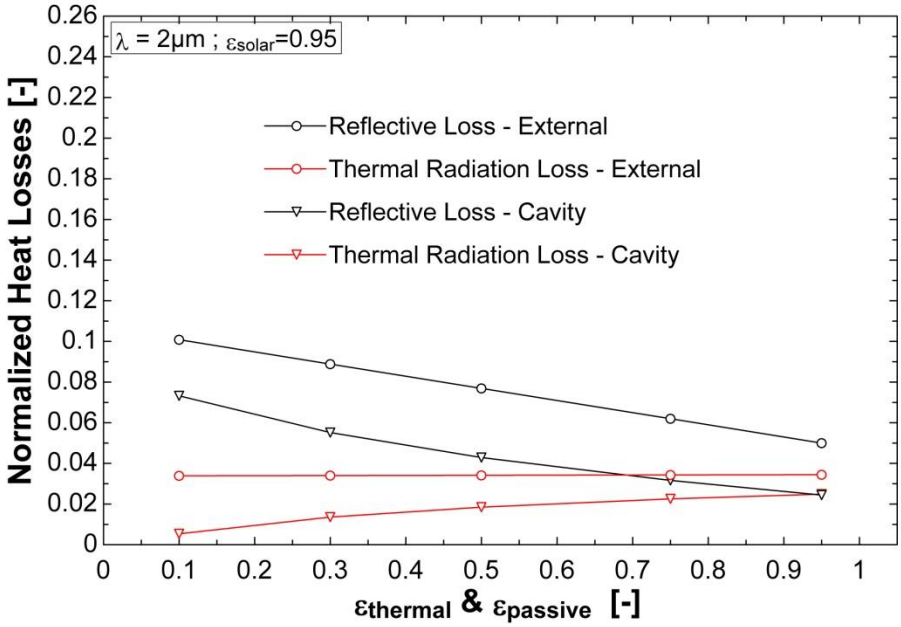

Figure 6.49 - Normalized reflective- and thermal radiation loss of cavity and external receiver for different emissivities – $\varepsilon_{solar\text{-}active}$=0.95

7 Conclusion

An analytical method was developed to model semi-gray radiation heat transfer inside a concentrated solar power cavity receiver. It considers all radiative interaction inside the cavity due to reflectance and emittance for diffuse surfaces. The application of a two band model is presented in this work, the model is however also applicable to more emissivity bands; the necessary equations are derived in this work and a sensitivity study was done to show the influence of the number of bands on the results of the model.

The method was implemented in the existing cavity receiver model in the System Advisor Model (SAM) developed by the National Renewable Energy Laboratory (NREL). SAM allows users to examine and to compare solar, other renewable technologies on economic, technological and operational bases. Annual simulations are done using typical mean year (TMY) weather data.

The modeling of convective heat losses of the cavity receiver model in SAM was also improved as part of this work. The convective losses in the original model were only included in a global energy balance; convective losses were accounted for in the determination of the useful energy gain and the efficiency of the receiver, but had no influence in the calculation of the receiver surface temperatures. The new model allows the user to accept the assumptions made in the model to determine the convection loss distribution inside the cavity to include convective losses in the local energy balances. In this way convective losses are directly included in the calculation of the cavity surface temperatures.

Due to the lack of valid correlations to determine convective losses of the cavity receiver a model was developed that is expected to provide the upper bound of natural convection loss. This model represents the cavity receiver as a combination of flat plates. To account for the buoyancy induced flow regime inside the cavity receiver, correlations for forced convection at flat plates are used to represent the natural convection loss of the cavity. The characteristic natural convection velocity is used as a flow velocity at all surfaces.

To include forced convection in the cavity receiver model the only available correlation, developed by (Siebers, D. and Kraabel, J., 1984) is used. To approximate the influence of wind direction on the convection loss of the cavity a scaling factor is introduced. The scale factor as it is implemented now utilizes a trigonometric function to model the decreasing influence of forced convection for direction from the backside of the receiver. In the current implementation,

maximum forced convection losses are assumed for wind perpendicular to the cavity aperture, minimum forced convection losses for wind from the back. This distribution however is strongly dependent on the tower geometry; there are also numerical studies that suggest that side wind leads to highest forced convection losses. Due to this lack of certainty in determining convective losses the possibilities to measure convective losses of a cavity receiver were analyzed. Small scale and large scale experiments were considered, leading to the conclusion that to obtain reliable, representative data a large scale experiment is necessary. It is questionable if the convection losses can be measured within a range of uncertainty that provides useful information.

With these improvements of the cavity model, the performance of the cavity receiver in dependence on surface emissivities was analyzed. It was found that while selective surfaces with higher solar emissivity and low thermal emissivity at the irradiated absorber surfaces improve the receiver efficiency this not the case for the adiabatic passive surfaces. To reduce the temperature and losses from these surfaces high reflectance in all wavelength bands is beneficial.

The semi-gray radiation model was also implemented in the external receiver model included in SAM. The performance of external and cavity receiver were compared as a function of surface emissivities. For optimum surface emissivity configuration, the cavity receiver always provided higher thermal efficiencies (depending on the solar emissivity 2-7%).

8 Future Work

For future work, the implementation of presented multi-band model with more than two emissivity bands is an interesting project to improve the radiation model. The application of this method using a real surface emissivity characteristic would be a good way to benchmark the presented model.

The existing model assumes diffuse radiation and reflection, meaning radiative characteristics that are independent of the incident angle of the incoming radiation. Whether this assumption is sufficient to accurately model real surfaces in concentrated solar application has to be shown.

Apart from the radiation model major uncertainties are present in the modeling of convective losses. Because none of the established convection loss correlations for cavity receivers are valid in the range of operational condition observed for our cavity receiver model the magnitude of convective losses is uncertain. The developed upper bound of natural convection is expected to overestimate the natural convective losses significantly. For a detailed model of a cavity receiver the local convection loss distribution has to be known. The distribution in this study is taken from an existing correlation, extrapolated and scaled to obtain a local convection loss for each computational surface segment that corresponds to more recent convection correlations. The obtained convection loss distribution lacks any physical basis and needs to be verified.

The same can be said for forced convection. The model used in this work to approximate forced convection is rough and has no physical verification. Improvements in the field of modeling convective losses of cavity receivers are absolutely necessary to be able to simulate these systems more accurately.

9 Bibliography

Al-Ansary,H. et al. 2011. Experimental Study of a Sand-Air Heat Exchanger for use with a High Temperature Solar Gas Turbine System. *Proceedings SolarPACES 2011 - Granda, Spain* . 2011.

Bailey, B.H., McDonald, S.L. 1997. *Wind Resource Assessment Handbook.* s.l. : AWS Scientific, Inc. , 1997. NREL Subcontract No. TAT-5-15283-01 .

Beckman, W.A. 1968. Temperature Uncertainties in Systems with Combined Radiaiton and Conuction Heat Transfer. 1968.

Clausing, A.M. 1981. An analysis of convective losses from cavity solar central. *Journal of Solar Energy.* 1981, Vol. 27, 4, pp. 295-300.

—. 1983. Convective Losses from Solar Central Receivers – Comparisons. *Journal of Solar Energy Engineering.* 1983, Vol. 105, pp. 29-33.

—. 1987. Natural Convection from Isothermal Cubical Cavities with a Variety of Side-Facing Apertures. *Journal of Heat Transfer.* 1987, Vol. 109, pp. 407-412.

Division, United Nations Statistics. 2008. UNdata. [Online] United Nations, 2008. [Cited: 10 12, 2011.] http://data.un.org/Data.aspx?d=EDATA&f=cmID%3aEL.

Duffie, J. A., Beckman, W.A. 2006. *Solar Engineering of Thermal Processes 3rd ed.* hoboken, Nwe Jersey : John Wiley & Sons INC, 2006.

Falcone, P., K. et al. 1981. Convective Losses from Solar Central Receivers. *Proceedings of a DOE/SERI/SNLL Workshop.* 1981.

Fang, J.B. et al. 2011. Thermal performance simulation of a solar cavity receiver under wnidy conditions. *Solar Energy.* 2011, Vol. 85, pp. 126-138.

Feierabend, L. 2009. *Thermal Model Development and Simulation of Cavity-Type Solar Central Receiver Systems.* Madison, Wisconsin : University of Wisconsin-Madison – Solar Energy Laboratory, 2009.

Gebhart, B. 1957. Unified Treatment for Thermal Radiation Transfer Processes. 1957.

Hewitt, G.F. 2008. *Heat Exchanger Design Handbook - Part 2 - Fluid Mechancs and Heat Transfer.* New York, Connecticut, Wallingfordm U.K. : begell house, inc. publishers, 2008. ISBN 978-1-56700-255-3.

Ho, C.K. et al. 2010. Methods for Probabilistic Modeling of Concentrating Solar Power Plants. *Solar Energy.* 2010.

Howell, J. R. 2010. *A Catalog of Radiaiton Heat Transfer Configuration Factors 3rd Editon.* [Online] Department of Mechanical Engineering - University of Austin Texas, 2010. [Cited: 10 23, 2011.] http://www.engr.uky.edu/rtl/Catalog/.

Hunt, A. 1979. A New Solar Thermal Receiver Utilizing Small Particles. *Proceedings of the International Solar Energy Society Conference, Altanta, GA.* 1979.

Kays, W.M. and Crawford, M.E. 1980. *Convective Heat and Mass Transfer 2nd ed.* s.l. : McGraw-Hill, 1980.

Klein, S.A. et al. 2007. *TRNSYS 16.* [Online] Thermal Energy System Specialists, LLC, 2007. [Cited: 12 6, 2011.] http://sel.me.wisc.edu/trnsys/.

Klein, S.A. 2011. F-chart Software. *Engineering Equation Solver (EES).* [Online] 2011. [Cited: 11 24, 2011.] http://www.fchart.com/.

Leibfried, U. and Orthjohan, J. 1995. Convective Heat Loss from Upward and Downward-Facing Cavity Solar Receivers: Measurements and Caclulations. *Journal of Solar Energy Engineering.* 1995, Vol. 117, 2, pp. 75-85.

LeQuere, et al. 1981. Experimental Study of Heat Loss Through Natural Convection From an Isothermal Cubic Open Cavity. *Proceedings DOE/SERI/SNLL Workshop in CEnvective Losses from Solar Receivers, SAndia Laboratories Report SAND81-8014, Livermore, CA.* 1981.

Loosen, A. et al. 2011. Development of a Solar Field and Receiver Simulation Tool for Central Receiver Technology. *SolarPACES2011, Granada, Spain.* 2011.

Ma, R.Y. 1993. *Wind Effeects on Convetive Heat Loss from a Cavity Receiver for a Parabolic Concentrating Solar Collector.* Albuquerque, NM : Sandia National Laboratories, 1993. SAND92-7293.

Nellis, G. and Klein, S.A. 2009. *Heat Transfer.* New York : Cambridge University Press, 2009. ISBN 978-0-521-88107-4.

NREL. 1990. Solar Radiation Data Manual for Flat-Plate and Concentrating Collectors. [Online] 1990. [Cited: 12 3, 2011.] http://rredc.nrel.gov/solar/pubs/redbook/PDFs/CA.PDF.

—. 2011. System Advisor Model. [Online] National Renewable Energy Laboratory, 2011. [Cited: 11 10, 2011.] https://www.nrel.gov/analysis/sam/.

Omega. 2011. Ultrasonic Doppler Flowmeters. *Flow Reference Section.* [Online] Omega, 2011. [Cited: 6 24, 2011.] http://www.omega.com/toc_asp/frameset.html?book=Green&file=ULTRASONIC_FLOW_REF .

Paitoonsurikarn S. and Lovegroove K. 2003. On the study of Convection Loss from Open Cavity Receivers in Solar Paraboloidal Dish Applications. *Proccedings of 41st ANZES Conference.* 2003.

Paitoonsurikarn, S. and Lovegrove K. 2006. A New Correlation for Predicting the Free Convection Loss from Solar Dish Concentrating Receivers. 2006.

Petukhov, B. S. and Popov, V. N. 1963. Theoretical Calculation of Heat Exchanger and Frictional Resistance in Turbulent Flow in Tubes of an incompressible Fluid with Variable Physical Properties. *High Temp. Thermophys.* 1963, Vol. 1, pp. 69-83.

Pitz-Paal, R. et al. 1991. A new concept pf a selective solar receiver for high temperature applications. 1991, Vol. 24, pp. 293-306.

Prakash, M. et al. 2008. Investigations on heat losses from a solar cavity receiver. *Solar Energy.* 83, 2008, pp. 157-170.

Ritchie, J.A. 2010. Pressure Measurement Instrumentation in a High Temperature Molten Salt Test Loop. *MAster's Thesis, University of Tennessee.* http://trace.tennessee.edu/utk_gradthes/829 (6/24/2011), 2010.

Schlichting, H. 1958. *Grenzschicht-Theorie 3rd ed.* Karlsruhe, Germany : G. Braun, 1958.

Siebers, D. and Kraabel, J. 1984. *Estimating Convective Energy Losses from Solar Central Receivers.* s.l. : Sandia National Laboratories, 1984. SAND84-8717.

Siegel R.and Howell J.R. 2002. *Thermal Radiation Heat Transfer 3rd ed.* New York : Taylor & Francis, 2002.

Smith, D.C. and Chavez, J.M. . 1987. *A Final Report on Phase I Testing of a Molten-Salt Cavity Receiver.* Albuquerque, NM : Sandia National Laboratories, 1987. SAND87-2290.

Stine, W.B. and McDonald, C.G. 1989. Cavity Receiver Heat Loss Measurements. *Proceedings of ISES World Congress, Kobe, Japan.* 1989.

Taumoefolau, T. et al. 2004. Experimental Investigation of Natural Convection Heat Loss From a Model Solar Concentrator Cavity Receiver. *Journal of Solar Energy Engineering.* 2004, Vol. 126, pp. 801-807.

Taylor and Kuyatt. 1994. Guidelines for Evaluating and Expressing the Uncertainty of NIST Measurement Results. *NAtional Institute of Standards and Technology Technical Note 1297.* 1994.

Teichel, Soenke H. 2011. *Private photographs.* 2011.

Tempil, 2012. [Online] [Cited: 02 23, 2012.] http://www.tempil.com/products/pyromark/.

Torresol Energy. [Online] Torresol Energy Investments, S.A. [Cited: 10 31, 2011.] http://www.torresolenergy.com/TORRESOL/image-library/en?initdate=&enddate=&categoria=cw4cb8173de9630.

U.S. Census Bureau. 2010. State & County QuickFacts. *ane County, Wisconsin.* [Online] U.S. Census Bureau, 2010. [Cited: 12 3, 2011.] http://quickfacts.census.gov/qfd/states/55/55025.html.

Vatell. 2011. Thermo Gage Specification Sheet. [Online] Vatell Cooperation, 2011. [Cited: 6 27, 2011.] http://www.vatell.com/thermogage.htm .

Wagner, M. 2008. *Simulation and Predictive Performance Modeling of Utility-Scale Central Receiver System Power Plants.* Madison, Wisconsin : University of Wisconsin-Madison – Solar Energy Laboratory, 2008.

Weed. 2011. Thermocouple General Specification. [Online] Weed Instrument Company, 2011. [Cited: 6 24, 2011.] http://weedinstrument.com/product_groups/industrial/thermo_pdfs/TC-GEN%20SPECS.pdf .

Z'Graggen,A. and Steinfeld,A. 2009. Heat and Mass Transfer Analysis of a Suspension of Reacting Particles subjected to Concentrated Solar Radiation. *International Journal of Heat and Mass Transfer*. 2009, Vol. 52, pp. 385-395.

10 Appendices

A:

The net electricity production of the USA in 2008 was according to (Division, United Nations Statistics, 2008) $4{,}152{,}840 \cdot 10^6$ kWh. According to (NREL, 1990) the annual averaged incident solar radiation on a 2-Axis Tracking Flat-Plate Collector which is equivalent to a heliostat mirror in a solar collector field in Long beach, California is 7.3 kWh per m^2 and day. With 365 day per average year, 2664.5 kWh/m^2 of solar radiation are incident on a 1m^2 heliostat.

The net electricity production of the USA in 2008 is therefore equivalent to 1558km^2 or 601 square miles. To set this into relation, the area of Dane County in Wisconsin is according to (U.S. Census Bureau, 2010) about 1197 square miles.